



The
University
Of
Sheffield.

Fabrication of bio-mimetic multi-voided polystyrene particles acting as broad-band light scatterers

By:

Antonino Bianco

Submitted to The University of Sheffield in fulfilment of the requirements for the award of Doctor of Philosophy

The University of Sheffield Faculty of Science

Department of Chemistry

September 2017

DECLARATION

The work described in the present thesis was undertaken at the University of Sheffield between October 2013 and September 2017 under the supervision of Prof. Patrick Fairclough and Dr. Oleksandr Mykhaylyk. Unless otherwise stated, it is the work of the author and has not been submitted in whole or in any part for any other degree at this or any other institute. Some research reported in this manuscript has been published by the peer reviewed journal Langmuir (ACS Publications) with the title “Control of the porous structure of polystyrene particles obtained by non-solvent induced phase separation”.

Mr. Antonino Bianco

Department of Chemistry

The University of Sheffield

September 2017

PUBLICLY PRESENTED WORK.

UK Colloids 2014 Symposium, London. July 2014.

Fabrication of multi-voided polymeric particles. Poster session.

Macro Group UK Young Researchers Meeting, Durham University. July 2014.

Fabrication of multi-voided polymeric particles. Poster session.

Materials Cluster 2014, The University of Sheffield. July 2014.

Fabrication of multi-voided polymeric particles. Oral presentation.

Colloid and Soft Matter Symposium, The University of Sheffield. May 2015.

Fabrication of multi-voided polymeric particles and films capable of delivering white structural colour. Oral presentation joint with Stephanie Burg.

Postgraduate Research Poster Session, The University of Sheffield. October 2015.

Fabrication of multi-voided polystyrene particles for structural white. Poster session.

Summer School on Scattering Methods Applied to Soft Condensed Matter, Bombannes. June 2016.

Fabrication and characterisation of porous polystyrene micro-spheres. Oral presentation.

Materials Cluster 2016, The University of Sheffield. September 2016.

Fabrication and characterisation of porous polystyrene micro-spheres. Oral presentation.

Structural Colour Symposium, The University of Sheffield. July 2017.

Fabrication and characterisation of porous polystyrene micro-spheres. Oral presentation.

Co-author of the article: Spatially modulated structural colour in bird feathers. Andrew J. Parnell et al. *Scientific Reports*, vol 5, p18317, (2015).

Author of the article: Control of porous structure of polystyrene particles obtained by non-solvent induced phase separation. Antonino Bianco et al. *Langmuir*, 33 (46), p13303-13314, (2017).

ABSTRACT.

Titanium dioxide is the main white pigment used in the paint industry. It is the most efficient broad-band light scattering material due to the high refractive index and its ability to scatter light across the entire visible range of the electromagnetic spectrum. However, the high production costs and the high carbon footprint associated with this compound constitute a motivation for investigating alternative materials. Polymeric particles have the potential to become a competitive alternative considering both their physical properties and the comparatively low production costs. The objective of this work was the identification of a simple and cost effective system for the production of bio-mimetic multi-voided polymeric particles, to be introduced in paint formulation as a partial replacement for the industrial white material titanium dioxide.

Nature does not rely on titanium dioxide to produce striking examples of white and is particularly ingenious in designing structures that are capable of maximising the amount of scattering in very little material, producing a remarkable white in very thin tissues. Some of the most relevant structures displaying exceptional white are the scales of the *Cyphochilus* and *Lepidiota stigma* beetles, consisting of isotropic networks of rod-like filaments of chitin and air-filled voids, and the foam-like structures found in the feathers of the *Garrulus glandarius* (Eurasian jay) bird, consisting in spherical air-filled voids within a keratin matrix. Those were identified as the target structures for the synthetic work. An effective way of producing porous structures in polymer materials is based on the possibility of inducing phase separation in an initially homogeneous polymer solution. The phase separation process can be initiated by the introduction of a non-solvent (NIPS) into the system and can proceed by a mechanism of nucleation and growth, producing closed pores within a polymer matrix resembling the foam-like structures of the *Garrulus glandarius*, or by spinodal decomposition, producing interconnected polymer-pore domains, similar to the networks found in the *Cyphochilus* and *Lepidiota stigma* beetles' scales.

Polystyrene was the polymer selected for the synthetic work, due to a good compromise between costs, refractive index and a large selection of good solvents. The first attempt at fabricating polystyrene multi-voided particles by NIPS involved a simple ternary system with tetrahydrofuran as the solvent and deionised water as the non-solvent. The process was successful in achieving porosity, but particles size and shape were difficult to control. The

fabrication process was upgraded by employing an Ink-Jet apparatus, capable of reducing and standardising the size of the polystyrene solution droplets. The Ink-Jet provided a way to control particles' shape and size, but presented a fatal flaw in the fact that the production was limited to a very small amount of material and the process was not industrially scalable. In order to overcome these limitations, a modification of the fabrication process was necessary, whereby the ability to control shape and size of the polymer solution droplets would not rely on the mechanical capabilities of the equipment employed, but rather on the intrinsic properties of the chemical system. An emulsion system was considered, where the polystyrene in toluene solution was finely dispersed into a continuous phase of deionised water. The spherical shape of the droplets was achieved by the action of the surface tension and the droplets' size could be controlled by the level of shear applied to the emulsion mixing. The emulsion method allowed the production of particles with the desired specifications and was a scalable process. The scale up was performed in the AkzoNobel® laboratories. The polystyrene multi-voided particles, along with titanium dioxide and the extender Ropaque, were implemented in paint formulations. The paints were spread on substrates to produce paint films of a desired thickness. The reflectance of the paint films was measured using a spectrophotometer and their density calculated. The reflectance and density data allowed the calculation of the scattering coefficient of the paints. A factorial design analysis of the scattering results was performed in order to compare the scattering power of the polystyrene multi-voided particles with those of titanium dioxide and Ropaque, and to highlight any synergistic effects between these materials. The analysis concluded that polystyrene multi-voided particles have a scattering power of 57-60% that of the Ropaque extender and of 6-8% that of titanium dioxide.

ACKNOWLEDGMENTS.

I would like to sincerely thank my supervisors Patrick Fairclough and Oleksandr Mykhaylyk for their patience and guidance in this academic journey. Without their continuous support and their precious inputs this work could have not been accomplished.

I would also like to thank the structural colour group at the University of Sheffield, formed by Andrew Parnell, Stephanie Burg, Christine Fernyhough, Adam Washington and David Whittaker, for their help and for the productive discussions. I am very grateful to Christopher Hill and Alan Dunbar for their support with SEM analysis, to Patrick Smith and Jonathan Stringer for their assistance with the Ink-Jet equipment, to Lian Hutchings' group at Durham University and Steve Armes' group at the University of Sheffield for their help with GPC analysis. A special thank you goes to the European Synchrotron Radiation Facility (ESRF) in Grenoble for providing SAXS beam time, and to Sylvain Prevost and the personnel of the ID02 beamline for the assistance with SAXS experiments. I would like to thank all the colleagues at the graduate office in Garden Street who got me through the daily routine. A special thank you goes to the AkzoNobel® group for their advice and expertise, and in particular to Bogdan Ibanescu and David Elliott for their precious help with the challenging experimental tasks carried out in Slough. I would also like to mention Andrew Parker from the Natural History Museum in London who provided great inputs for targeting the best biological structures, and Innovate UK for the financial support of the project.

On a personal level, I would like to thank my family, my mother Nunzia, my father Renato and my brother Roberto for their help and encouragement at all times.

A special thank you goes to Irene, Michelangelo and Francesco F. who played a major role in helping me maintain mental well-being during those stressful four years. You were my safe sanctuary in London whenever I needed to escape. A thank you to Margherita from the far away Montreal, who never stopped believing in my potential. I would like to thank Silvia, Giulia, Dario and Francesco A. from the University of Sheffield Italian Society to help me settle in when I first moved to Sheffield and for sharing a part of this academic journey together.

Special thanks go to Claudia, Mateo, Federica, Eirini, Xeni, Gioia, Caterina, Stathis, Francesca, Andrea and the little Irene for brightening my days in Sheffield.

Table of Contents

OBJECTIVE.....	9
CHAPTER 1: OPTICS.....	10
THIN-FILM INTERFERENCE.....	13
MULTI-LAYER INTERFERENCE.....	14
DIFFUSE OR INCOHERENT REFLECTION.....	16
DIFFRACTION.....	18
PHOTONIC CRYSTALS.....	20
LIGHT SCATTERING.....	21
CHAPTER 2: STRUCTURAL COLOUR IN NATURE.....	26
BUTTERFLIES.....	27
BEETLES.....	33
BIRDS.....	37
CHAPTER 3: REPRODUCTION OF BIOLOGICAL STRUCTURES BY A PROCESS OF NON-SOLVENT INDUCED PHASE SEPARATION OF A HOMOGENEOUS POLYMER SOLUTION.....	44
THERMODYNAMICS OF PHASE SEPARATION OF A POLYMER SOLUTION.....	44
CHAPTER 4: MATERIALS AND CHARACTERISATION TECHNIQUES.....	51
MATERIALS.....	51
CHARACTERISATION TECHNIQUES.....	55
GEL PERMEATION CHROMATOGRAPHY (GPC).....	55
VISCOSITY OF THE POLYMER SOLUTIONS AND C^*	57
CLOUD POINT DETERMINATION.....	63
DYNAMIC LIGHT SCATTERING (DLS).....	65
SCANNING ELECTRON MICROSCOPY (SEM) AND IMAGE-J ANALYSIS OF SEM.....	67
SMALL ANGLE X-RAY SCATTERING (SAXS).....	70
CHAPTER 5: MULTI-VOIDED POLYSTYRENE PARTICLES BY A PROCESS OF NON-SOLVENT INDUCED PHASE SEPARATION OF A POLYSTYRENE SOLUTION.....	76
NIPS BY SOLUTION - FABRICATION PROCESS.....	76
CHARACTERISATION OF MULTI-VOIDED POLYSTYRENE PARTICLES BY SEM.....	78
FABRICATION PROCESS BY INK-JET.....	82
CHAPTER 6: MULTI-VOIDED POLYSTYRENE PARTICLES BY A PROCESS OF NON-SOLVENT INDUCED PHASE SEPARATION OF A POLYSTYRENE EMULSION.....	89
NIPS BY EMULSION - FABRICATION PROCESS.....	89
CHARACTERISATION OF POLYSTYRENE BY GPC.....	92
PHASE SEPARATION OF POLYSTYRENE – TOLUENE – ETHANOL SYSTEMS.....	95

CHARACTERISATION OF POLYSTYRENE SOLUTIONS: CRITICAL CHAIN OVERLAP CONCENTRATION.	97
CHARACTERISATION OF POLYSTYRENE SOLUTIONS: VISCOSITY.....	99
CHARACTERISATION OF EMULSION DROPLETS SIZE.....	103
CHARACTERISATION OF MULTI-VOIDED POLYSTYRENE PARTICLES BY SAXS.	104
CHARACTERISATION OF MULTI-VOIDED POLYSTYRENE PARTICLES BY SEM.	107
CORRELATIONS BETWEEN POLYMER CONCENTRATION OF POLYSTYRENE–TOLUENE SOLUTIONS AND STRUCTURAL MORPHOLOGY OF THE PARTICLES.	112
CHAPTER 7: NIPS BY EMULSION SCALE UP.	118
PERFORMANCE OF MULTI-VOIDED PARTICLES IN PAINT FORMULATIONS.....	128
CHAPTER 8: CONCLUSIONS AND FUTURE WORK.	149
REFERENCES.....	154

OBJECTIVE.

The objective of this project is the creation of a simple and cost effective system for the fabrication of bio-mimetic multi-voided polymeric particles for light scattering. The inspiration for the internal structure of the particles is derived from natural structures capable of exploiting purely physical mechanisms of light – matter interactions¹ in order to produce long lasting structural colour.² A particular focus is given to broad-band reflectors and scatterers,³ able to achieve white due to the efficient scattering of light across the entire visible spectrum. Several species of beetles⁴ and birds⁵ have evolved the ability to produce structures able to maximise light scattering in thin and light organic tissues.⁶ This work is an attempt to mimic such structures in polystyrene particles that would act as small broad-band scatterers, producing white.

The ultimate goal of the project was the implementation of the multi-voided particles in paint formulations provided by the industrial partner AkzoNobel®. The particles act as light scattering centres within the paint, contributing to opacity and white in paint films.⁷

The function of white materials and opacifiers in industrial paints is currently performed by titanium dioxide,⁸ which is a very efficient scatterer with a high refractive index.¹ Titanium dioxide is assisted in the role of opacifier by other agents known as extenders,⁷ generally consisting of inorganic materials such as calcium carbonate, aluminium silicate, magnesium carbonate, which are not as effective as TiO₂ due to a lower refractive index.⁷ Organic extenders, consisting of core-shell (or voided) polymer latex particles, are also employed.⁹ In general, the core-shell polymer particles exploit the difference in refractive index between the polymer shell and the air contained in the single cavity (core) to scatter light in the visible range of the electromagnetic spectrum. Extenders are used in paints in order to reduce the amounts of titanium dioxide, which is an expensive material with a high carbon footprint.¹⁰ The introduction of cheap bio-mimetic polymeric broad-band scatterers in paint films, acting as organic extenders characterised by multiple air-filled voids, may contribute to a further reduction of TiO₂ levels and lead to more eco-friendly paints. It is obvious that the high refractive index of TiO₂ ($n = 2.61$ at the wavelength of light $\lambda = 589$ nm) and its ability to scatter light across the entire visible range of the electromagnetic spectrum make this compound the most preferable broad-band light scattering material. However, other scattering agents, in particular polymeric particles, could be a competitive alternative considering both their physical properties and production costs. In this respect, it would be useful to obtain quantitative information about to what extent these materials can be used as opacifiers in a comparison with TiO₂. So far there was no systematic study providing insights into potential applications of multi-voided polymeric opacifiers.

CHAPTER 1: OPTICS.

Light can be defined as a transverse electromagnetic wave, where the direction of the energy propagation is perpendicular to the motion.¹¹ The **refractive index n** is a key parameter in the description of the light phenomena that occur when the electromagnetic (EM) radiation interacts with matter. The refractive index is defined as:¹²

$$n = \frac{c}{v} \quad \text{Equation 1}$$

where c and v are the velocity of the electromagnetic radiation in vacuum and in a medium respectively. The refractive index determines the extent at which the EM radiation is refracted at the interface of two different media.¹² It has to be noted that the refractive index depends on the wavelength of the EM radiation.

The electromagnetic radiation spectrum is broad, encompassing gamma-rays to one end with waves of high frequencies ν (in the order of exa-Hertz) and short wavelengths λ (pico-meters) to radio-waves with low frequencies (Hertz) and long wavelengths (km) to the other end.¹³ The range of EM radiation that can be directly perceived by the human eye is referred to as visible light and it is delimited by the violet light with frequency of 750 tera-Hz and wavelength of 400 nm and by the red light with frequency of 430 tera-Hz and wavelength of 700 nm.¹³

Colour is a human perception derived from the stimulation of the cone cells in the eye, triggered by EM radiation. Three different types of cone cells respond to different bands of light wavelengths: 564-580 nm (red), 534-545 nm (green), 420-440 nm (blue).¹⁴ The combination of stimuli due to the three types of cone cells, defined as trichromacy, covers the entire visible range in humans.¹⁴ Other animal species have cone cells sensitive to other bands (eg. ultraviolet) or a different number of cone cells (eg. five in the *Papilio butterfly*, pentachromacy) providing a different vision experience.¹⁵ Sight is one of the most effective ways in which living organisms gain information on the external environment. Colour plays a key role in the evolution where organisms developed coloured tissues for different purposes, from species recognition to sexual selection and camouflage.^{16 17}

Colour can be produced by reflected or transmitted light as the result of wavelength selective absorption. This is generally defined as a chemically produced colour and it occurs in materials such as pigments and dyes.⁵ The energy carried by the photons induces the promotion of electrons to higher molecular energy levels in conjugated systems of double bonds present in the chromophore

molecules. Part of the visible light is thus absorbed by the pigment while only certain wavelengths are transmitted or reflected giving rise to the observed colour.⁵

However, colour can also be the result of purely physical mechanisms occurring when the light interacts with certain types of structures in a material. Thin-film interference, multi-layer interference, diffraction and scattering are such mechanisms.¹⁸ The colour generated by those is defined as structural colour and it is the focus of this work. One of the main advantages of structural colour over pigmentation is that, while pigments undergo chemical degradation and gradually lose the ability to perform wavelength selective absorption, the organic design responsible for structural colour remains virtually unchanged over time.⁵

When describing optical phenomena, light is usually represented in the form of a ray, which can be defined as an imaginary line that symbolises the direction in which the radiant energy flows. A group of parallel light rays is usually defined as a light beam.¹⁹ These concepts are systematically used in this work to illustrate the behaviour of light interacting with objects.

When light travels from a medium with refractive index n_1 to a second medium with refractive index n_2 , reflection and refraction of the incident wave takes place. This scenario is effectively described by the **Fresnel's Law**.⁵

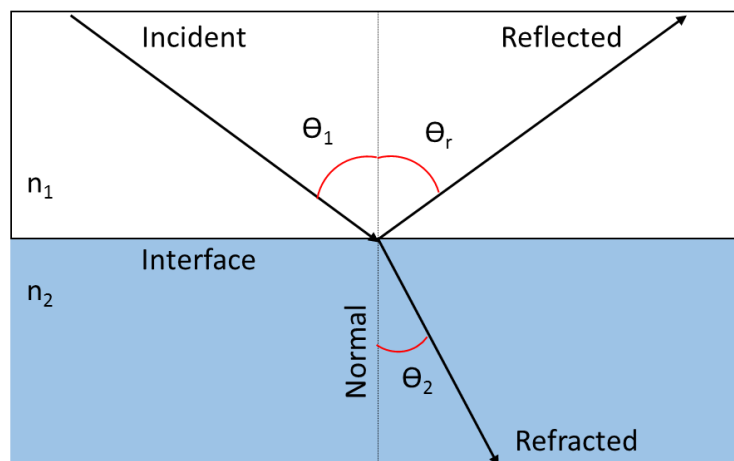


Figure 1: Light behaviour at the interface between two isotropic media with refractive indices n_1 and n_2 . The incident light beam is reflected with an angle $\theta_r = \theta_1$ and refracted with an angle θ_2 at the interface between the two media.

A plane wave incident with an angle θ_1 on an interface between two isotropic media with refractive index of n_1 and n_2 respectively, is reflected θ_r and refracted θ_2 at the interface: the directions of the incident, reflected and refracted waves lie on the plane.⁵ The reflectance r and transmittance t at the

interface are dependent on the polarization of light. Considering the two extremes, s-polarised light with the electric field direction perpendicular to the plane and p-polarised light when parallel to the plane, r and t are given by the equations:⁵

$$r_s = \frac{n_1 \cos \theta_1 - n_2 \cos \theta_2}{n_1 \cos \theta_1 + n_2 \cos \theta_2} \quad \text{Equation 2}$$

$$t_s = \frac{2 n_1 \cos \theta_1}{n_1 \cos \theta_1 + n_2 \cos \theta_2} \quad \text{Equation 3}$$

for s-polarised light and:

$$r_p = \frac{n_2 \cos \theta_1 - n_1 \cos \theta_2}{n_2 \cos \theta_1 + n_1 \cos \theta_2} \quad \text{Equation 4}$$

$$t_p = \frac{2 n_1 \cos \theta_1}{n_2 \cos \theta_1 + n_1 \cos \theta_2} \quad \text{Equation 5}$$

for p-polarised light.

From the Fresnel's Law, the **Law of Reflection** (Figure 1):²⁰

$$\theta_1 = \theta_r \quad \text{Equation 6}$$

and the **Snell's Law (Refraction)** (Figure 1) are derived:²⁰

$$\frac{\sin \theta_1}{\sin \theta_2} = \frac{v_1}{v_2} = \frac{\lambda_1}{\lambda_2} = \frac{n_2}{n_1} \quad \text{Equation 7}$$

where v is the velocity of light in the respective media and λ is the wavelength.²⁰

THIN-FILM INTERFERENCE.

One of the simple structures that give rise to structural colour when interacting with light is a thin, transparent film and this interaction is defined as **thin-film interference**.¹⁸

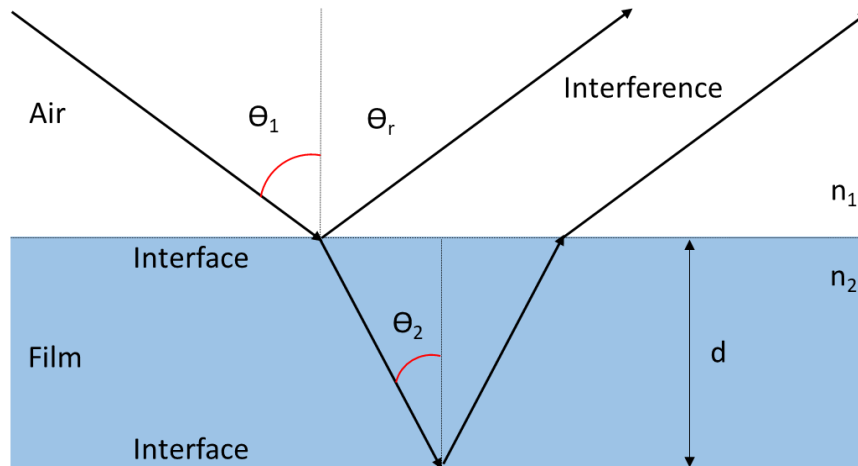


Figure 2: The phenomenon of thin-film interference. The incident light beam is reflected with an angle $\theta_r = \theta_1$ (eq. 6) and refracted with an angle θ_2 (eq. 7) at the first interface between the two isotropic media (air and a film of thickness d) with refractive indices n_1 and n_2 respectively. The refracted light is reflected again at the second interface and then refracted a second time. Constructive interference between the light initially reflected and the light travelling through the film occurs when the extra-path length travelled by the light across the film is a multiple minus half of the wavelength λ , eq. 8.

When a plane wave is incident with an angle θ_1 on a thin film of thickness d and refractive index n_2 it produces a reflected wave with an angle of reflection θ_r and a refracted wave with an angle of refraction θ_2 . At the second interface, the reflection takes place a second time, and the light reflected by the two interfaces interferes. Constructive interference for a certain wavelength is produced when (Figure 2):⁵

$$2 n_2 d \cos \theta_2 = \left(m - \frac{1}{2}\right) \lambda \quad \text{Equation 8}$$

where m is an integer number. Constructive interference therefore occurs when the extra-path length travelled by the beam across the film is a multiple minus half of the wavelength λ . Structural colour produced by thin-layer interference depends on the angle of incidence, the thickness of the film and the refractive index of the materials.⁵

MULTI-LAYER INTERFERENCE.

When thin layers of two different materials are assembled into a periodic structure, the optical phenomenon of **multi-layer interference** is observed.⁵ Considering a structure made of layers of thin-film 1 with refractive index n_1 and thickness d_1 and thin-film 2 with a refractive index n_2 and thickness d_2 periodically stacked on each other as in Figure 3, reflection and refraction of light take place at each interface.

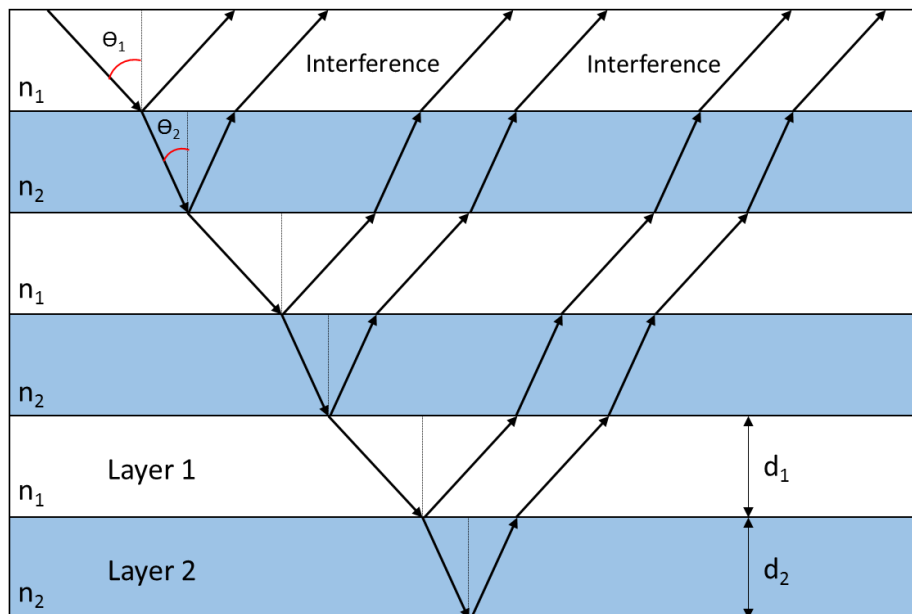


Figure 3: The phenomenon of multi-layer interference. Layers of thin-film 1 with refractive index n_1 and thickness d_1 and thin-film 2 with a refractive index n_2 and thickness d_2 are periodically stacked on each other. Light is reflected and refracted at every interface. Constructive interference is produced when the extra-path length travelled by the beam across the films is a multiple m of the wavelength λ , eq. 9.

Constructive interference is produced when:⁵

$$2 (n_1 d_1 \cos \theta_1 + n_2 d_2 \cos \theta_2) = m \lambda \quad \text{Equation 9}$$

where m is an integer number. Constructive interference therefore occurs when the extra-path length travelled by the beam across the films is a multiple m of the wavelength λ .

Due to the multiple reflections, the colour produced by multi-layer interference is more intense than the colour produced by thin-film interference, and it depends on the thickness of the two layers, the refractive index of the materials and the viewing angle of the observer, giving rise to the phenomenon of iridescence.⁵

Iridescence occurs when the colour observed changes according to the viewing angle and the spacing d between planes or interfaces.⁵ This is due to the different angles of reflection and refraction for different wavelengths of light. When white light interacts with a thin layer, light at the violet-end of the visible spectrum is reflected with larger angles than light at the red-end of spectrum.

Since the distance that the light travels when reflecting at the two interfaces of a thin layer depends on the angle of incidence and the layer thickness d , the conditions for constructive interference change accordingly.⁵

DIFFUSE OR INCOHERENT REFLECTION.

When light interacts with a smooth surface, as in the cases described above, light is coherently reflected along a specular direction, with an angle of reflection equal to the angle of incidence.

However, when light interacts with surfaces of increasing roughness, a fraction of the incident light is reflected in directions other than the specular one. This fraction is defined as **diffuse or incoherent reflection**.²¹

When the magnitude of the diffused reflection is so significant that the specular component can be neglected, then the surface is considered to be a rough or matt surface.

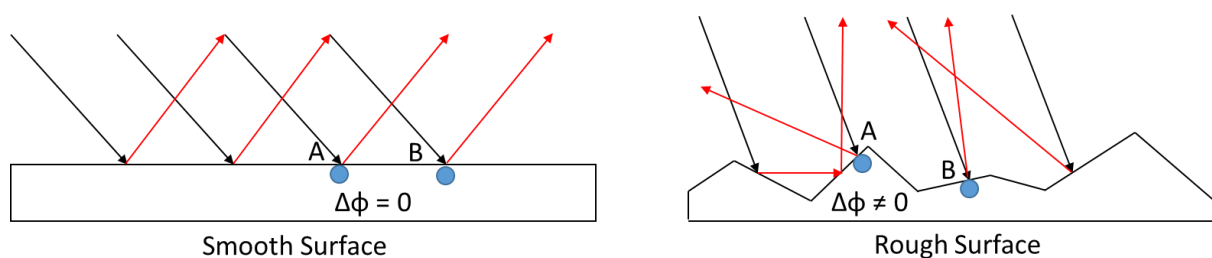


Figure 4: A smooth surface (left) producing coherent reflection. The phase difference $\Delta\phi$ between two parallel light waves reflected at random points A and B would be equal to zero, producing coherent reflection, since the height difference between the two points $|A - B|$ is equal to zero (eq. 10). A rough surface (right) producing incoherent reflection. The phase difference $\Delta\phi$ between two parallel light waves reflected at random points A and B would be different from zero (eq. 10), since the height difference between the two points $|A - B|$ is \neq zero. For a small degree of roughness $\Delta\phi \ll \pi$ the reflected waves in the specular direction will be almost in phase and will produce constructive interference. For a significant roughness $\Delta\phi \approx \pi$ the waves will be out of phase, determining destructive interference.

When parallel beams of light interact with a rough surface, each beam behaves accordingly to the law of reflection, with the angle of reflection being equal to the angle of incidence: but since contiguous sections of the surface have different orientations, the reflected beams are all oriented in different directions, producing incoherent reflection.²¹

A description of diffuse reflection may be given considering a system constituted by a rough surface. Any two points may be chosen on the surface and labelled A and B. When two parallel beams interact with the surface at these points, different scenarios may take place: the reflected light waves on the specular direction may be in or out of phase.²¹

The phase difference $\Delta\phi$ between the two waves is given by the equation:²¹

$$\Delta\phi = 2 |k| |A - B| \cos \theta_0 \quad \text{Equation 10}$$

where $|k|$ is equal to $2\pi/\lambda$ and is defined as the modulus of the wave vector of the incident light of wavelength λ , while θ_0 is the angle of incidence measured from the normal line.²¹

If the surface is smooth, the height difference between the two points $|A - B|$ is equal to zero, therefore the phase difference $\Delta\phi$ of the waves in the specular direction is also equal to zero and it is independent of the angle of incidence.²¹

If the surface is rough,²⁰ then $\Delta\phi \neq 0$. For a small degree of roughness $\Delta\phi \ll \pi$ the reflected waves in the specular direction will be almost in phase and will produce constructive interference.²¹

For a significant roughness $\Delta\phi \approx \pi$ the waves will be out of phase, determining destructive interference.²¹

$\Delta\phi = \pi/2$ is known as the Rayleigh criterion and is generally considered as the threshold for roughness. When $\Delta\phi < \pi/2$ the surface is smooth; when $\pi/2 < \Delta\phi \leq \pi$ or $\Delta\phi > \pi$ the surface is rough.²¹

DIFFRACTION.

When a beam of light interacts with an obstruction with dimensions comparable to the wavelength of the propagating light, a scattering phenomenon takes place, defined as **diffraction**.²⁰

This phenomenon is easily observed when a beam of light interacts with a diffraction grating, an object in the form of a sheet of transparent material such as glass or a polymer, with a large number of parallel grooves on it. The behaviour of light is similar to what observed for the double-slit experiment.²⁰ The scenario in Figure 5 illustrates the diffraction produced by a grating with slits of width s and placed at a distance d :²⁰

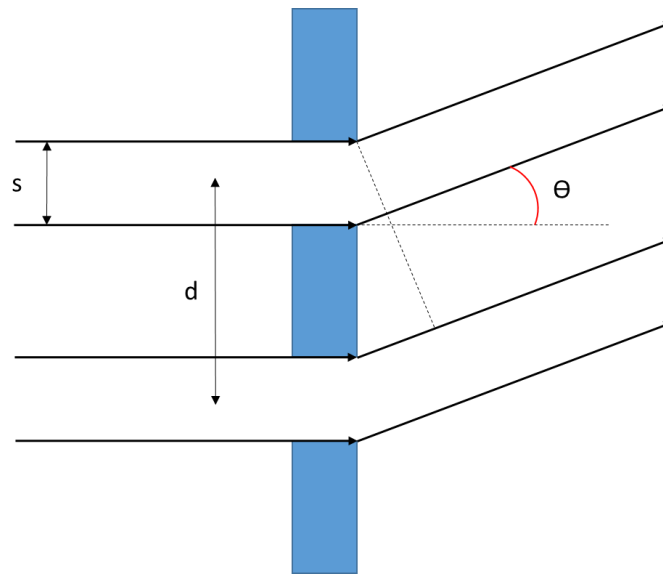


Figure 5: A diagram of a diffraction grating with slits of width s separated by a distance d . The diffraction angle is represented by θ .

When the beam of light is normally incident on the grating, the diffraction produces maxima at an angle θ , according to the relation:²⁰

$$d \sin \theta = m \lambda \quad \text{Equation 11}$$

where d is the distance between the slits, λ is the wavelength and m an integer number.

If the incident beam has an angle of incidence α , then the equation describing diffraction is modified as:²⁰

$$d (\sin \theta + \sin \alpha) = m \lambda \quad \text{Equation 12}$$

In the case of multiple slits on the diffraction grating, the intensity distribution I_θ of the diffracted beams is given by:²⁰

$$I_\theta = I_0 \frac{\sin^2 \left(N \frac{\pi}{\lambda} d \sin \theta \right)}{\sin^2 \left(\frac{\pi}{\lambda} d \sin \theta \right)^2} \quad \text{Equation 13}$$

where I_0 is the intensity of the incident beam, N is the number of slits, d the distance between slits. The total intensity distribution for the diffraction phenomenon is given by the contributions of both diffracted beams and interference. Therefore the above equation is modified to include interference, as:²⁰

$$I_\theta = I_0 \frac{\sin^2 \left(\frac{\pi}{\lambda} s \sin \theta \right) \sin^2 \left(N \frac{\pi}{\lambda} d \sin \theta \right)}{\left(\frac{\pi}{\lambda} s \sin \theta \right)^2 \sin^2 \left(\frac{\pi}{\lambda} d \sin \theta \right)^2} \quad \text{Equation 14}$$

The intensity is proportional to $\sin^2 \left(N \frac{\pi}{\lambda} d \sin \theta \right)$ which means that the intensities of the principal maxima are proportional to the square of the number of slits N . Increasing the number of slits produces narrower maxima with higher intensity, with blue light nearer to the direction of the incident beam and red light further away.²⁰

PHOTONIC CRYSTALS.

When EM radiation is incident on a crystal with crystallographic planes in the lattice separated by a distance d , a phenomenon of constructive interference takes place. Materials exhibiting this effect are referred to as **photonic crystals**.^{22 23} In a scenario where two waves, labelled 1 and 2, in phase with each other, are incident on a photonic crystal with crystallographic planes at a distance d and are scattered by scatters A and B on two parallel crystallographic planes, as described in Figure 6,

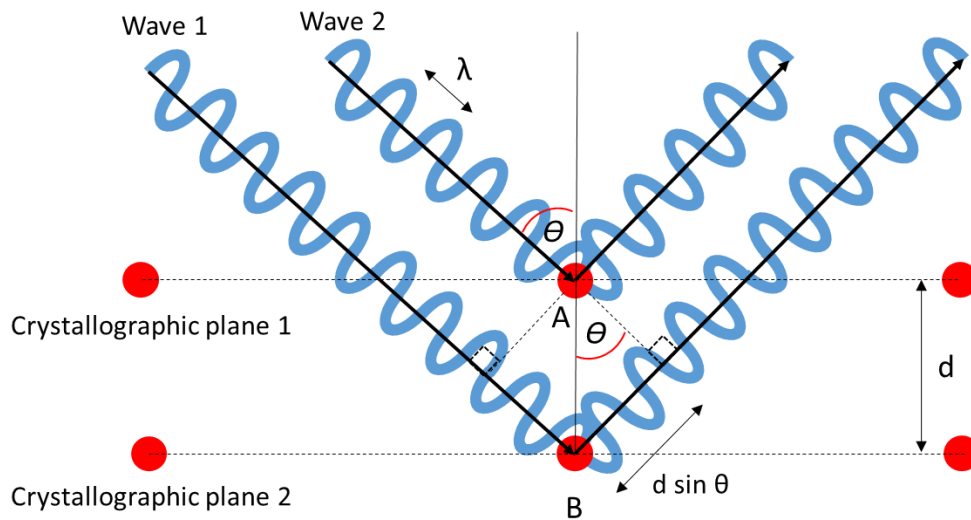


Figure 6: Constructive interference generated by the interaction of light with a photonic crystal. Waves 1 and 2 are scattered by scatters A and B respectively, located in two parallel crystallographic planes at a distance d . The conditions for constructive interference are described by the Bragg's Law (eq. 15): the light interacting with the second plane travels a longer path length, equivalent to twice the distance d between the planes multiplied by $\sin \theta$.

the conditions for constructive interference are described by the Bragg's Law:²²

$$2 d \sin \theta = m \lambda \quad \text{Equation 15}$$

where m is an integer number.

The light interacting with the second crystal plane travels a longer path length, equivalent to twice the distance d between the planes multiplied by $\sin \theta$.²²

LIGHT SCATTERING.

Light scattering can be defined as the **change of direction and intensity** of a light beam due to its interaction with an object. Scattering is the result of the combined effects of the phenomena of light reflection, refraction and diffraction previously described (Figure 7).¹⁹ A comprehensive theory describing light scattering as the result of the interaction of a light beam with spherical particles was formulated by Gustav Mie and it is generally referred to as Mie scattering. This theory accurately predicts the **angle and the intensity** of the scattered light beam, due to the light – particle interaction.¹⁹

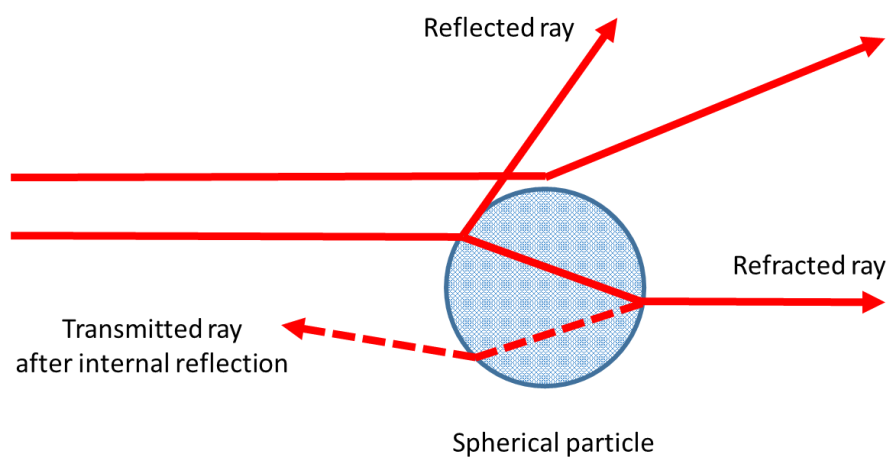


Figure 7: The interaction of a light beam with a spherical particle. Scattering is defined as the change of direction and intensity of a light beam and can be interpreted as the result of the combined effects of light reflection, refraction and diffraction. A fraction of the light is also transmitted after internal reflection. Adapted from “A Primer on Particle Sizing by Static Laser Light Scattering” by P. Webb.¹⁹

In order to simplify the description of light scattering, a series of constraints and conditions are applied. Mie theory only considers the scattering from spherical, isotropic particles and the incident light is considered to be monochromatic and composed of only plane waves. Only the scattering derived from the primary light source (defined as single scattering) is taken into account, leaving out the effects of multiple scattering, which include the light scattered from neighbouring particles.¹⁹

Only static elastic scattering is considered, therefore the effects of particles motion are ignored, along with Raman (inelastic scattering) and Doppler contributions.¹⁹

The phenomenon of light absorption is important in determining the intensity of the scattered light. Light absorption occurs when the atomic excitation promoted by the energy of the photons is dissipated by random atomic motion or in the form of thermal energy, rather than by photon re-emission.¹⁹ The reduction in energy of the incident beam is defined as light extinction, which is the degree of attenuation of the incident light energy. Light extinction is given by the sum of the

contributions of both scattering and absorption phenomena.¹⁹ Mie theory demonstrates that the intensity of the scattered light is a function of the light wavelength, the scattering angle, the particle size and the difference in refractive index between the particles and the surrounding medium.¹⁹ The theory clearly highlights an **angular dependence of the intensity of the scattered light for various particles' size** (Figure 8).⁵ In particular, with increasing particles' size, the scattering becomes anisotropic: a preferential direction is clearly observed, with the forward scattering being dominant.⁵

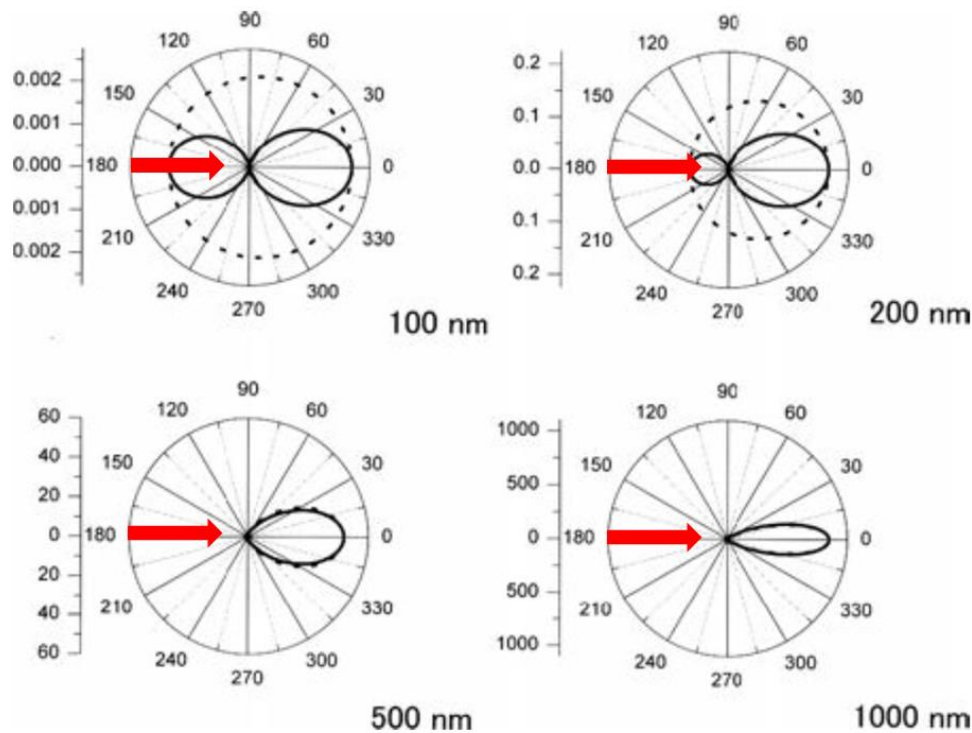


Figure 8: The diagram shows the angular dependence of the intensity of the scattered light for various particles size, as demonstrated by the Mie scattering theory. With the increasing radius of the spherical particles, the scattering progressively becomes more anisotropic. A forward preferential direction can be clearly observed. The scattering is nearly isotropic for spherical particles of 100 nm radius. It becomes anisotropic for particles with 200, 500 and 1000 nm radii. The simulation considers a sphere with refractive index of 1.5, a medium with refractive index of 1.33 and light with wavelength of 500 nm. The arrow shows the direction of the incoming wave. Reprinted from "Structural Colour In The Realm Of Nature" by S. Kinoshita, World Scientific, 2008.⁵

Mie theory also shows a **wavelength dependence of the intensity of the scattered light for various particles' size**.⁵ In a plot of scattering intensity vs wavelength (Figure 9) it can be clearly observed that, as the particles size progressively increases, a peak occurs in the visible region of the spectrum. This means that Mie scattering directly contributes to colour and that the colour is dependent on the size of the particles.⁵ Particles with a small radius would scatter violet - blue light, while with increasing radius the peak broadens and shifts towards longer wavelengths. If a scattering material is

composed of particles with a broad size distribution, then the scattered light would encompass the entire visible spectrum producing white colour.

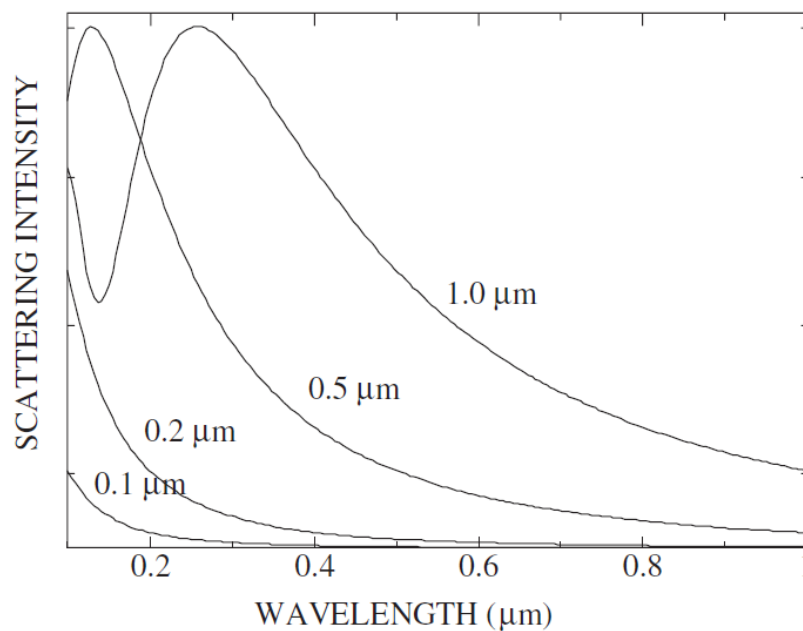


Figure 9: The diagram shows the wavelength dependence of the intensity of the scattered light for spherical particles of various size. As the particles radius increases, a peaks emerges in the visible spectrum, meaning that the scattering directly contributes to the colour. The simulation shows the scattering intensity for spherical particles of 0.1, 0.2, 0.5 and 1.0 μm , assuming that the particles have a refractive index of 1.5, are in a medium with refractive index of 1.33 and the incident light has a wavelength of 500 nm. Reprinted from “Structural Colour In The Realm Of Nature” by S. Kinoshita, World Scientific, 2008.⁵

Mie scattering is considered to be the cause of the structural colouration observed in a large variety of biological tissues. In particular it is associated to non-iridescent structural colour, due to the intrinsic irregularity of the structures involved.⁵ It is important to note that often the Mie scattering observed in biological samples is not due to spherical particles, but rather to spherical voids present within the tissues (Figure 10). The behaviour of the light interacting with a spherical void embedded in a biological medium is analogous to the light – particle interaction previously described, therefore Mie scattering can be perfectly applied to this type of systems.⁵

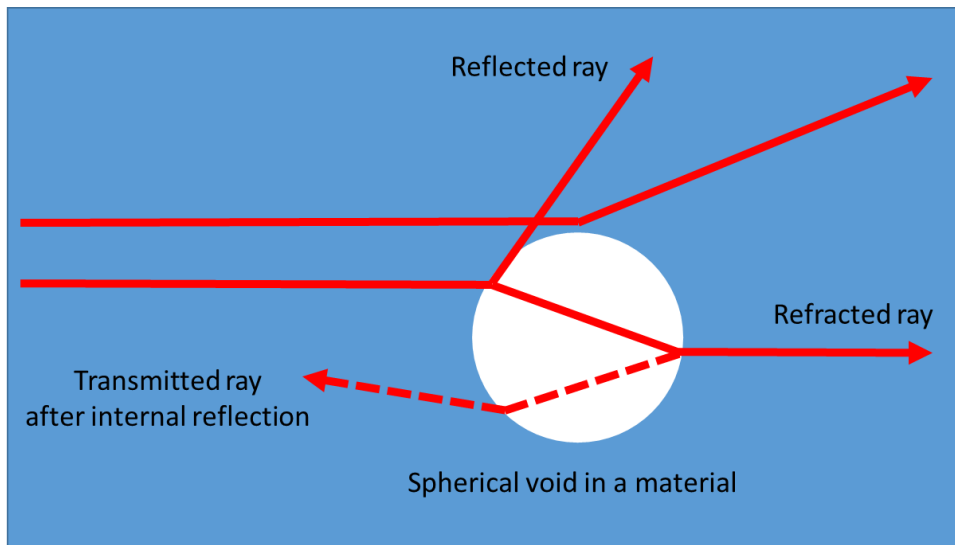


Figure 10: A sketch representing the interaction of a light beam with a spherical void within a material. The light behaviour is analogous to that shown for light – particle interaction (Figure 7). This type of system is more representative of biological tissues that exhibit evidence of structural colour due to Mie scattering.

A special case of the Mie scattering theory is known as **Rayleigh scattering** and it occurs when the EM radiation interacts with particles that are significantly smaller than light wavelength (in the order of one tenth of λ).²⁰ Rayleigh scattering is a type of elastic scattering, where the kinetic energy of the wave is conserved. When the oscillating electric field of the light wave interacts with the electric field of a particle, it induces the electric charges within the particle to oscillate at the same frequency of the wave. As a result, the particle becomes a radiating dipole, and the radiation emitted is observed as scattered light.²⁰

The intensity of the scattered light is related to the size of the scattering particles and it is described by the Rayleigh equation:²⁰

$$I = I_0 \frac{1 + \cos^2 \theta}{2 R^2} \left(\frac{2 \pi}{\lambda} \right)^4 \left(\frac{n^2 - 1}{n^2 + 2} \right)^2 \left(\frac{d}{2} \right)^6 \quad \text{Equation 16}$$

where I_0 is the intensity of the incident light, λ is the wavelength, θ is the scattering angle, n is the refractive index of the particles, d is the diameter of the particle and R is the distance from the particle to the detector. The equation exhibits a strong **wavelength dependence of the scattering** in the order of λ^{-4} implying that light of shorter wavelength would be scattered more strongly than light of longer wavelength.²⁰

The Rayleigh equation can be adjusted to account for the scattering from molecules, by expressing the refractive index n in terms of molecular polarizability α . The equation 16 is thus modified into:²⁰

$$I = I_0 \frac{8 \pi^4 \alpha^2}{\lambda^4 R^2} (1 + \cos^2 \theta) \quad \text{Equation 17}$$

Thus, due to a wavelength dependence of the scattered intensity, atmospheric dust scatters shorter wavelength of the sun light spectrum stronger, producing the blue colour of the sky.

Both Mie and Rayleigh scattering, due to the intrinsic irregularity of the scattering medium, such as disordered arrays of particles, are optical phenomena that produce non-iridescent structural colour, in contrast to the other mechanisms described such as multi-layer interference, diffraction, photonic crystals, where the regularity of the structures gives rise to iridescence.²⁰

CHAPTER 2: STRUCTURAL COLOUR IN NATURE.

Colour is an essential feature of living organisms. Animals and plants often display vivid and bright colours in their plumage, membranes or exoskeletons, sometimes with complex characteristic patterns associated with particular species or families.⁵

It is believed that colour plays a key evolutionary role in the animal kingdom, driving sexual selection, facilitating species recognition or favouring camouflage dynamics.¹⁷

In some cases, these bright colours are due to the presence of pigments in the organic tissues. Pigments produce colour by wavelength selective absorption: the incident light is absorbed by the molecule allowing the excitation of electrons to higher energy molecular levels. The photons whose energies are insufficient to fill the orbitals energy gaps are reflected or transmitted.⁵

In other cases, the colour observed is the result of the purely physical phenomena described in the optics section. Sometimes a combination of both is possible, like in the case of the green feathers of some species of parrots, where the colour is the results of yellow pigments and blue structural colour produced by scattering.⁵ It is important to highlight that structural colour is observed everywhere in the natural kingdom: it is present in plants, contributing to the colouration of flowers and fruits; it is present in both terrestrial and aquatic animal life.¹⁷ In this chapter three major classes of animals (butterflies, beetles and birds), which exhibit striking structural colouration, have been selected, and the structures that generate either iridescent or non-iridescent colour effects are investigated.

BUTTERFLIES.

Lepidoptera, colloquially referred to as butterflies, are a group of insects that include hundreds of thousands of species classified into 46 super-families.⁵ Due to the bright colours displayed on the large wings and often result of structural colouration, Lepidoptera have been extensively studied from an optical point of view.^{24 25}

All the Lepidoptera species present large wings compared to the body; the wings are covered by scales with average dimensions of 0.2 mm in length, 0.1 mm in width and 0.003 mm in thickness.⁵ The scales overlap slightly. If observed in detail under an electronic microscope, the Lepidoptera scales may be classified into two main types: the cover scales, with different shapes and sizes, which are specialised to perform several mechanical tasks, and the ground scales, with a more consistent rectangular shape.^{26 25}

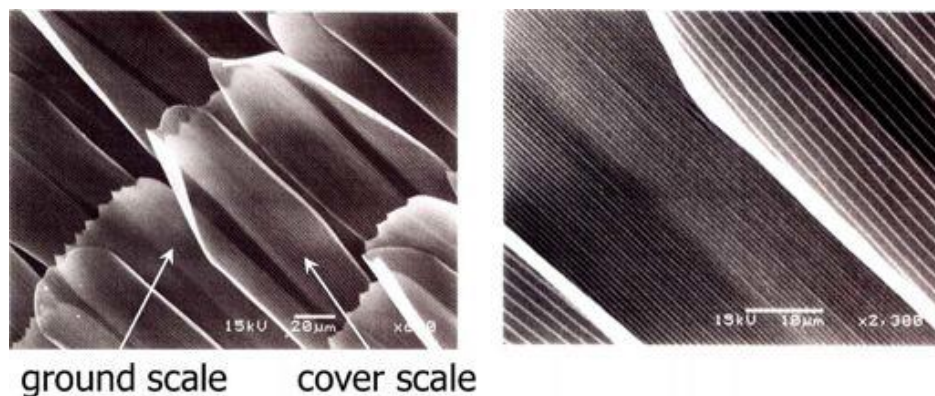


Figure 11: SEM images of ground and cover scales in the *Morpho didius* butterfly. Reprinted from "Structural colours in nature: the role of regularity and irregularity in the structure. Kinoshita and Yoshioka, 2005".²⁷

The microscopic structure of the scales is constituted by a series of parallel ridges that are supported by a number of small pillars, defined as micro-ribs. The ridges are connected together by arch-like structures named cross-ribs, which run perpendicular to the ridges.

The whole framework of ridges, micro-ribs and cross-ribs is finally held firm together by larger connecting structures named trabeculae.²⁸

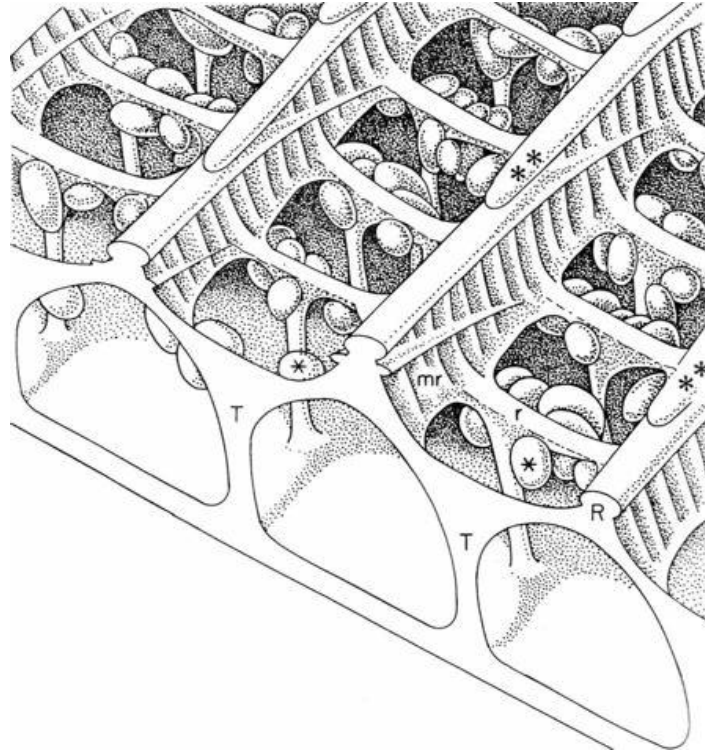


Figure 12: Overview of the microscopic structure of a Lepidoptera scale. The connecting underlying structure defined as trabeculae is highlighted (T). The ridges (R) are supported by the trabeculae and by the micro-ribs (mr). The arch-like structures, cross-ribs (r), connecting the parallel ridges are also represented. Reprinted from "Light and colour on the wing: structural colours in butterflies and moths. Ghirardella, 1991.²⁹

The interaction of light with this regular periodic ladder-like structure present in the scale architecture is responsible for the structural colourations.

One of the most scenic and studied class of butterflies is the *Morpho*, native of South America. These butterflies exhibit, for the male exemplars, a bright metallic blue colour with iridescent effects.²⁶

The distance between the ridges in the *Morpho* butterflies varies according to the species. For example, it is 1.0 μm for *Morpho sulkowskyi* and 0.7 μm for *Morpho rhetenor*. The blue structural colour is produced by the cover scales, while the ground scales beneath are pigmented and present a dark brown colour.⁵

In order to understand the mechanism of the blue colour, it is necessary to look in detail at the cross section of the ridges. If a scale is sliced, it is possible to observe that a ridge has a height of approximately 2.0 μm and it is 0.3 μm in width. The key feature of the structure is the conformation similar to a book-shelf library: each ridge presents about 6 or 7 shelves with a thickness of 0.05 to 0.07 μm . The distance between the shelves is of approximately 0.2 μm .²⁶

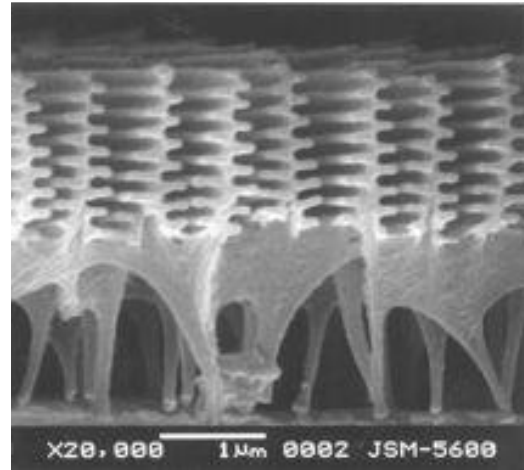


Figure 13: A *Morpho rhetenor* butterfly displaying a bright blue colour in the large wings (left). On the right, a SEM image of a cross-section of a ridge in the scale of *Morpho* butterfly. The book-shelf structure, responsible for multi-layer interference, is clearly visible. Reprinted from "Structural Colour In The Realm Of Nature" by S. Kinoshita, World Scientific, 2008.⁵

This configuration of the ridges operates like a multi-layer interference structure described in the optics chapter (Figure 3): the spacing between the shelves (≈ 200 nm) and the shelves' thickness (50 - 70 nm), along with an average refractive index for the shelves of $n \approx 1.2$ and the air with $n = 1.0$, accounts for a constructive interference of reflected light for wavelengths around 460 nm, in the blue zone of the visible spectrum.²⁶ This small difference in refractive index ($\Delta n \approx 0.2$) is sufficient to produce the prominent colour observed.

The presence of pigments in the ground scales that lie beneath the cover scales is also important, since these pigments provide to the absorption of light of other wavelengths reflected at different angles, enhancing the richness of the blue colour.²⁶

Measurements on the *Morpho* butterflies scales, to determine the angular dependence of the reflected light according to the viewing angle, were performed on *Morpho adonis* and *Morpho sulkowskyi* species. A spectrometer operating with an incident angle of -45° and a detection angle of $+30^\circ$ was employed, and the butterfly scales were tilted from an angle of -90° to $+90^\circ$. The experiment showed that the reflected light ranged from wavelengths of 380 nm to 580 nm, with a maxima of 460 nm for the *Morpho sulkowskyi* and 482 nm for the *Morpho adonis*.⁵

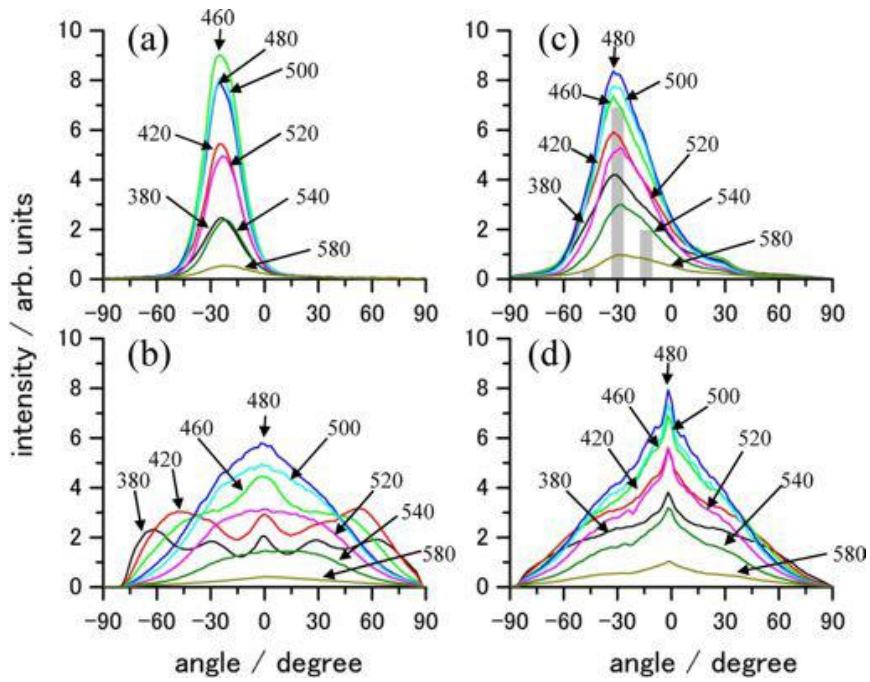


Figure 14: Reflectance measurements of the wing of a *Morpho* butterfly. The diagrams show the angular dependence of the reflected light intensity under monochromatic light illumination between 380 and 580 nm. Diagrams (a) and (c) represent measurements within a plane parallel to the ridge; diagrams (b) and (d) represent measurements within a plane perpendicular to the ridge. The maxima at 460 – 480 nm are evidence for the constructive interference of the blue light. Reprinted from “Wavelength-selective and anisotropic light-diffusing scale on the wing of the *Morpho* butterfly. Yoshioka and Kinoshita, 2004”.³⁰

A theoretical model built from the *Morpho* butterflies scales, consisting of shelves of refractive index 1.60 separated by a distance d of 200 nm, produced diffused reflection in the wavelength range of 400 nm to 550 nm with a maxima at 480 nm. Increasing the number of shelves from 3 to 6 and then to 9 had the effect of producing narrower peaks, sharpening the blue colour.²⁶

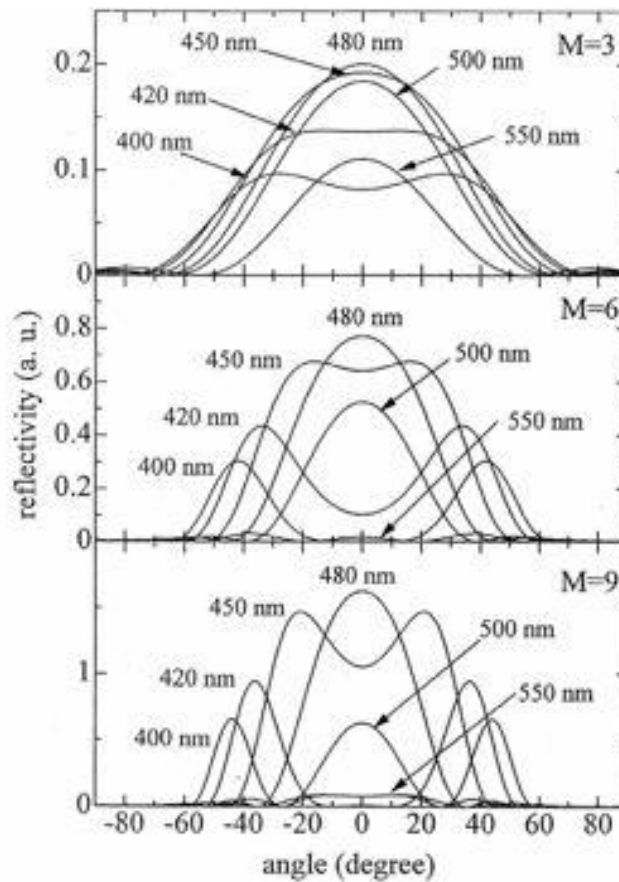


Figure 15: Diagrams showing the reflectance from a theoretical model based on the *Morpho* scale, with shelf-structures of refractive index of 1.60 separated by a distance d of 200 nm. The model produced diffused reflection in the wavelength range of 400 nm to 550 nm with a maxima at 480 nm, similar to the real-life structure measured in Figure 14. Increasing the number of shelves from 3 to 6 and then to 9 had the effect of producing narrower peaks, sharpening the blue colour. Reprinted from "Structural Colour In The Realm Of Nature" by S. Kinoshita, World Scientific, 2008.⁵

Simpler experiments performed on the wings of the *Morpho* butterflies also confirmed the structural colouration as the effect of multi-layer interference. For instance, changing the refractive index of one of the medium (the air between the shelves of the scales) by immersing the wings into different liquids, resulted in a rapid change in the colour observed. Ethyl alcohol with a refractive index of 1.36 produced green (Figure 16), while using toluene with a refractive index of 1.50 changed the colour into a dark brown.⁵



Figure 16: Colour change of a *Morpho didius* wing from blue when in air (left) to green when in ethyl alcohol (right). Reprinted from "Structural Colour In The Realm Of Nature" by S. Kinoshita, World Scientific, 2008.⁵

BEETLES.

Coleoptera, usually referred to as beetles, are a class of insects that present large variations in the coloration of their exoskeletons, often exhibiting vivid and bright colours. The most common mean of achieving colour in beetles is by multi-layer interference: periodic structures consisting of alternate layers of different organic materials are found in the beetles elytra, producing iridescent structural colour.⁵

One of the most striking examples of structural colour by multi-layer interference is provided by the *Chrysochroa fulguidissima*, also known as the Jewel beetle. The Jewel beetle is a native species from Asia and its elytra have been used in Asian cultures for centuries in craft works and decorations.⁵

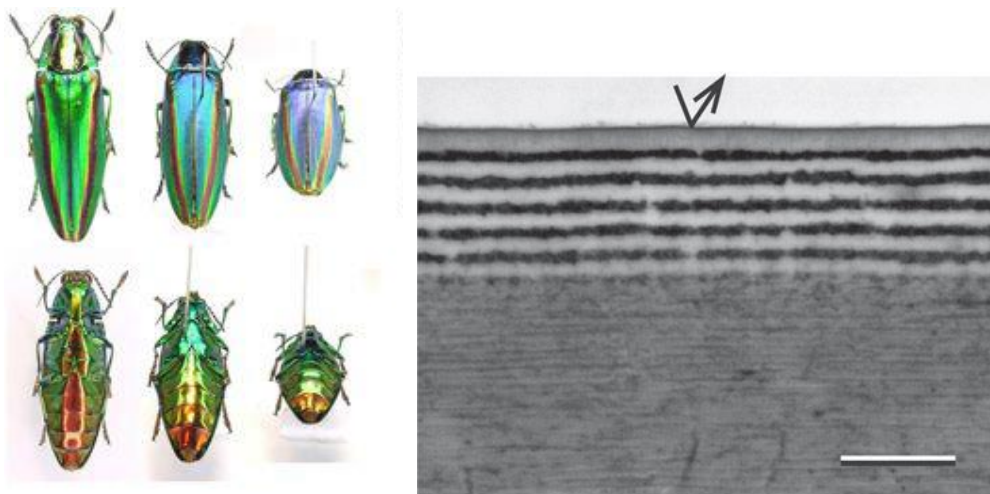


Figure 17: On the left an image of the *Chrysochroa fulguidissima* beetle, highlighting the iridescence in the dorsal and ventral regions as the viewing angle changes. On the right, a cross-section of *Chrysochroa fulguidissima* layered epicuticle, showing the alternate layered structure giving rise to the iridescence. Scale bar = 1 μm . Reprinted from "Polarized iridescence of the multi-layered elytra of the Japanese jewel beetle, *Chrysochroa fulguidissima*" by Stavenga et al.³¹

The dorsal side of the Jewel beetle exhibits a metallic green colour, only interrupted by two reddish-brown stripes. When changing the viewing angle, the colour gradually changes from green to blue. Iridescence is also present in the ventral area, where at different angles the colour shifts from brown to green.⁵ Electron microscopy on the elytra were performed on a section of 1.3 μm in thickness: a series of alternate layers with different electron densities were observed.³¹ In the green section of the elytra, 16 layers were identified with thicknesses d_1 of 82 nm and d_2 of 78 nm and refractive index n_1 of 1.59 and n_2 of 1.67. The small difference in refractive index ($\Delta n \approx 0.08$) is enough to produce the impressive colour effect with a maxima at $\lambda = 520$ nm. In the red stripes a lower number of 12 layers was observed, with slightly larger thickness d_1 of 105 nm and d_2 of 100 nm and refractive

index n_1 of 1.60 and n_2 of 1.68. The difference in refractive index is unchanged, but the increase in the layers thickness favours the constructive interference of red light with a maxima at $\lambda = 670 \text{ nm}$.³¹

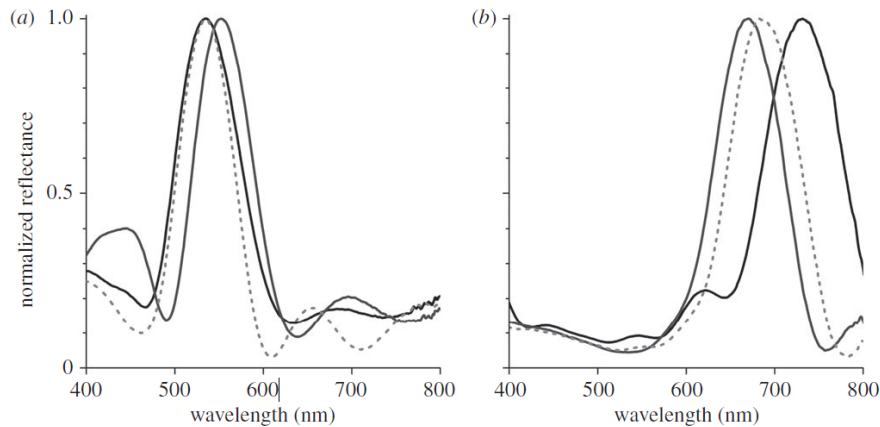


Figure 18: Diagrams showing the reflectance spectrum for (a) green (maxima at $\approx 520 \text{ nm}$) and (b) red/purple (maxima at $\approx 670 \text{ nm}$) regions of the *Chrysochroa fulguidissima* beetle's elytra. Reprinted from "Polarized iridescence of the multi-layered elytra of the Japanese jewel beetle, *Chrysochroa fulguidissima*" by Stavenga et al.³¹

Similar structural configurations producing iridescence are observed in other species of beetles. The *Plateumaris sericea* or Leaf beetle also displays beautiful metallic-like colourations.⁵ The three most common specimens have a blue, bronze or red exoskeleton. The colours are produced by three layers of two organic materials with refractive index of 1.73 and 1.40. The difference in the colour produced is due to the different thickness of the layers: 60 to 100 nm for the blue, 70 to 160 nm for the bronze and 100 to 140 nm for the red beetle.⁵

Multi-layer interference is the most common strategy to achieve structural colour for beetles. However other structures have been observed that are able to obtain a completely different effect, producing **non-iridescent structural colour**, and in particular broad-band reflectors capable of scattering light in the entire visible range, appearing white.³²

In order to achieve a bright white appearance all the wavelengths in the visible range must be scattered with the same efficiency. Structures able to do so are defined as broad-bands reflectors.³² This goal cannot be obtained with optical coherent structures, as they would reinforce specific wavelengths and produce iridescence.

Whiteness requires significantly disordered structures that multiply the scatter of light. This is normally achieved by very thick systems where the light is progressively scattered as it travels deep into the structure and interacts with a large number of interfaces. The scattering medium must be randomly organised with randomly positioned scattering centres.^{6 33}

The importance of the beetle structures is due to the fact that they are capable of achieving **remarkable white with very thin systems**. This means that the beetle tissues evolved to maximise the amount of scattering in remarkably thin material.³⁴ It can be assumed that evolution engineered these organic tissues to provide the best possible scattering in the lightest possible structure, with very low mass per unit area, since low mass is absolutely crucial for flying insects.³⁴

One of the best examples of white is found in the *Cyphochilus* beetle. The body of the insect is covered in tiny white scales with average dimensions of 250 μm in length, 100 μm in width and an average of only 7 or 8 μm in thickness. The scales are made of chitin, a protein with a refractive index of 1.56. The difference in refractive index for the scales is therefore $\Delta n = 0.56$ and is sufficient to achieve the enhanced scattering observed. Another beetle species that presents thin white scales is the *Lepidiota stigma*, with an average thickness of 15 μm .³⁴

SEM performed on cross-sections of *Cyphochilus* and *Lepidiota stigma* (Figure 19) beetles highlighted the presence of an intricate, randomised and isotropic network of rod-like filaments of chitin.⁶

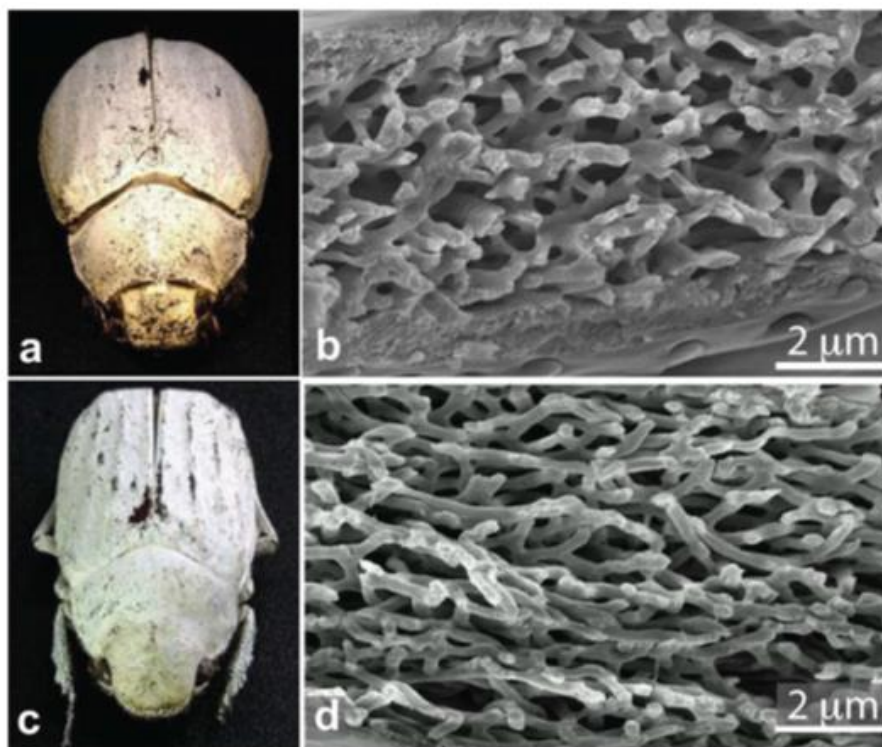


Figure 19: Images of *Lepidiota stigma* (a) and *Cyphochilus* (c) beetles. SEM of the cross-section of the scales of the *Lepidiota stigma* (b) and *Cyphochilus* (d) respectively. Intricate, randomised and isotropic network of rod-like filaments of chitin are clearly visible. Reprinted from "Bright-White Beetle Scales Optimise Multiple Scattering of Light" by Burrese et al.⁶

The filling fraction of chitin has been estimated in 50-60%, with the rest of the volume filled by air. In the *Cyphochilus* scales the chitin filaments present an average thickness of 244 ± 51 nm and are separated by voids with an average diameter of 580 ± 120 nm. In the *Lepidiota stigma* scales the average thickness of the chitin filaments is 348 ± 77 nm and the average diameter of the voids is 700 ± 180 nm.⁶

Spectroscopic measurements on scales belonging to these two species showed that they are able to reflect light across the entire visible spectrum with an efficiency of $\approx 70 - 80\%$.^{6 32}

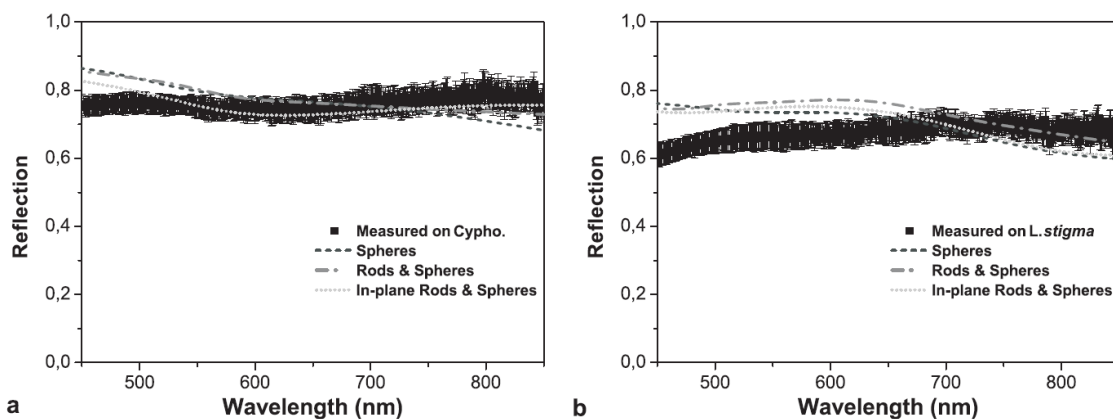


Figure 20: Reflection spectra of the white scales of *Cyphochilus* (a) and *Lepidiota stigma* (b). The experimental data (thick black line) showed that a single scale is able to reflect light across the entire visible spectrum with an efficiency of $\approx 70 - 80\%$, producing the whiteness observed. The dashed lined are predictions from mathematical models comprising only spheres; spheres and rods randomly oriented in a tri-dimensional space; spheres and rods with a random orientation in a plane. Reprinted from "Bright-White Beetle Scales Optimise Multiple Scattering of Light" by Burresi et al.⁶

From the analysis of the beetle scales, the researchers³² came to the conclusion that in order to design an efficient broad-band optical scatter, an optimum compromise between the number of scattering centres and their relative distance is necessary. If there are too many scattering centres per unit volume, this **optical crowding** would produce a reduction in scattering efficiency; the same occurs if the scattering centres are placed too far apart. The scales and their modelling suggests that an optimum structure would consist of randomly oriented scattering centres with a diameter of 200 to 300 nm and with an average relative distance of 500 nm.³²

BIRDS.

Another class of animals that is renowned for the beautiful display of flaring colours is that of birds. Across the numerous species, bird feathers present important examples of structural colour. As in the case of the beetles, it is possible to find structures that exploit different optical mechanisms to produce both iridescent and non-iridescent structural colour. The generic structure of bird feathers consists of a shaft that grows from the animal body and that branches into small filaments called barbs. The barbs in turn branch into even smaller filaments called barbules (Figure 21). The structures responsible for the optical properties are found in the barbules.⁵

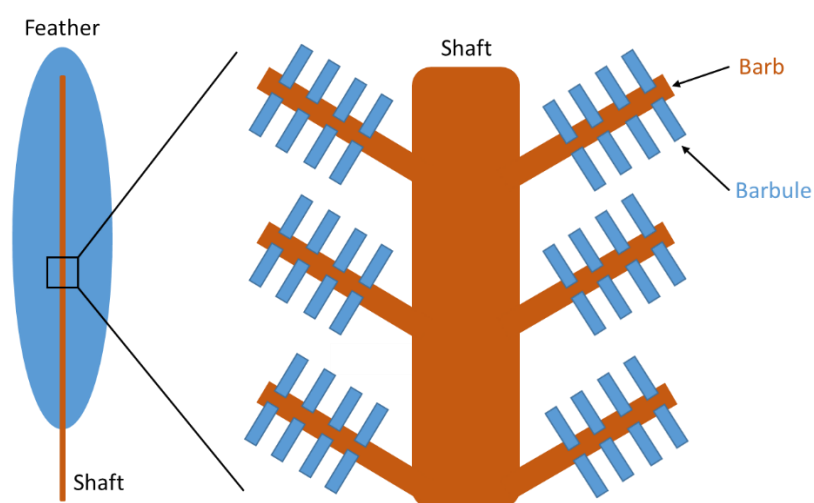


Figure 21: A sketch of the general structure of a bird feather. A shaft growing from the animal body branches into small filaments called barbs. The barbs further branch into even smaller filaments called barbules. The structures responsible for the colour observed are present in the barbules.

Since the early systematic studies on bird feathers employing SEM imaging, the presence of melanin granules with rod-like shapes in the barbule tissues was recorded. It was later understood that iridescent structural colour in a large number of bird species was due to the way these melanin rods were assembled.⁵

A classic example of iridescent structural colour in birds is provided by the *Pavo cristatus* (peacock). The barbules in a *Pavo cristatus* feather are made of layers of keratin with a thickness of 0.4 – 0.5 μm , surrounding a fibrous core of 2.0 μm . Within the keratin layers, melanin rods of about 1.0 μm in length are oriented parallel to the surface and regularly arranged in order to form a lattice with up to 11 layers of rods, as shown in the cross-section in Figure 22.^{35 5}

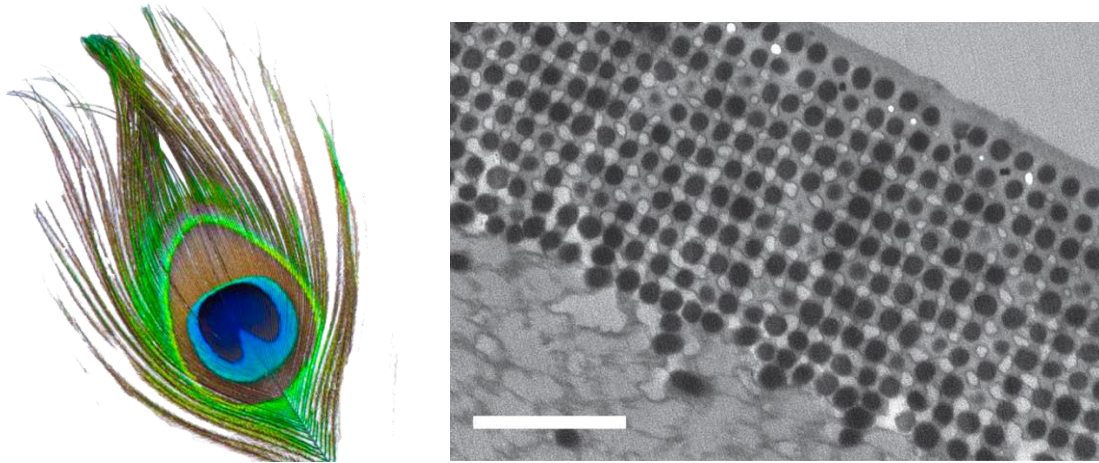


Figure 22: On the left an overview of a *Pavo cristatus* feather. On the right a TEM image of a cross-section of a *Pavo cristatus* feather. It is possible to observe the melanin rods (black dots) and the air holes (clear dots). Scale bar = 1 μm . Reprinted from "Light manipulation principles in biological photonic systems" by Starkey and Vukusic, *Nanophotonics*, 2013.³⁶

The melanin rods are kept in place by keratin bands. The rods are separated by air holes. The colour produced is controlled by the number of melanin rods layers in the lattice and by their separation distance due to the air holes.⁵

The dark blue colour in *Pavo cristatus* feathers is produced by 9 to 11 layers of melanin rods separated by air holes of 160 nm in diameter. Turkish green is given by 9 or 10 layers of rods with 170 nm of diameter for air holes. Red-brown requires fewer layers, 5 to 7, with a larger separation of 210 nm due to the air holes.⁵

Another example of iridescent structural colour in birds is provided by the hummingbirds. Similarly to what observed in the peacock feathers, melanin platelets arranged into regular arrays are found in the barbules of hummingbirds.^{5 37}

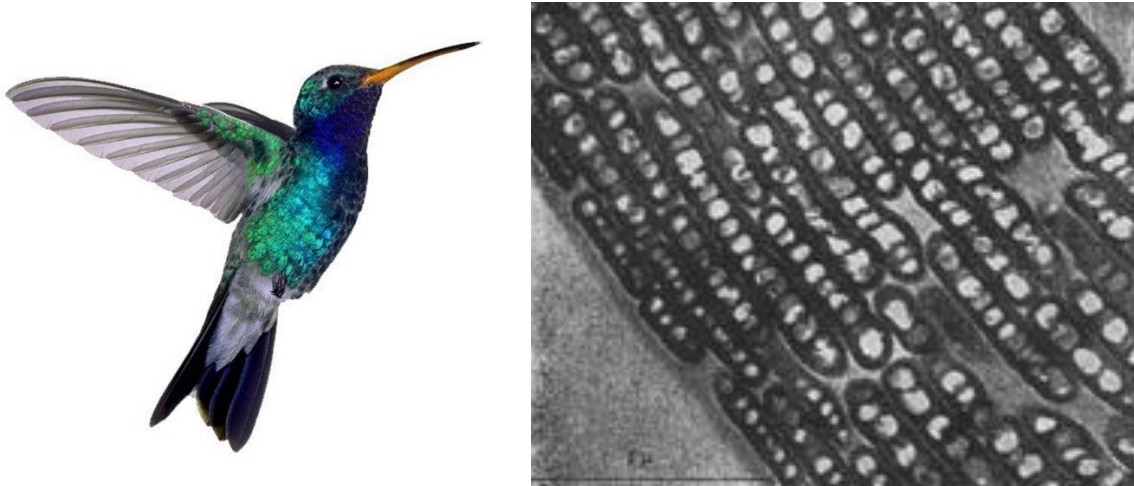


Figure 23: On the left an overview of a hummingbird. On the right a TEM image of a cross-section of a hummingbird feather. It is possible to observe the melanin platelets (in black). Reprinted from "Iridescent Colours of Hummingbird Feathers" by Greenewalt et al. 1960.³⁷

The melanin platelets are elliptical in shape and arranged into layers parallel to the surface of the barbule. The number of layers may vary according to the species from 7 to 15, with their thickness ranging from 100 to 220 nm. The platelets are separated by small pockets of air.⁵

The thickness of the melanin platelets and of the air pockets determines the colour observed. For example, the blue in the tail of the *Amazilia cyanura* hummingbird is produced by platelets of 32 nm in thickness spaced by air pockets of 123 nm.⁵

Non-iridescence structural colour is produced in birds by Rayleigh or Mie scattering, described in the optics section. SEM images of bird feathers exhibiting non-iridescent structural colour show structures consisting of air pockets in keratin networks, similar to **foams**. Some of the most representative examples are provided by the *Tangara mexicana* and the *Kingfisher*, which display bright blue non-iridescent colours, given by foam-like structures where spherical voids are embedded into the keratin matrix of the barbules.⁵

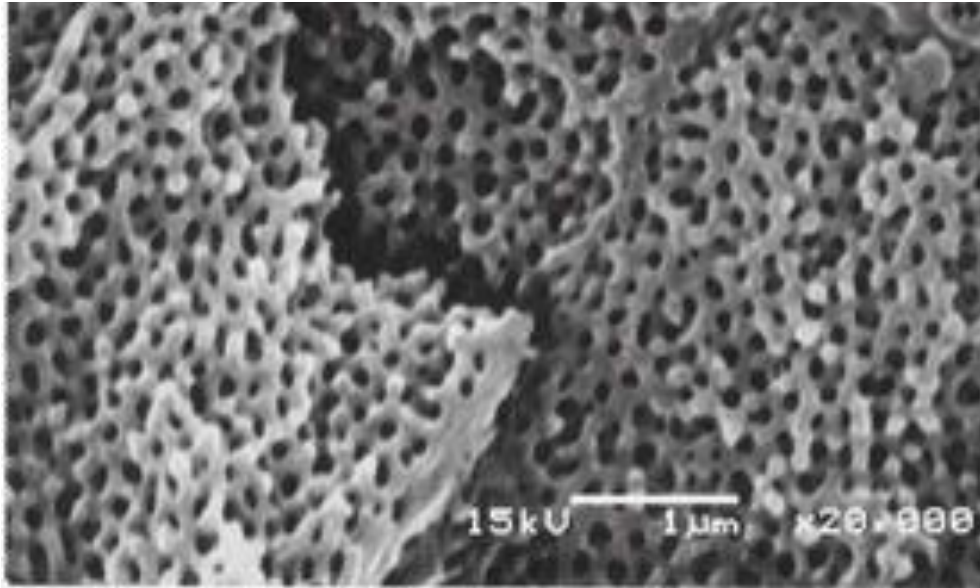


Figure 24: A cross-section of a barb of a Common kingfisher. The foam structure with pores of ≈ 200 nm in diameter is clearly visible. Reprinted from "Structural colours in nature: the role of regularity and irregularity in the structure. Kinoshita and Yoshioka, 2005".²⁷

Light is scattered at the keratin – air interfaces and the colour produced is related to the void size. Analysis on blue feathers in the *Jay*, *Cotinga* and *Ara* species showed that the average hole size in the foam structures is about 200 nm in diameter.⁵

Studies on the feathers of the *Agapornis roseicollis* by Dyck also highlighted a foam-like structure in the inner part of the barbs of this bird, presenting a tri-dimensional network where keratin rods of about 100 nm in thickness were spaced out by empty holes of 100 nm in diameter.⁵ Dyck investigated the internal structure of several other species and found that the thickness of the keratin rods and the diameter of the air pockets was quite consistent among the birds, while the random orientations of the rods was the reason for the lack of iridescence observed.⁵ Measurements of the reflected light from these structures showed that they act as broad-band scatters, able to scatter light from the ultraviolet to the blue. The feathers appear blue since that is the only portion of the reflected light detectable by the human eyes.⁵

The analysis of the foam structures allowed Dyck to produce a theoretical model, known as the "hollow cylinder model", for an ideal structure capable of producing non-iridescent structural colour. Hollow cylinders with diameters ranging from 200 to 400 nm randomly oriented within a keratin matrix would reproduce the same colour effects observed in those birds.⁵

Another interesting example of non-iridescent structural colour is provided by the *Garrulus glandarius* (Eurasian jay). The peculiarity of this bird is in the colouration of the feathers present on the wings, where a periodic shift from dark blue to light blue and to white is observed.³⁸



Figure 25: (a) An image of Jay feather, with a periodic colour pattern from white to dark blue. (b) Photograph of the *Garrulus glandarius*. Reprinted from “Spatially modulated structural colour in bird feathers” by Parnell et al.³⁸ Photograph of the Jay *Garrulus glandarius*: (Credit: Luc Viatour/www.Lucnix.be) this image is licensed under the Attribution-ShareAlike3.0 Unported license.

Research on the wing feathers clearly showed that the structure responsible for the range of colours is a thin layer of 10 μm covering the barbs. The research correlated the structural information obtained by SEM and SAXS with the periodic colours exhibited along the barbs.³⁸

Microscopy showed evidence of a foam-like structure with lack of a long range order, giving rise to the non-iridescent colour. The shift from blue to white along the barb is due to a change in size of the voids within the keratin network. A more regular foam-structure with air holes of about 130 – 170 nm in diameter was associated with the blue part of the Jay barb, while structures with higher degree of disorder and larger holes of about 200 – 210 nm in diameter corresponded to the white sections on the barb.³⁸

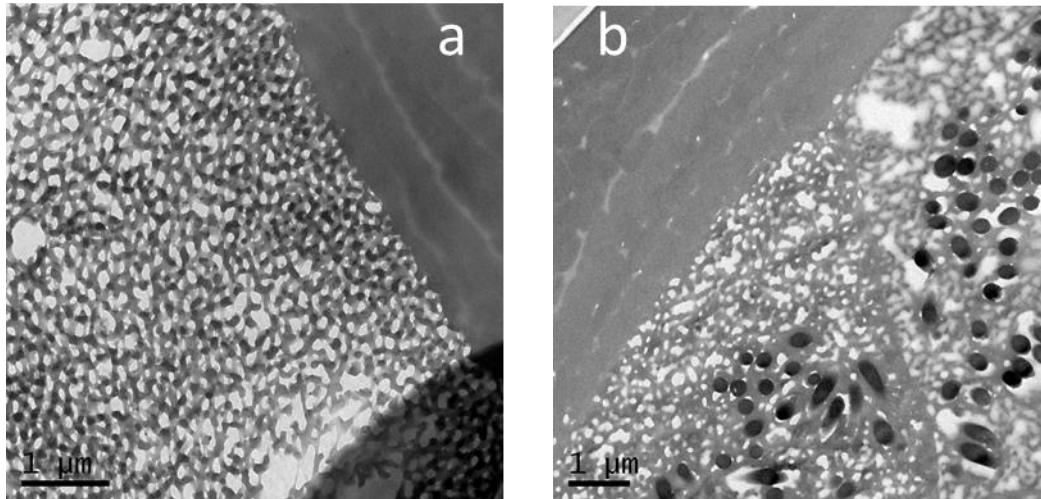


Figure 26: TEM images of cross-sections of Jay feathers. (a) a section of a blue region. (b) a section of a white region, with more irregular pores and larger voids distribution. The black dots are melanin granules. Reprinted from "Spatially modulated structural colour in bird feathers" by Parnell et al.³⁸

The research proposed the hypothesis that the foam structures observed in the Jay are achieved by a mechanism of spinodal decomposition, where the keratin medium undergoes phase separation over time.³⁸ This process, due to random fluctuations in the medium, produces domains with different keratin densities. As the phase separation proceeds, the amplitude of the fluctuation waves increases, resulting in domains which progressively grow in size. When the phase separation stops, the regions with high keratin density form the keratin matrix, while the regions with low keratin density produce the voids, which are then occupied by the air.³⁸ Since the domains of the structure change in size along the barb as the feather grows, it is speculated that the Jay must have a mechanism in place capable of arresting the process of phase separation at a desired time, in order to achieve the desired colour effect at the exact point along the barb.³⁸

The analysis of the structures explored in this section provides the necessary background to understand the elegant design behind the efficient structural configurations that give rise to structural colour in nature.

Since the objective of the project is the fabrication of synthetic broad-band scatterers in the form of polymeric micro-spheres, producing non-iridescent structural white, the target structures to consider are those observed in the white scales of the beetles and the white sections of the Jay feathers. The beetles exhibit intricate, randomised and isotropic networks of rod-like filaments of chitin separated by air voids. The *Cyphochilus* present chitin filaments with thickness of ≈ 240 nm and voids with a diameter of ≈ 580 nm.³² Models based on this type of network suggests that an

optimum structure would consist of randomly oriented filaments of chitin with diameters of ≈ 250 nm separated by voids of ≈ 500 nm.³² The non-iridescent feathers in birds showed foam-like internal structures with randomly oriented voids in a keratin matrix.^{5 38} Even though these structures tend to produce blue structural colour due to the small and consistent size of the voids between 100 and 200 nm,⁵ the white sections of the Jay barbs demonstrate that structural white is possible when the voids increase in size over 200 nm and present a greater size distribution.³⁸

CHAPTER 3: REPRODUCTION OF BIOLOGICAL STRUCTURES BY A PROCESS OF NON-SOLVENT INDUCED PHASE SEPARATION OF A HOMOGENEOUS POLYMER SOLUTION.

THERMODYNAMICS OF PHASE SEPARATION OF A POLYMER SOLUTION.

The core part of this project revolved around the identification of a chemical system that could reproduce either a network of the type observed in the *Cyphochilus* and *Lepidota stigma* scales³² or a foam structure of the type found in the *Garrulus glandarius*' feathers,³⁸ within spherical polymeric micro-particles.

An effective way of producing porous structures is based on the possibility of inducing phase separation in an initially homogeneous polymer solution.³⁹

The properties of dilute polymer solutions are determined by the interaction between the polymer and the solvent.⁴⁰ When a polymer is dissolved in a poor solvent, the intra-molecular interactions between the polymer chain sub-units dominate over the inter-molecular forces between the polymer and the solvent molecules. As a result of this phenomenon, the polymer chains tend to contract.⁴¹ In the opposite scenario, when a polymer is dissolved in a good solvent, the inter-molecular forces between the polymer and the solvent molecules are stronger than the intra-molecular interactions within the polymer chains. The polymer chains are able to expand and the swollen polymer occupies a larger volume.⁴¹

In an ideal polymer solution, where the intra-molecular forces between the polymer sub-units are perfectly balanced by the inter-molecular forces between polymer and solvent, the polymer chains behave like ideal random coils. Such a solvent is defined as a theta-solvent. The interaction forces between polymer and solvent are quantified by a parameter χ , known as the Flory-Huggis interaction parameter, which is a measure of the energy required to inter-disperse polymer and solvent molecules.^{41 40}

The thermodynamic behaviour of a polymer solution in theta conditions is related to the temperature of the system, the number of moles of polymer present in the system, the number of moles of the solvent, the volume fraction of the polymer, the volume fraction of the solvent and the interaction parameter between the polymer and the solvent.⁴²

The phase separation of a homogeneous polymer solution can be induced by a change in temperature (thermally induced phase separation, TIPS) or by the introduction of a non-solvent (non-solvent induced phase separation, NIPS).^{42 43}

Non-solvent induced phase separation is the process investigated in this work.

Every ternary system with polymer, solvent and non-solvent components has a unique characteristic phase separation behaviour that is related to the Flory-Huggins interaction parameter, the polymer molecular weight and the polymer concentration, the solvent to non-solvent ratio and their relative miscibility.

The behaviour of a ternary system can be generalised by a comprehensive isothermal phase diagram (Figure 27).⁴⁴ The binodal line marks the boundary between the one-phase region, where the system is a homogenous solution, and the two-phase region, where the system undergoes a liquid-liquid de-mixing and, as progressively more non-solvent is added, a solid-liquid de-mixing where the polymer precipitates.⁴⁴ The upper limit of the binodal is referred to as the critical point. The spinodal line is the boundary between metastable and unstable zones in the two-phase region. The critical point is also the point of interception between the binodal and the spinodal lines.⁴⁴

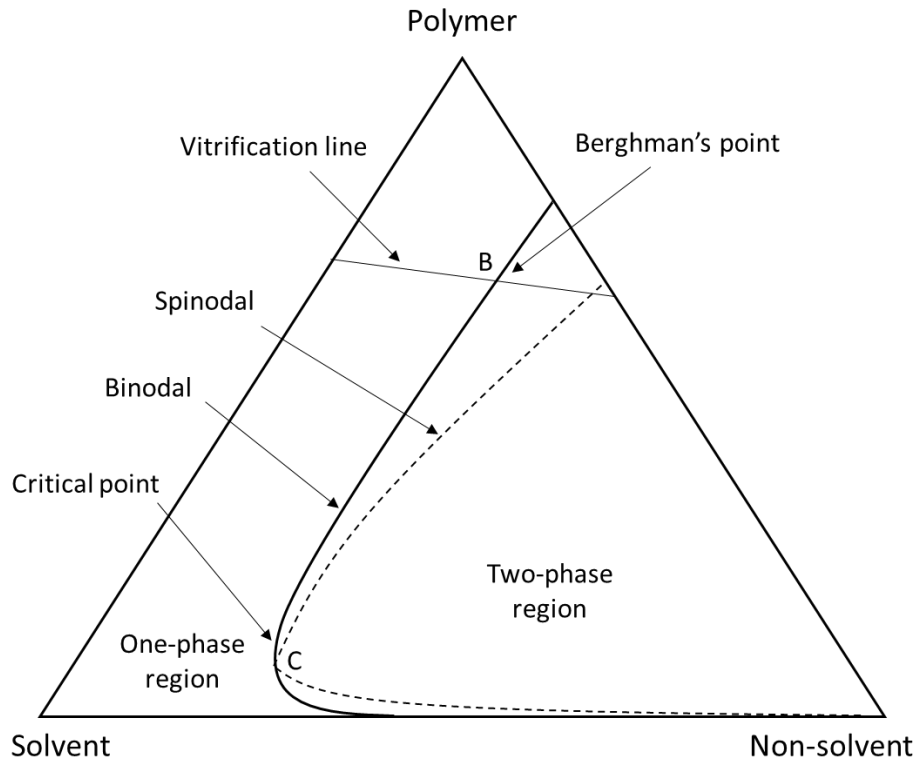


Figure 27: A general isothermal ternary phase diagram for a polymer-solvent-non solvent system. The binodal line marks the border between the one-phase region, where the system is a homogenous solution, and the two-phase region, where the phase separation produces a de-mixing of the solution into a liquid-liquid mixture and, with continuing quenching with the non-solvent, into a solid-liquid mixture with polymer precipitate. The spinodal line marks the boundary between the metastable regions, where phase separation occurs by a mechanism of nucleation and growth, and the unstable region where the phase separation takes place by spinodal decomposition. The binodal and spinodal boundaries meet at the critical point C. The Berghman's point⁴⁵ is at the interception of the binodal and the vitrification line, and marks the point where the polymer reverts to a glass. Adapted from "Evolution of polymeric hollow fibers as sustainable technologies: Past, present, and future" by Na Peng et al.⁴⁶

The two-phase region is divided by the spinodal line into three areas: the two areas between the binodal and the spinodal lines are defined as metastable areas, where the polymer solution is stable with respect to small fluctuations in the composition.⁴⁶ When those fluctuations in the composition become large, the mechanism of phase separation by **nucleation and growth** is triggered.⁴⁶ According to the polymer concentration and whether the phase separation takes place above or below the critical point, two different scenarios of nucleation and growth may take place.^{46 47}

If the phase separation takes place above the critical point, the de-mixing of the solution proceeds by the nucleation and growth of the polymer poor phase: solvent rich regions are formed and grow, resulting in the formation of liquid-filled pores in a continuous polymer matrix (Figure 28).^{47 48} When

the phase separation arrests and the solvent is removed, this mechanism produces polymeric particles or membranes with internal voids, which are not interconnected.⁴⁸

If the phase separation takes place below the critical point, the de-mixing of the solution proceeds by the nucleation and growth of the polymer rich phase: polymer nuclei are formed and grow producing a granular morphology.⁴⁷ When the phase separation stops and the solvents are removed, this mechanism produces polymeric particles with no internal porosity.⁴⁸

The area below the spinodal line is thermodynamically unstable. Phase separation occurring in this region is defined as **spinodal decomposition**.⁴⁷ It takes place when the system enters the spinodal region either directly, by crossing the critical point, or indirectly after passing the metastable region due to further quenching with the non-solvent.⁴⁸ The spinodal decomposition process is due to fluctuations in the concentration of the polymer solution: this triggers a fluctuation wave of increasing amplitude through the solution. As a result of the fluctuation wave, the phase separation gives rise to the formation of bi-continuous structures, where the polymer rich-phase and the polymer poor-phase are completely interconnected.⁴⁸ With the removal of the solvent after the process stops, the final product is a polymer network with mutually interconnected polymer domains and voids.⁴⁸

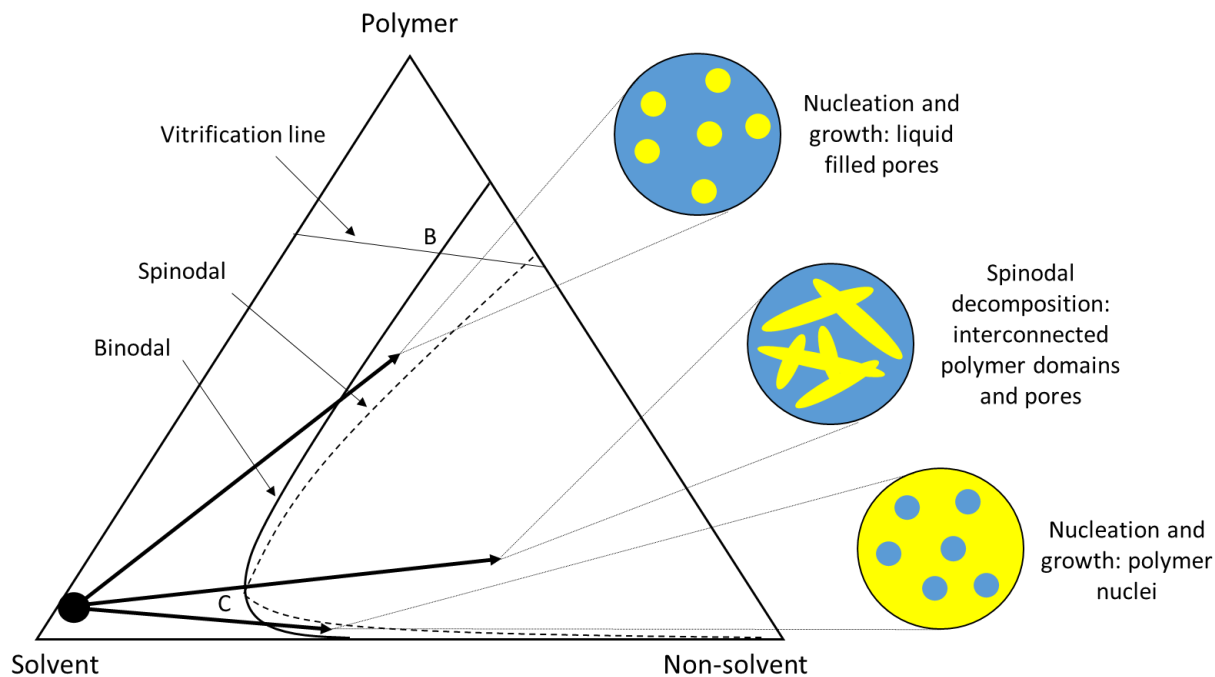


Figure 28: A generic isothermal ternary phase diagram for a polymer-solvent-non solvent system, highlighting the mechanisms of phase separation in the metastable and unstable regions. Phase separation taking place in the metastable region below the critical point C proceeds by a mechanism of nucleation and growth of the polymer-rich phase: polymer nuclei with no internal porosity are produced. Phase separation taking place in the metastable region above the critical point C proceeds by a mechanism of nucleation and growth of the polymer-poor phase: solvent rich regions are formed and grow, resulting in the formation of liquid-filled pores in a continuous polymer matrix. Phase separation occurring in the unstable region proceeds by a mechanism of spinodal decomposition: a polymer network with mutually interconnected polymer domains and solvent domains is produced. With solvent removal, the voids are filled by air. Adapted from "Composition and phase changes observed by magnetic resonance imaging during non-solvent induced coagulation of cellulose" by Laity et al.⁴⁸

The phase separation of a polymer solution, independently from the mechanisms by which may occur, arrests at the Berghman's point,⁴⁵ which is the point of interception between the binodal line and the glass transition line.⁴⁴

The Berghman's point marks the limit where the glass transition temperature of the polymer is lower than the temperature of the system:⁴⁵ at this point the polymer chains motion slows down and the polymer reverts to a glass.⁴⁴ The morphology achieved at this stage is thus fixed and observed experimentally.

The process of non-solvent induced phase separation (NIPS) of a homogeneous polymer solution has been exploited in many ways due to the numerous industrial applications of porous materials.^{49 50} Many studies have investigated the effect of several factors, such as polymer molecular weights and

concentrations, different affinities between solvent and non-solvent, on the morphology achieved. Porosity may be obtained within different structures, from large monoliths,⁵¹ to membranes⁵² and micro-particles.⁵³

Research on polycarbonate NIPS to manufacture porous monoliths highlighted the impact of different molecular weights and polymer concentrations on the final morphology achieved.⁵¹ Polycarbonate with different molecular weights were dissolved in chloroform, with cyclohexane acting as the non-solvent to induce phase separation.⁵¹

The study showed separate correlations between increasing polymer molecular weight and pore size; and concentration and pore size. The authors assigned this dependence to the viscosity of the systems, as they suggested that viscosity would affect phase separation and void size.⁵¹

The importance of the solvent for achieving a specific pore morphology has also been examined. Two NIPS systems based on poly-methyl methacrylate, with either N,N-dimethylformamide (DMF) or acetone as the solvent, with water as non-solvent, were studied.⁵⁴

The DMF system corresponded to a rapid de-mixing of the polymer solution, due to the water having high affinity for DMF. In the acetone system a delayed de-mixing occurred, due to water having a lower affinity for acetone compared to DMF.

As a result of different affinities between solvent and non-solvent, and therefore different exchange rates between them, different pore morphologies were observed: elongated pores were achieved for membranes produced with DMF, while spherical pores were observed in membranes with acetone.⁵⁴

A study aimed at producing micro-granules from polystyrene involved a combination of both TIPS and NIPS.⁵⁵ Polystyrene was dissolved in cyclohexane heated to a temperature in the range of 50-60 °C. An emulsion of this was formed by dispersing the solution in water, stabilised by a surfactant. This was then mixed with ethanol non-solvent at 0 °C. The concentration of the polystyrene in solution, affecting the viscosity of the system and the solvent-non-solvent exchange rate, was found to have a major impact on the morphology of the polystyrene structures.⁵⁵

Low concentration of polystyrene favoured the formation of polymer nuclei with low porosity. An intermediate polystyrene concentration favoured a continuous network morphology within the particles, while high polystyrene concentration produced spherical micro-granules with large internal cavities.⁵⁵

The non-solvent induced phase separation (NIPS) of a homogeneous polymer solution showed potential as a chemical process able to reproduce the type of porosity found in biological structures. In the next sections the selection of appropriate polymer, solvent, non-solvent systems and the characterisation methods of the resulting products is discussed.

CHAPTER 4: MATERIALS AND CHARACTERISATION TECHNIQUES.

In this chapter, the materials and the characterisation techniques used in the research are outlined and described. In some instances, examples of experimental data are included to show how the techniques were applied. However, the full experimental data are reported in the following chapters 4, 5 and 6, in the appropriate sub-sections.

MATERIALS.

The main objective of the experimental work was the fabrication of polymeric micro-particles with a porous internal structure. Light would be scattered at every polymer-air interface due to the difference in refractive index n between the two media. The larger Δn , the more effective would be the scattering. In order to maximise Δn between the polymer and the air ($n = 1.00$) filling the internal voids, a series of polymers with high refractive index were initially surveyed.

These included poly-pentabromophenyl methacrylate ($n = 1.71$), poly-9-vinylcarbazole ($n = 1.68$), poly-1-vinylnaphthalene ($n = 1.68$) and poly-vinyl phenyl sulphide ($n = 1.66$).

Since the secondary objective of this work was the identification of a cost-effective system, the other important factor to consider in the choice of the polymer was the cost of the materials. Sigma-Aldrich, which is one of the main suppliers of laboratory raw materials in UK for scientific research, listed the cost of these high refractive index polymers as follows: poly-pentabromophenyl methacrylate (£ 322.50 g⁻¹), poly-9-vinylcarbazole (£ 22.70 g⁻¹), poly-1-vinylnaphthalene (£ 124.00 g⁻¹) and poly-vinyl phenyl sulphide (£ 257.00 g⁻¹).

Other possible candidates were the more common α -cellulose ($n = 1.50$) and polystyrene ($n = 1.59$) with a slightly lower refractive index. The cost of these raw materials was estimated by Sigma-Aldrich as: α -cellulose (£ 0.026 g⁻¹) and polystyrene (£ 0.028 g⁻¹). Since it was known from the research on biological tissues that prominent structural colour effects could be achieved with a Δn as small as $\approx 0.1^5$ and that the refractive index of the chitin and the keratin found in beetles and birds are $\approx 1.56^{34}$ and $\approx 1.54^5$ respectively, economic reasons favoured the choice of either α -cellulose or polystyrene. Polystyrene was finally chosen as it offered a greater selection of good solvents, its hydrophobic nature and due to the extensive information about its properties available from scientific literature.

The research for an optimum system proceeded through several stages. The initial step was a proof of concept that porosity in the matrix of polystyrene particles could actually be achieved. In order to

do so, a simple ternary system with polystyrene as the polymer, tetrahydrofuran (THF) as the solvent and deionised water as the non-solvent, was chosen. Tetrahydrofuran is a good solvent for polystyrene while deionised water was the ideal non-solvent as it is miscible with THF, cheap and readily available in the laboratory.

The polystyrene used for this part of the project was already available at the Department of Chemistry, previously synthesised by a post-graduate researcher: two samples had molecular weights (M_w) of $\approx 30 \text{ kg mol}^{-1}$ and 100 kg mol^{-1} . A third sample with higher M_w of $\approx 317 \text{ kg mol}^{-1}$ was purchased from Sigma Aldrich (Gillingham, England) (Lot. Number MKBP1175V) and a fourth sample of lower M_w of $\approx 23 \text{ kg mol}^{-1}$ from Polymer Source (Montreal, Canada) (Lot. Number P9397-S).

The solvent tetrahydrofuran (THF) was purchased from Fisher Chemical (Loughborough, England) (Lot. Number 1352646) while deionised water was supplied by a Milli-Q Millipore water system. All the products were used as received.

The fabrication process required the preparation of a polymer solution of polystyrene in THF, delivered drop-wise to a bath of non-solvent deionised water.

The products obtained were characterised by scanning electron microscopy (SEM) in order to detect porosity within the particles.

Once the formation of porous internal structures within polystyrene micro-particles was established, the next step of the project revolved around the improvement of the fabrication process in order to gain a greater control of particles' shape and size, and the full characterisation of the systems in order to understand the effect of several variables, such as polystyrene molecular weight and concentration, on the morphology of the particles' internal structure. The control of particle shape was achieved through the preparation of an emulsion, where the initial polystyrene solution was dispersed as a discontinuous phase in the form of small spherical droplets, within a continuous phase of a second liquid. The emulsion was stabilised by a surfactant and delivered to a bath of non-solvent.

The continuous phase selected was deionised water, supplied by a Milli-Q Millipore water system. This required a different choice for the solvent, as in order to form an emulsion the discontinuous phase must not be miscible with water, like in the case of tetrahydrofuran. Toluene, which is a good solvent for polystyrene and not miscible with water, was selected. The non-ionic surfactant sorbitane mono-oleate (span 80) was used to stabilise the emulsion, while ethanol was identified as an ideal non-solvent, since it is miscible with both water and toluene. This is important because the non-solvent must be able to diffuse into the toluene droplets dispersed in the continuous phase of water and precipitate the polystyrene in the form of spherical micro-particles.

The polystyrene samples used for the emulsion systems had three different molecular weights: a lower M_w of 23 kg mol⁻¹, an intermediate M_w of 207 kg mol⁻¹, and a higher M_w of 317 kg mol⁻¹. The 23 kg mol⁻¹ (Lot. Number P9397-S) was purchased from Polymer Source (Montreal, Canada), while the 207 (Lot. number 02726DE) and 317 kg mol⁻¹ (Lot. number MKBP1175V) samples were purchased from Sigma Aldrich (Gillingham, England). An additional bi-modal polystyrene blend with M_w of 53 and 107 kg mol⁻¹ (Lot. Number MKBS6957V) was also purchased from Sigma Aldrich. The molecular weight of the polystyrene samples was assessed by gel permeation chromatography (GPC) analysis.⁵⁶ Toluene (Lot. Number SZBF0580V) and span 80 non-ionic surfactant (Lot. Number MKBF2220V) were purchased from Sigma Aldrich. Ethanol (Lot. Number 16B050509) was purchased from VWR Chemicals (Lutterworth, England). All the products were used as received.

The full characterisation of the systems required the measurement of the viscosity of the initial polystyrene in toluene solutions using a rheometer, the measurement of the droplets size of polystyrene solutions in the emulsions using dynamic light scattering, the construction of a ternary phase diagram defining the cloud points by using turbidimetric titration. The critical chain overlap concentration C^* for the polystyrene solutions was calculated based on literature values.

The structural morphology of the polystyrene multi-voided particles was characterised by scanning electron microscopy (SEM) and small angle X-ray scattering (SAXS). The study highlighted a correlation between the polystyrene concentration in the initial polymer solutions and the average diameter of the pores in the internal structure of the particles, for systems with polystyrene concentration smaller than C^* . Since polystyrene concentration and viscosity of the polymer solution are related, a correlation between the viscosity of the initial solutions and the average pore size was also observed. These correlations allowed the control of pore size in the final morphology of the particles by selecting the appropriate conditions (polystyrene concentration) for the initial polymers solutions.

The final part of the project consisted in the scale up of the emulsion system, in order to produce enough product to be incorporated into paint formulations provided by the industrial partner AkzoNobel® and to be tested. Due to health and safety requirements in the AkzoNobel® laboratories, the toluene solvent and the ethanol non-solvent were replaced by the less harmful xylene and isopropanol respectively. Initial testing in Sheffield employing polystyrene 23 kg mol⁻¹ (Polymer Source, Lot. Number P9397-S), xylene (Sigma Aldrich, Lot. Number SZBC1510V) and isopropanol (VWR Chemicals, Lot. Number 15L180503) demonstrated that the particles' morphology obtained was equivalent to that achieved with the previous systems based on toluene and ethanol.

The scale up process took place in the AkzoNobel® laboratories in Slough, UK. Polystyrene of M_w 25 kg mol⁻¹ (confirmed by GPC analysis) was synthesised from the monomer styrene at the AkzoNobel® pilot plant in Slough. It was delivered to the R&D laboratories in Slough in the form of polystyrene solutions in xylene with a concentration of 40% by weight. Xylene solvent and isopropanol non-solvent were also provided by the plant in Slough. Span 80 non-ionic surfactant was purchased from Sigma Aldrich, while deionised water was obtained from a Millipore water purifier. The polystyrene particles were characterised by SEM to verify the presence of a porous internal morphology.

The particles were dispersed into water-based paint formulations containing Acrysol X935-60 (thickener), titanium dioxide slurry (opacifier), Ropaque Ultra E (extender), Mirecide ON37 (antibacteria), Dispelair CF246 (anti-foam), Disponil A1580 (non-ionic surfactant), Bermocoll EBM solution (non-ionic surfactant), Dispex N40 (dispersing agent).

The paint was spread on Melinex transparent polyester substrates using a film applicator, in order to achieve films of a desired thickness. The reflectance of the paint films over black and white substrates was measured using a Datacolor spectrophotometer. The density of the films was calculated. The reflectance and density data allowed the estimation of the scattering coefficient of the paint due to the polystyrene multi-voided particles, and therefore the quantification of the scattering power of the particles.

CHARACTERISATION TECHNIQUES.

In this section, a brief outline of the analytical techniques used to characterise the polymers, the polymer solutions, the emulsions, the phase separation process and the particles' morphology, is given. For the full experimental data refer to the respective sub-sections in the chapters 4, 5 and 6.

GEL PERMEATION CHROMATOGRAPHY (GPC).

Gel permeation chromatography is a separation technique used to gain information on the molecular weight distribution of a polymer sample.⁵⁶ The process includes a stationary phase (a column tightly packed with a porous cross-linked gel in the form of beads, which act as a filter) and a mobile phase (a continuously flowing stream of solvent, called eluent).⁵⁶

The GPC apparatus consists of a pump, which delivers the mobile phase at a selected flow-rate; an injector, where the sample, in the form of a polymer solution, can be introduced into the solvent stream; a column, which separates the sample according to molecular size; and a detector, capable of quantifying the sample components.⁵⁷

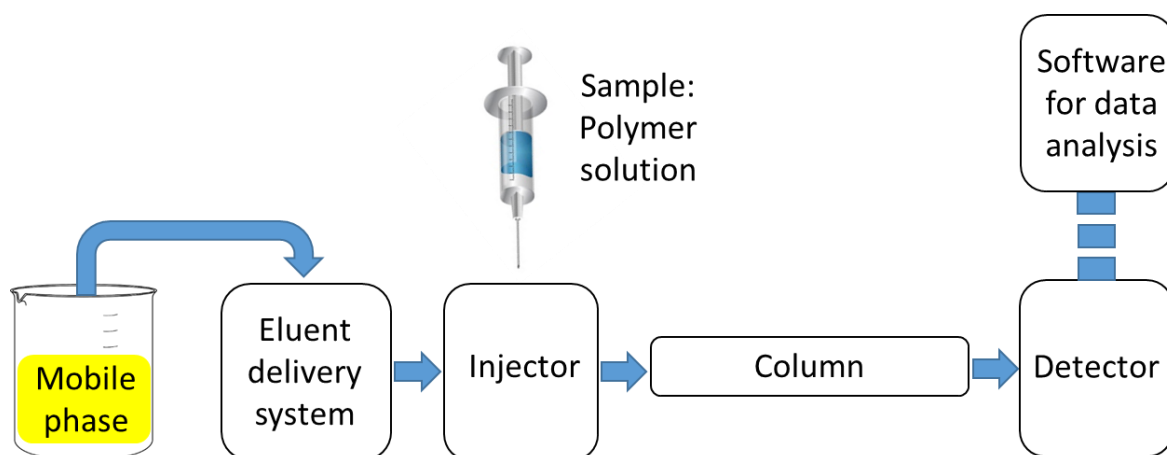


Figure 29: The basic components of a gel permeation chromatography apparatus. The solvent, constituting the mobile phase, is delivered by a pump at a selected flow-rate. An injector facilitates the introduction of the polymer sample, in the form of a polymer solution, into the solvent stream. The column separates the sample according to the molecular size of its components. The detector continuously monitors the flow, detecting and quantifying the passing polymer sample.

The sample preparation requires the dissolution of the polymer in a good solvent. The polymer solution is then injected into the mobile phase stream, and the polymer is separated by the column.⁵⁷ The separation is related to the radius of gyration of the polymer chains in the solvent, which determines the volume of the chains in solution. When crossing the column, the smaller

polymer chains transit for a longer period of time through the porous gel, since the smaller dimensions favour their trapping into the small pores (they have a longer flow-path). Longer polymer chains, with greater radii of gyration and larger volumes, only interact with large pores and can therefore easily pass through the column (they have a shorter flow-path). As a result, polymer chains of different lengths elute at different retention times.⁵⁷ A detector is used to determine the concentration of the different chain populations in the sample, providing information on the molecular weight distribution of the polymer analysed. A calibration curve, obtained by using polymer standards of known molecular weight, enables an accurate estimation of the sample molecular weight.⁵⁷

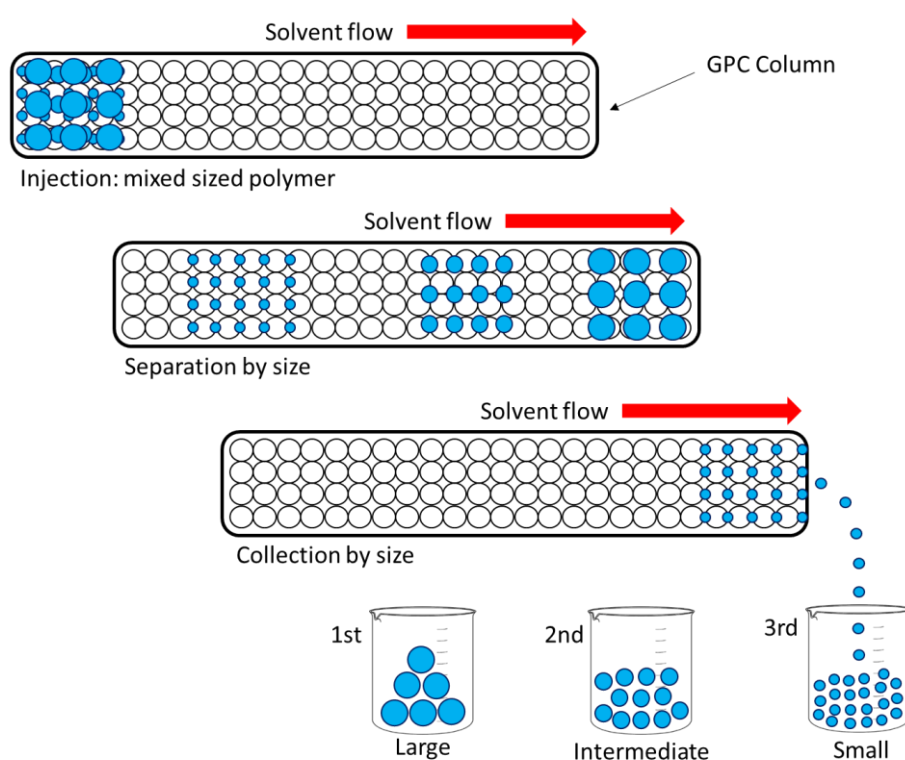


Figure 30: A schematic representation of the separation mechanism within a GPC column. The column is filled with tightly packed beads of cross-linked porous gel. When the sample is injected and reaches the column due to the action of the solvent flow, chain molecules of different lengths move across the column at different rates. Large polymer molecules have a shorter flow-path, as they only interact with large pores within the gel. They have a shorter retention time and are the first components of the sample to be detected. Smaller polymer molecules have a longer flow-path, as they interact with a large number of small pores within the gel. They have a longer retention time.

The GPC device may use different techniques in order to characterise the sample. The most common detectors for GPC are concentration sensitive (which exploit UV absorption or refractive index to

differentiate between the mobile phase and the polymer) or molecular weight sensitive (using light scattering to determine polymer chain size).⁵⁷

The data collected by the detector are processed by software and displayed in the form of a chromatogram. A chromatogram is a 2D diagram, generally in the form of retention time (minutes) on the x-axis and response (mV) on the y-axis.⁵⁷

VISCOSITY OF THE POLYMER SOLUTIONS AND C^* .

The shear viscosity of the polymer solutions used to produce the multi-voided particles was measured using a rotational stress-controlled rheometer, equipped with a cone and plate geometry, using a continuous shear mode.

Rheology can be defined as the study of flow and deformation of matter, and in particular it investigates the relationship between stress and deformation in a material.⁵⁸

If a tangential force F is applied to a material, as in Figure 31, a deformation occurs. The concepts of shear stress, shear strain and shear rate can be introduced in order to describe the system.^{58 59}

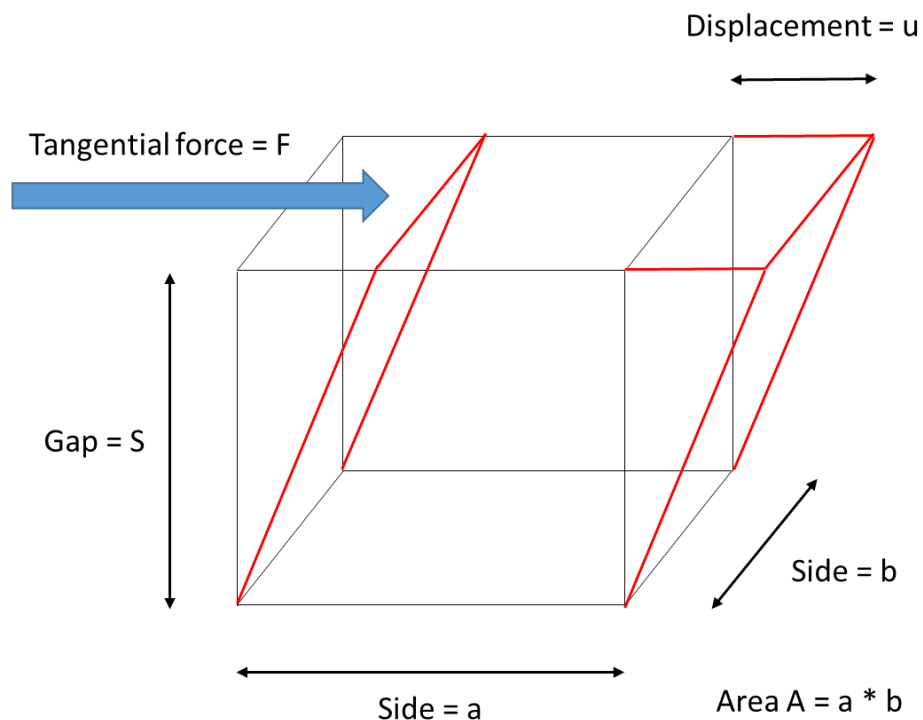


Figure 31: A cuboid section of a material undergoing deformation into a parallelepiped, due to the effect of the tangential force F applied. The size of the dimensions a , b and S are highlighted. The displacement u can be observed.

The shear strain γ is given by the relationship between the displacement u of the sample due to the action of the tangential force F and the height of the sample S , which is equivalent to the gap between the two plates of the rheometer, where the sample to be analysed is placed (Figure 32). The shear strain is a dimensionless number.⁵⁹

$$\gamma = \frac{u}{S} \quad \text{Equation 18}$$

The shear rate $\dot{\gamma}$ is given by the shear strain per interval of time, and it is expressed in reciprocal seconds (s^{-1}):⁵⁹

$$\dot{\gamma} = \frac{\gamma}{t} \quad \text{Equation 19}$$

The shear stress τ is given by the tangential force F divided by the area A of the sample where the force is applied, and it is expressed in Pascal (Pa) or Nm^{-2} .⁵⁹

$$\tau = \frac{F}{A} \quad \text{Equation 20}$$

The shear viscosity η of a sample, defined as the resistance of the material against the flow induced by the tangential force F , is calculated by dividing the shear stress τ by the shear rate $\dot{\gamma}$, and it has the units of $Pa \times s$:⁵⁹

$$\eta = \frac{\tau}{\dot{\gamma}} \quad \text{Equation 21}$$

The rheometer is the instrument used for measuring the viscosity of a material. The basic structure consists of a motor, able to promote a controlled rotation of the measuring plate (also called geometry), generating torque. The geometry is directly connected to the motor and can have different configurations (eg. flat and conical are the most common). The static plate acts as a sample holder and it is normally integrated with a temperature controller, in order to maintain a selected temperature for the measurements. The sample is placed in the gap between the static and the measuring plates.⁵⁹

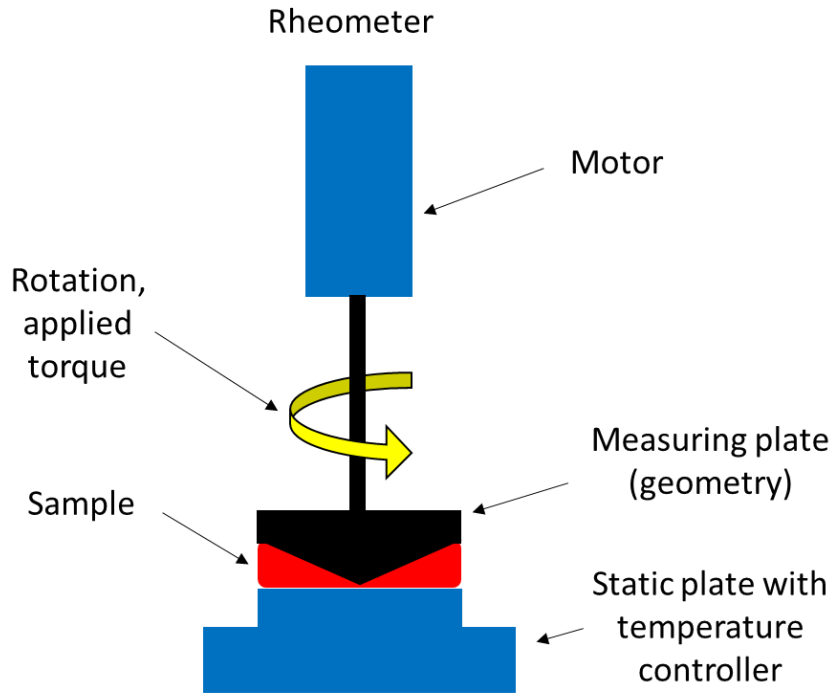


Figure 32: A sketch of the basic structure of a rheometer. The motor produces torque and promotes the rotation of the measuring plate (called geometry). The static plate has the function of a sample holder. It is usually integrated with a temperature controller to keep a constant temperature during the measurements. The sample is placed between the geometry and the static plate.

The rheometer is capable of applying or measuring torque, angular displacement and angular velocity. These parameters can be used to calculate shear stress τ , shear strain γ and shear rate $\dot{\gamma}$, ultimately obtaining the value of the shear viscosity η of the sample analysed.

The shear stress τ is calculated from the torque M , using the relationship:⁵⁹

$$\tau = M \times K_{\tau} \quad \text{Equation 22}$$

where K_{τ} is the stress constant and it is dependent on the type of geometry used (eg.: K_{τ} is equal to $2/\pi r^3$ for a flat (parallel plate) geometry or to $3/2\pi r^3$ for a conical (cone and plate) geometry, where r is the radius of the geometry).⁵⁹

The shear strain γ is calculated from the angular displacement θ (expressed in radians) using the relationship:⁵⁹

$$\gamma = \theta \times K_{\gamma} \quad \text{Equation 23}$$

where K_γ is the strain constant and it is also dependent on the type of geometry used (K_γ is r/S for parallel plate geometry with r the radius of the geometry and S the gap between the plates. K_γ is $1/\beta$ for cone and plate geometry, where β is the angle of the cone).⁵⁹

Finally, the shear rate $\dot{\gamma}$ can be obtained from the angular speed Ω (in rad s^{-1}) which is directly controlled by the motor, according to the relationship:⁵⁹

$$\dot{\gamma} = \Omega \times K_\gamma \quad \text{Equation 24}$$

The shear viscosity η of the material is therefore obtained as:⁵⁹

$$\eta = \frac{\tau}{\dot{\gamma}} = \frac{M K_\tau}{\Omega K_\gamma} \quad \text{Equation 25}$$

The rheological data for shear viscosity η are usually displayed in two-dimensional diagrams with shear rate $\dot{\gamma}$ on the x-axis and shear stress τ on the y-axis. Alternatively, they can be displayed with shear rate $\dot{\gamma}$ on the x-axis and shear viscosity η on the y-axis: in this form, zero shear viscosity η_0 can be extrapolated for shear rate $\dot{\gamma}$ approaching zero.

The viscosity of the polymer solutions was measured using a rotational continuous shear mode. The measurements showed that the viscosity η was independent of shear rate, demonstrating that the polymer solutions behaved like Newtonian fluids within the measured shear rate interval ($\dot{\gamma} < 100 \text{ s}^{-1}$). Zero shear viscosity η_0 was then extrapolated for shear rate $\dot{\gamma}$ approaching zero. An alternative method for obtaining the viscosity of the polymer solutions relies on the use of an oscillatory mode, which is designed to measure the storage modulus G' (a measure of the material's ability to store elastic energy) and the loss modulus G'' (a measure of the material's ability to dissipate energy).⁶⁰ G' and G'' can be used to calculate the complex viscosity $|\eta^*|$:⁶⁰

$$|\eta^*| = \sqrt{(\eta')^2 + (\eta'')^2} \quad \text{Equation 26}$$

where:

$$\eta' = \frac{G''}{\omega} \quad \text{Equation 27}$$

$$\eta'' = \frac{G'}{\omega}$$

Equation 28

with ω being the angular frequency.

For a Newtonian fluid G' is equal to zero. Since it would be difficult for a rheometer to measure a zero value for G' due to the uncertainty caused by the limits of equipment sensitivity, it would be better to rely only on G'' to measure the dynamic viscosity η' , defined as the resistance of a liquid to shearing flow. The dynamic viscosity can therefore be also extracted from oscillatory measurements. However, in industry a rotational continuous flow is usually preferred and this is the reason why a rotational stress-controlled rheometer using a continuous shear mode was employed.

The viscosity of the polymer solutions is strictly linked to the concentration of polymer. It was found that this concentration affects the phase separation and it plays an important role in determining the morphological features of the final products.

When a polymer is dissolved in a good solvent, the polymer chains achieve geometrical configurations which can be mathematically described as a random-walk. The radius of gyration is a parameter used to estimate the volume of space occupied by the polymer chains in a solvent and it is defined as the root mean square distance of the chain from its centre of mass.⁶¹

In dilute solutions, the polymer chains are separated from each other by large regions of solvent. However, as the polymer solutions become progressively more concentrated, the polymer chains are found closer to each other until, at a certain concentration defined as the critical chain overlap concentration C^* , the polymer chains are in direct contact and the phenomenon of chain interaction occurs.⁶¹ The kinetic of phase separation of a polymer solution and the morphology of the precipitated polymer are affected by whether the polymer solution concentration, C , is higher or lower than C^* . The ratio C/C^* defines the degree of polymer chain overlapping.⁶¹

The radius of gyration of a polymer in solution can be experimentally determined by light, neutron or X-ray scattering experiments.⁶²

It can also be theoretically calculated from the relationship between the Kuhn length and the contour length of a polymer chain.⁶³

The Kuhn length can be defined as the distance along the polymer that corresponds to a stiff (unbent) segment in a freely jointed chain model. The Kuhn length is not necessarily equal to the monomer length and it is usually longer. The contour length is the end-to-end distance of a polymer chain completely stretched out.^{63 64}

The radius of gyration is given by:

$$R_g^2 = \frac{1}{6} L \times b \quad \text{Equation 29}$$

where R_g^2 is the mean squared radius of gyration of the polymer, b is the Kuhn length and L is the contour length.⁶³ The contour length L can be calculated from:

$$L = 2 \times l \times \cos\left(\frac{\theta}{2}\right) \times N \quad \text{Equation 30}$$

where l is the carbon-carbon bond length of the polymer skeleton, θ is the tetrahedron angle and N is the number of repeat units in the polymer chain, calculated as molecular weight M_w of the polymer divided by the molecular weight M_u of the monomer.⁶³

The value of the radius of gyration, obtained either from scattering experiments or by theoretical models, can be used to calculate the critical chain overlap concentration C^* :⁶¹

$$C^* = \frac{3M_w}{4\pi(R_g^2)^{3/2}N_A} \quad \text{Equation 31}$$

where M_w is the molecular weight of the polymer, R_g^2 is the mean squared radius of gyration and N_A is the Avogadro's number.⁶¹

CLOUD POINT DETERMINATION.

The phase separation behaviour of polymer-solvent-non solvent ternary systems can be mapped by turbidimetric titration.⁶⁵ The technique allows the identification of the binodal boundary, separating the one-phase region (where the system is a homogeneous mixture) from the two-phase region (where the system undergoes a de-mixing into a solid-liquid mixture, with polymer precipitation) on a ternary phase diagram.⁴⁴ The binodal marks the starting point of the phase separation, which then proceeds by nucleation and growth or by spinodal decomposition according to whether the system transits into a metastable or an unstable region.^{44 46}

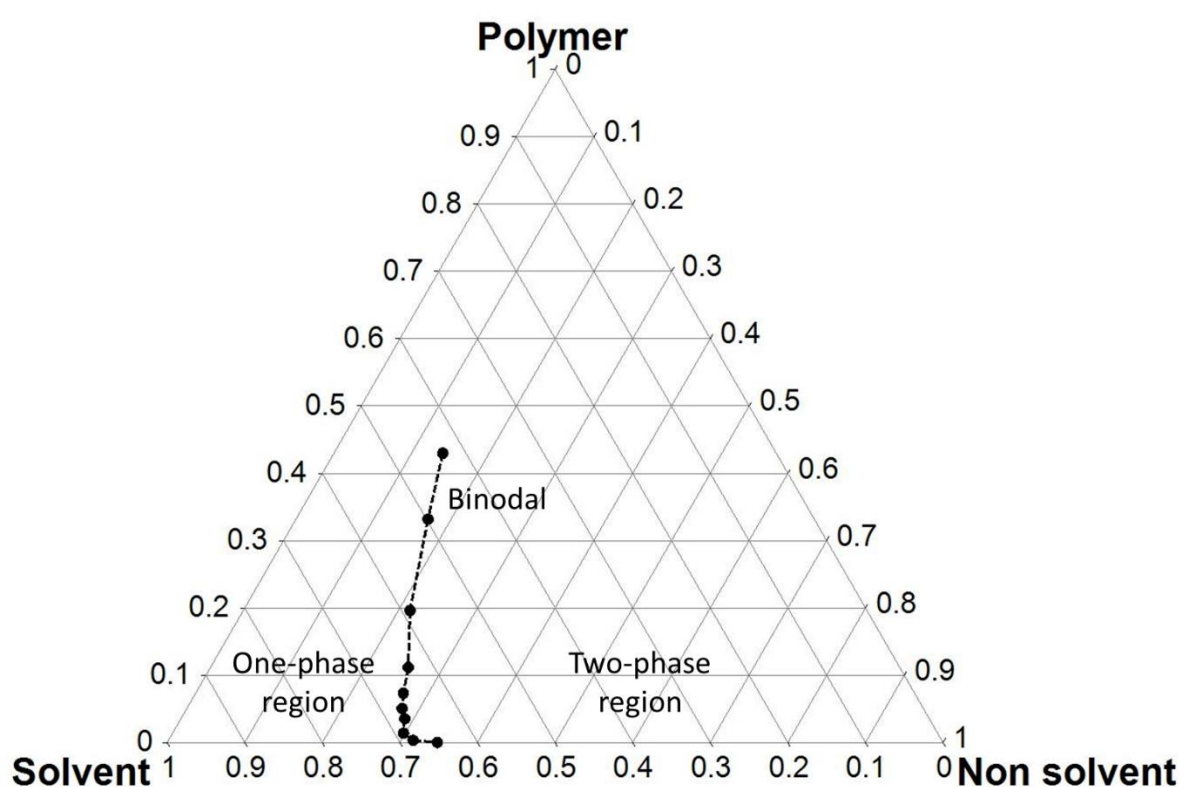


Figure 33: A ternary phase diagram for a polymer-solvent-non solvent ternary system. The example of binodal reported was obtained by turbidimetric titration performed on polystyrene (bi-modal sample with M_w of 53 and 107 kg mol⁻¹) solutions in toluene at PS concentrations from 0.05 to 50% by weight. The filled circles represent the cloud points measured. The dotted line connecting the cloud points represent the binodal boundary.

Turbidimetric titration, also called cloud points measurement, is carried out by delivering non-solvent to stirring polymer solutions, having different concentrations.⁶⁵ The delivery of non-solvent is terminated when the polymer solution suddenly transitions from clear to cloudy, due to the precipitation of the polymer.⁶⁵ The volume of non-solvent delivered is recorded. The amounts of polymer, solvent and non-solvent for each measurement can then be converted into percentages

and can be used to build a ternary phase diagram as in Figure 33. The cloud points can be connected to highlight the binodal boundary.

Turbidimetric titration was performed by delivering ethanol non-solvent drop-wise from a burette to stirring solutions of polystyrene in toluene. Nine measurements were performed, with polystyrene solutions at the concentrations of 0.05, 0.5, 2.0, 7.0, 10.0, 15.0, 25.0, 40.0% by weight. Above 40.0 % w/w the solutions were too viscous for the measurements to be performed correctly (the only exception is represented by the bi-modal sample where a tenth measurement was performed with a PS solution of 50% wt concentration). The amounts of polystyrene, toluene and ethanol were converted into weight percentages and used to build a ternary phase diagram for the system, to map the exact locations and conditions at the beginning of the phase separation. The relative amounts of solvent and non-solvent at the start of the phase separation were used to explain the morphological differences observed in the polystyrene multi-voided particles.

DYNAMIC LIGHT SCATTERING (DLS).

Dynamic light scattering was used to estimate the average droplet size of the polystyrene-toluene solutions, dispersed, as the discontinuous phase, in the emulsions used to fabricate the multi-voided particles.

The DLS set up consists of a monochromatic light source (a laser), a sample chamber (a cuvette holder) and a photomultiplier detector at a set angle.⁶⁶ The laser light is scattered by the particles in solution (or the droplets in the case of an emulsion), giving rise to a speckle pattern, and collected by the photomultiplier detector.⁶⁶

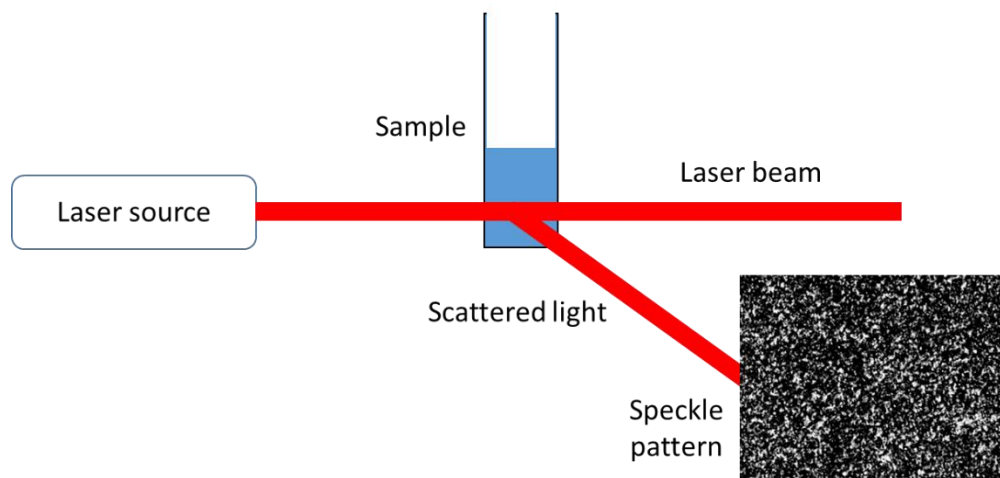


Figure 34: A sketch of a DLS set up. A monochromatic light source directs a beam to the sample: the scattered light is collected in the form of a speckle pattern by a photomultiplier detector positioned at a specific angle.

When the particles in solution are hit by the laser light, they scatter light in all directions. The scattered light from different particles interacts, giving rise to constructive or destructive interference. Constructive interference would produce a white spot on the detector's screen, while destructive interference would produce a dark spot: this image of white and dark spots is defined as a speckle pattern.⁶⁷

Since the particles in the sample are constantly moving due to the Brownian motion, also the speckle pattern is continuously changing. Thus, the intensity of the scattered signal recorded by the photomultiplier at a set angle will be fluctuating with time. The rate of change of the intensity is related to the size of the particles: the greater the size, the slower their motion, the slower is the rate of change of the pattern.⁶⁷ The analysis of the evolution of the intensity (or a speckle 2D pattern) with time, performed by an auto-correlator and described by a correlation function, allows the estimation of the decay rate Γ of the autocorrelation function as a function of delay time:⁶⁷

$$\Gamma = q^2 D_t \quad \text{Equation 32}$$

where D_t is the translational diffusion coefficient and $q = \left(\frac{4\pi n_0}{\lambda}\right) \sin \theta$ with n_0 being the refractive index of the sample, λ is the irradiating laser wavelength, and 2θ is the angle at which the detector (a photomultiplier) is located with respect to the sample.⁶⁷

The translational diffusion coefficient D_t can then be used to obtain the diameter d of the particles, according to the Stokes-Einstein equation:⁶⁷

$$d = \frac{k T}{3 \pi \eta D_t} \quad \text{Equation 33}$$

where k is the Boltzmann's constant, T is the temperature, and η is the viscosity of the sample.⁶⁷

SCANNING ELECTRON MICROSCOPY (SEM) AND IMAGE-J ANALYSIS OF SEM.

Structural information regarding the morphology of the polystyrene multi-voided particles was obtained by imaging the cross-sections of fractured particles using scanning electron microscopy (SEM). The SEM images of multi-voided polymeric particles were processed using the Image J^{68 69} software in order to estimate the pore size distribution within the samples.

The first step of the image processing required a software calibration: the scale bar on the SEM images was used as a guide to set the correct pixel/distance ratio. The function “bandpass filter” was used to sharpen the edges of the porous regions and the function “threshold” was used to select, by chromatic contrast, only the areas of interest (the pores).

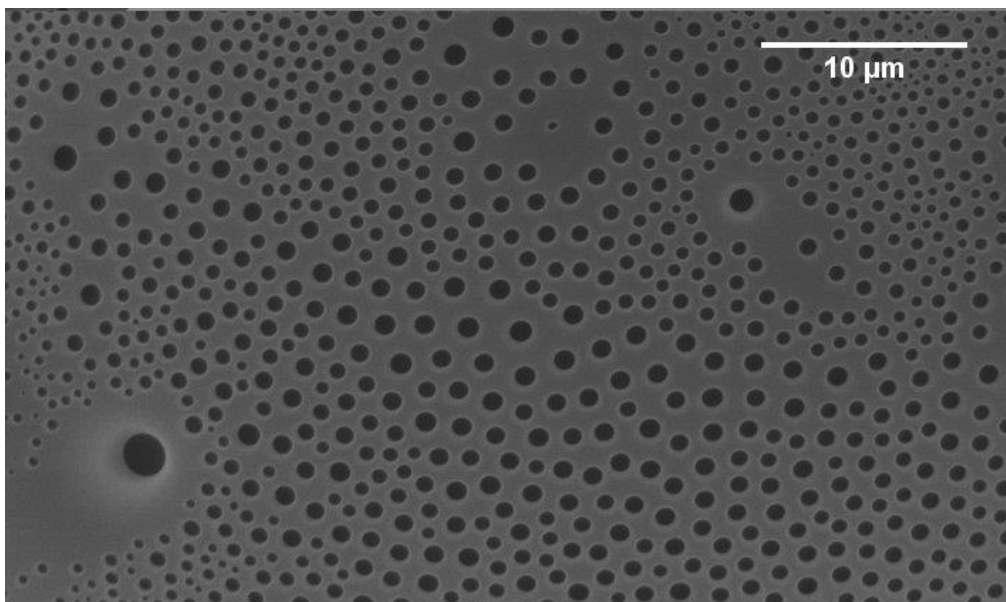


Figure 35: The original SEM image of a porous region within a polystyrene multi-voided particle. The scale bar (10 µm) was used for calibration, in order to set the correct pixel/distance ratio.

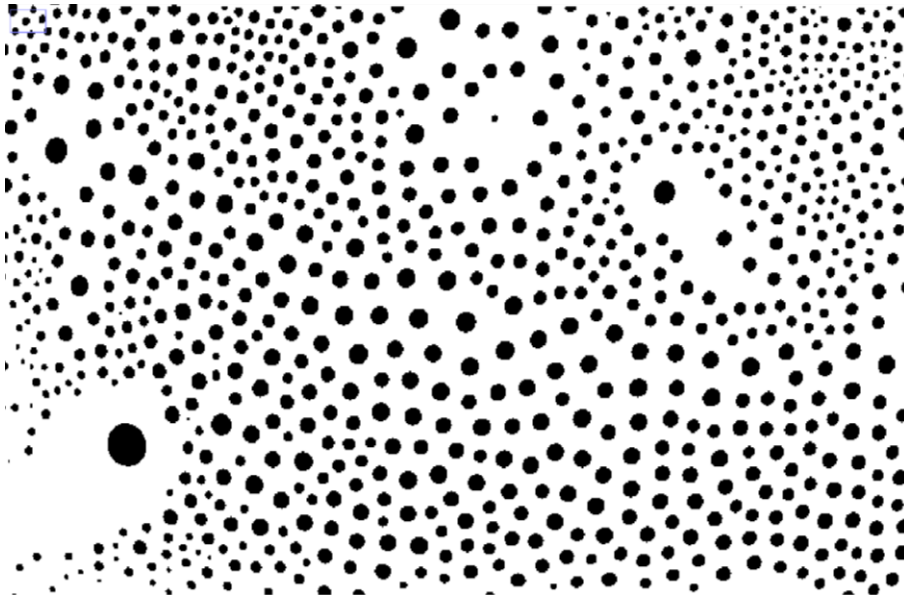


Figure 36: The processed image of the original in Figure 35, after applying the “bandpass” and the “threshold” functions. Only the regions of interest (the pores) are selected.

The high contrast image (Figure 37) obtained for the porous structure using the “analyse” function was used to identify the boundaries of the pores. The software calculated the value of the area within every circle-like object on the basis of the initial pixel/distance calibration. The area was expressed in nm^2 . A list of pores with their corresponding areas was produced by the software, enabling the calculation of pore diameters. The histogram analysis tool in Microsoft Excel was used to display this information in a graphical form, presenting the pore diameter in nm on the x-axis and the number of pores (frequency) on the y-axis.

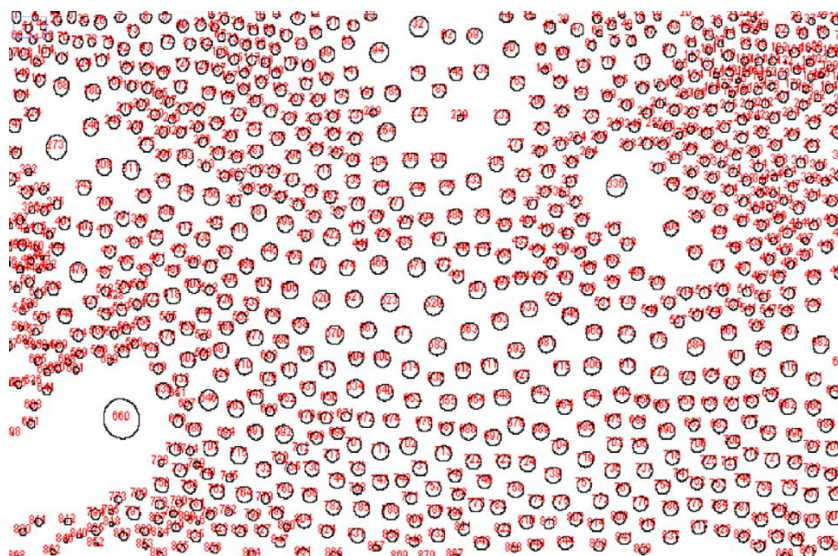


Figure 37: The “analyse” function highlighted the outline of the porous regions, providing a value of the area for each circle-like object. The areas can be used to calculate the diameters, making the assumption that the pores are perfect circles.

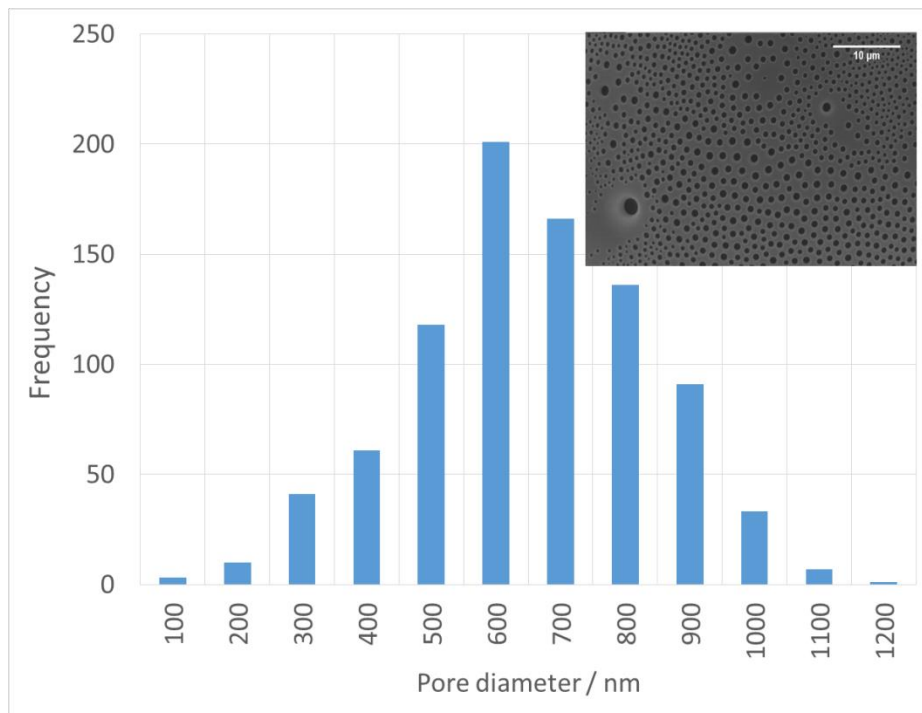


Figure 38: A histogram of the number of pores versus their diameter, showing the pore size distribution obtained from the SEM image after the Image J processing.

This process enabled the quantification of the graphical information obtained by SEM imaging and made possible the estimation of the pore size distributions within the polymer samples.

SMALL ANGLE X-RAY SCATTERING (SAXS).

SAXS was used in order to determine the average pore size of the polystyrene multi-voided particles. This technique is complementary to the SEM: both provide structural information on the samples. However, while SEM is limited in the fact that only a few particles can be imaged and analysed, SAXS collects information from a relatively large sample volume (about 1 mm^3) and is able to provide information on millions of micron-sized particles. It is therefore more representative and accurate.⁷⁰ The basic components of a SAXS instrument consist of a X-ray source of monochromatic radiation (this can be a sealed X-ray tube for lab-devices coupled with a monochromator, or a synchrotron), a collimation system to control divergence and size of the X-ray beam, a sample holder, a beam-stop to exclude the intense direct beam from scattering patterns, and a X-ray detector (usually a 2D detector) to record the scattered radiation.^{70 71}

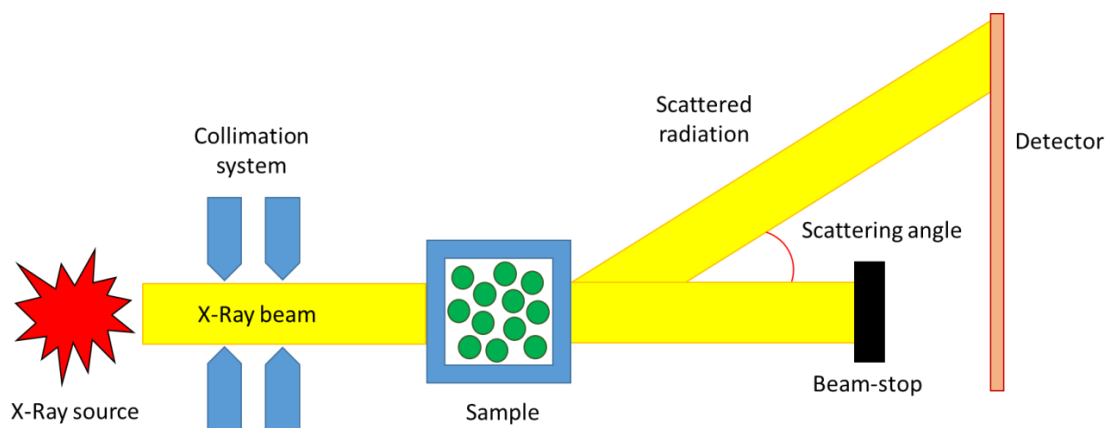


Figure 39: A basic set up for a SAXS instrument. A X-ray source produces an incident X-ray beam focused by a collimation system in order to interact with a sample. The scattering takes place due to the interaction of the X-ray with the sample and it is recorded in the form of a bi-dimensional pattern by the detector. The beam-stop is used to exclude the primary X-ray beam from scattering pattern and also to prevent the intense primary beam from hitting and damaging the detector.

A SAXS instrument is generally capable of resolving structural features in the size-range of 1 to 100 nm. However, if needed, this range can be extended below 1 nm down to a fraction of angstrom (wide-angle X-ray scattering, WAXS) or above 100 nm up to $10 \mu\text{m}$ (ultra small-angle X-ray scattering, USAXS).⁷⁰ When the X-ray beam interacts with the particles in the sample, the electrons oscillate with the same frequency of the incident radiation. As a result of this oscillation, the electrons start radiating at the same frequency (elastic scattering). The radiation emissions from neighbouring atoms comprising an object in the sample give rise to interference, producing coherent scattering: the interference patterns formed, which carry information on the structural features of the object and the sample in general, are recorded by the detector.^{70 71}

The interference pattern is characteristic of the internal structure of the sample and it is registered in the form of a two-dimensional pattern on the detector plane. The intensity of the scattering varies with the scattering angle. The scattering patterns are presented as functions of \vec{q} , defined as the length of the scattering vector, and given by the difference between the incident radiation vector \vec{K}_0 and the scattered radiation vector \vec{K} , as shown in Figure 40.⁷¹

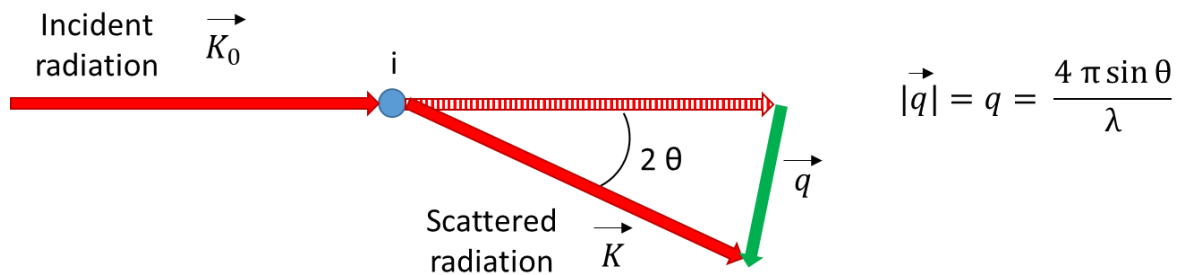


Figure 40: The length of the scattering vector \vec{q} , given by the difference between the incident radiation vector \vec{K}_0 and the scattered vector \vec{K} , due to the interaction with the atom i . The modulus of the vector $|\vec{q}|$, indicated as q , is equivalent to $4\pi \sin \theta / \lambda$ and it is expressed in \AA^{-1} or nm^{-1} .

\vec{q} represents a distance on the bi-dimensional (2D) pattern on the detector plane. The modulus of the vector $|\vec{q}|$, indicated as q , is given by:⁷¹

$$q = \frac{4\pi \sin \theta}{\lambda} \quad \text{Equation 34}$$

where θ is half of the scattering angle and λ is the wavelength of the applied radiation. q is expressed in \AA^{-1} or nm^{-1} : for this reason a scattering pattern is also defined as a structure represented in reciprocal space.⁷⁰

The polystyrene multi-voided particles were characterized using the following approach. Scattered intensity of nanoscale structural objects at large q should follow a power law dependence:⁷²

$$I(q) \propto q^{-P} \quad \text{Equation 35}$$

where P is the power-law exponent. In the particular case, when $P = 4$, Equation 35 corresponds to Porod's law, describing scattering from a two-phase system with sharp interfaces. It is expected that the studied polystyrene multi-voided particles in air correspond to a typical two-phase polymer-air

system having sharp distinct interfaces. Indeed, it was found that SAXS patterns of these particles obey Porod's law at large q . A complete expression for Porod's law is:^{72 71}

$$I_v(q) = \frac{I(q)}{V} \propto \frac{2 \pi (\Delta SLD)^2 S_v}{q^4} = \frac{B}{V} q^{-4} = B_v q^{-4} \quad \text{Equation 36}$$

where I is the relative scattered intensity, I_v is the absolute scattered intensity per unit sample volume, V is the sample volume irradiated by X-rays, ΔSLD is the contrast corresponding to a difference between scattering length densities of the two phases, S_v is the total surface area per unit sample volume and B_v is Porod's constant per unit volume of the material. Another parameter to be considered in SAXS analysis of the system is the scattering invariant. When expressed on an absolute scale the invariant is defined as the total scattering power of the sample per unit volume, calculated by integrating the absolute scattered intensity over the entire reciprocal space:^{72 71}

$$Q_v = \frac{Q}{V} = \int q^2 I_v(q) dq = 2 \pi^2 (\Delta SLD)^2 \varphi_P (1 - \varphi_P) \quad \text{Equation 37}$$

with φ_P being the volume fraction occupied by the air in the polystyrene-air two-phase system. A relative Porod's constant B (Equation 36) and the relative invariant Q (Equation 37) can be used to calculate S_v .^{71 72}

$$S_v = \frac{\pi B \varphi_P (1 - \varphi_P)}{Q} \quad \text{Equation 38}$$

It should be noted that absolute intensity calibration of scattering patterns is not required for this calculation as only the ratio B/Q , excluding irradiated sample volume and the scattering length density contrast of the material, is used in Equation 38.

The air volume fraction (dominated by the pore volume fraction of the voided polystyrene particles) can be estimated knowing the density of polystyrene ρ_s , the density of air ρ_p and the packing density of the particles in the sample volume ρ_{sam} , measured as mass of the sample divided by the volume occupied:⁷²

$$\varphi_P = \frac{\rho_s - \rho_{sam}}{\rho_s - \rho_p} \quad \text{Equation 39}$$

The volume fraction occupied by polystyrene is the remaining volume:⁷²

$$\varphi_s = 1 - \varphi_p \quad \text{Equation 40}$$

Using the values for the surface area S_v and the pore and structural volume fractions φ_p and φ_s of the samples, it is possible to determine the pore chord l_p defined as the average length of the void domains:⁷²

$$l_p = \frac{4 \varphi_p}{S_v} \quad \text{Equation 41}$$

The B/Q ratio required for S_v and chord length calculations were obtained from SAXS patterns using a one-level model of the unified approach⁷³ implemented in Irena SAXS macros for Igor Pro software.⁷⁴

The unified approach is based on merging Guinier and Porod approximations together as one function for fitting a basic scattering pattern combined of Guinier and Porod regions without any particular features corresponding to a particle shape, size and particle internal morphology. The Guinier region (associated with small q values) provides information about the radius of gyration of scattering objects (particles) and the Porod region (associated with big q values) contains information about the surface area of interfaces between two phases comprising the analysed system (for example, homogeneous particles dispersed in a homogenous solution). If the scattering objects are large and have a broad distribution of sizes the Guinier region might not be resolved in SAXS patterns and as a result only Porod region could be approached by SAXS measurements. Thus, the scattering pattern observed in this case would correspond to a Porod approximation represented by a power law (Equation 36) and the unified fit approach would provide the Porod's constant proportional to the interface surface area (Equation 38).

In Figure 41 a representative example of scattering pattern (polystyrene particles in air synthesised from bi-modal polystyrene, with 2% w/w polymer concentration in the initial solution) is shown, along with a model fit obtained from the unified approach.⁷³ This was used to calculate the B/Q value required for the measurements of the polystyrene-air interface surface area and, subsequently, the estimation of the average pore size.

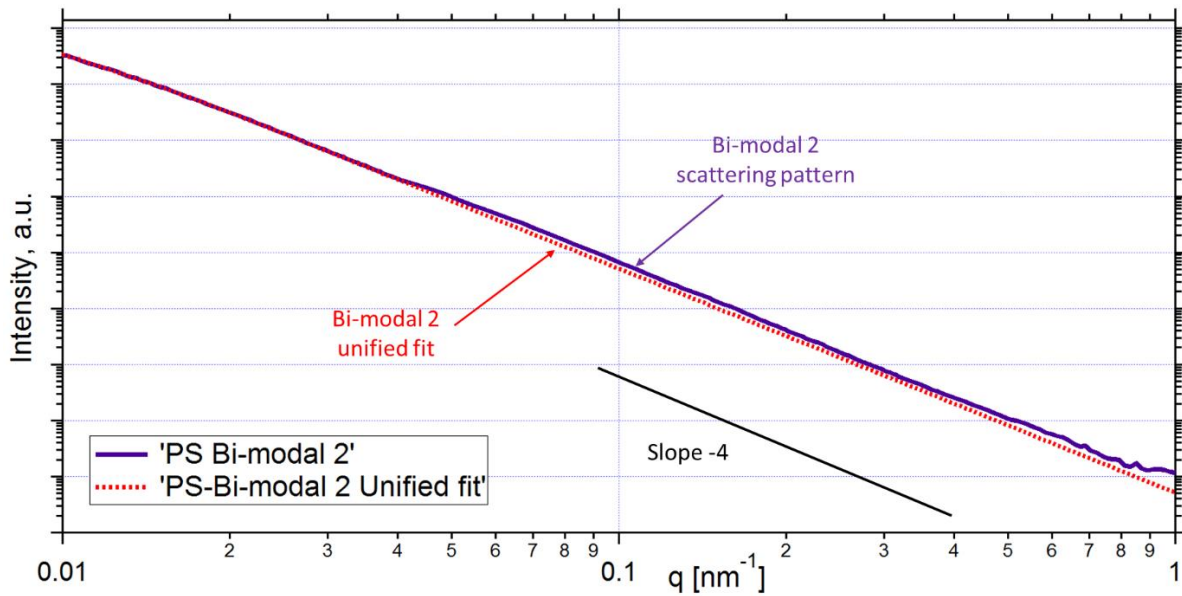


Figure 41: A representative SAXS pattern of polystyrene particles powder in air (bi-modal polystyrene, with 2% w/w polymer concentration in the initial solution) displayed in a double logarithmic format. The pattern was fitted (dotted line) using a one-level model of the unified approach implemented in Irena SAXS macros for Igor Pro software. It was assumed for the model that, at high q , $I(q) \propto q^{-4}$. The slope -4 is given for guidance.

The values of the average pore size obtained by SAXS were implemented in the pore size distribution diagrams produced by Image J,⁶⁸ analysing the SEM images of the polystyrene multi-voided particles. The agreement between the SEM and SAXS results demonstrates the complementarity of the two characterisation techniques.

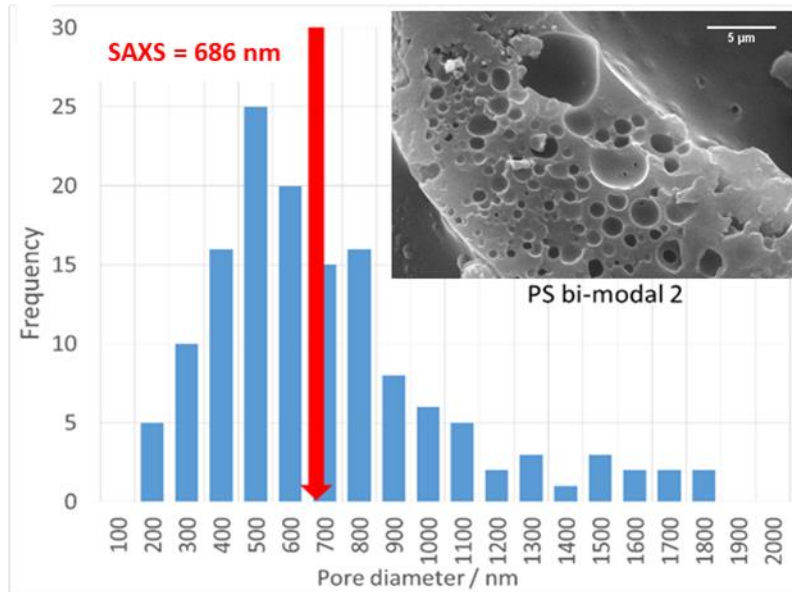


Figure 42: A representative diagram showing the pore size distribution for a bi-modal polystyrene multi-voided particle produced with 2% w/w polymer concentration in the initial solution, obtained from the SEM image after the Image J processing. The diagram was implemented with the average pore size obtained by SAXS analysis, represented as a vertical arrow within the distribution. This shows the agreement between the SEM and SAXS results and the complementarity of the two characterisation techniques.

CHAPTER 5: MULTI-VIDED POLYSTYRENE PARTICLES BY A PROCESS OF NON-SOLVENT INDUCED PHASE SEPARATION OF A POLYSTYRENE SOLUTION.

NIPS BY SOLUTION - FABRICATION PROCESS

The aim of the synthetic work was the fabrication of polymeric porous particles with:

1. A spherical shape in order for the particles to pack effectively within a paint film;
2. An ideal particles' size range of $\approx 10 - 50 \mu\text{m}$ so that the particles would fit in multiple layers within a paint film (with thickness up to $300 \mu\text{m}$);
3. A closed external surface to prevent water from the water-based paint to fill the voids in the particles, and thus reducing the scattering power of the material in wet conditions;
4. An internal porous structure, with poly-disperse pore size in the range of 200 to 700 nm, mimicking the foam structure of bird feathers, able to effectively scatter light in the visible range, producing white.

The first approach to the fabrication of porous particles by the non-solvent induced phase separation method was attempted by exploring the simplest version of a ternary system, comprising only the three essential ingredients: a polymer, a solvent and a non-solvent. The first system investigated included polystyrene with M_w of 30 kg mol^{-1} , tetrahydrofuran (THF) as the solvent and deionised water as the non-solvent.

Polystyrene was dissolved in THF at room temperature in a glass beaker by magnetic stirring, to produce a polymer solution with 10% wt of polystyrene. The polymer solution was delivered drop-wise via a 10 ml syringe (with a needle gauge of $\approx 0.7 \text{ mm}$ inner diameter), connected to a syringe pump, to four stirring coagulation baths with non-solvent to solvent ratios by volume of 1 : 1 water/THF, 1 : 0.3 water/THF, 1 : 0.1 water/THF and water only. The pump flow rate was set to 20 ml hr^{-1} . The ratio of polystyrene solution to coagulation bath was kept at 1 : 10 by volume.

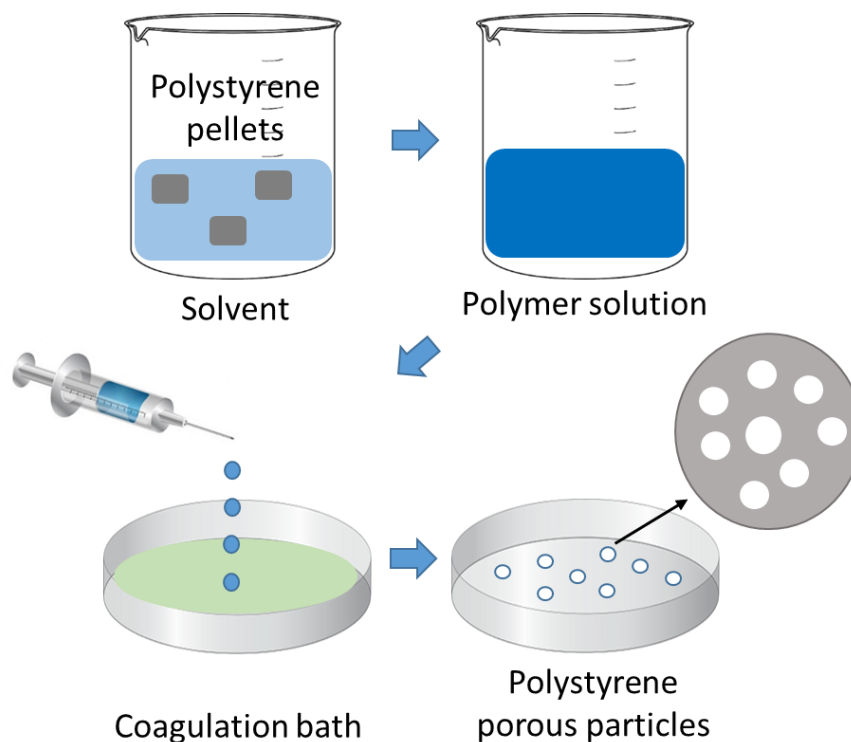


Figure 43: The process of NIPS by polystyrene solution. Polystyrene in the form of pellets was dissolved in THF solvent in order to form a polystyrene solution. The solution was delivered by means of a syringe (with a needle gauge of ≈ 0.7 mm inner diameter) connected to a syringe pump at a steady rate to a stirring coagulation bath. The particles were isolated from the mixture by vacuum filtration and left to dry to remove the residual liquids.

The products obtained were isolated by vacuum filtration and left to dry in a fume cupboard in order to remove the liquids. The systems with coagulation baths of 1 : 0.3 water/THF, 1 : 0.1 water/THF and only water were successful in producing white particles.

The system with coagulation bath of 1 : 1 water/THF produced an amorphous and colourless agglomerate, due to the high levels of THF solvent present in the coagulation bath that re-dissolved the polymer.

This trial was a proof of principle which confirmed that using a simple ternary system of polymer, solvent and non-solvent, and keeping the coagulation bath ratio of non-solvent to solvent high, white polymeric particles could indeed be achieved.

In order to investigate the effects of polystyrene molecular weight on the macroscopic morphology of the particles, the same experiment was performed with polystyrene of higher molecular weight (M_w 100 kg mol⁻¹ and 317 kg mol⁻¹) and keeping the polymer concentration at 10% wt. However, the products obtained by using high molecular weight polystyrene were in the form of long fibres, rather than the powder-like particles previously produced. This was due to the phenomenon of polymer

chains entanglement described in the characterisation section, taking place when the polymer solution concentration is higher than the critical chain overlap concentration, indicated as C^* , and defined as the critical concentration at which polymer coils begin to overlap.⁶¹ It was demonstrated that, employing this simple process, it was impossible to produce particles with high molecular weight polymer, at this level of polymer concentration.

Thus, a first evident limitation of employing the process of NIPS by solution regards the use of either low molecular weight polymer or very dilute polymer solutions in order to achieve particles.

CHARACTERISATION OF MULTI-VOIDED POLYSTYRENE PARTICLES BY SEM.

The particles successfully produced with low molecular weight polystyrene of M_w 30 kg mol⁻¹ were characterised by scanning electron microscopy (SEM). The images showed different morphologies for particles achieved with different coagulation bath compositions. For the 1 : 0.3 water/THF bath, the particles presented rounded irregular shapes. Reducing the level of solvent in the coagulation bath to 1 : 0.1 water/THF or eliminating THF altogether from the bath, produced particles with progressively flatter shapes. This trend can clearly be observed by comparing the Figure 44, 45 and 46.

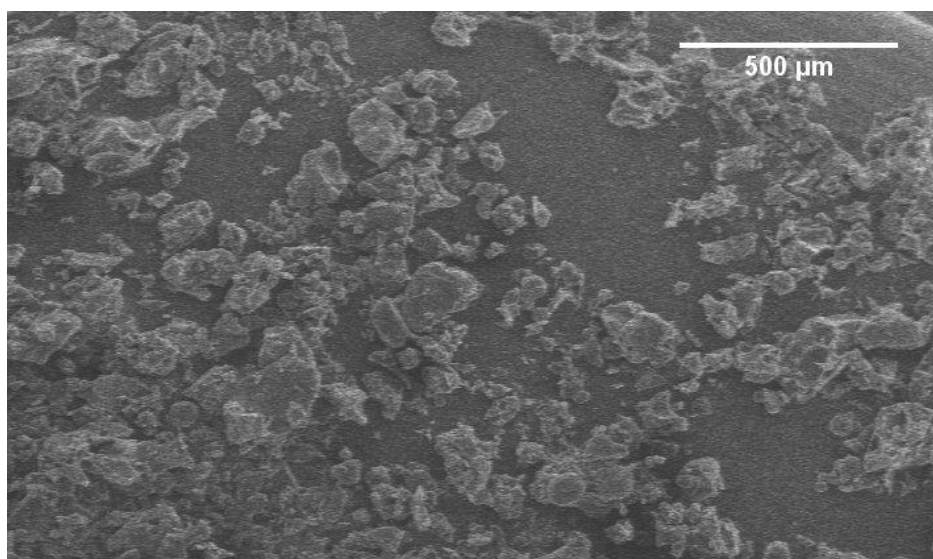


Figure 44: A representative SEM image of the polystyrene particles produced with a polystyrene in THF solution with PS M_w of 30 kg mol⁻¹ and a coagulation bath composed of 1 : 0.3 water/THF. The particles present rounded irregular shapes and broad size range.

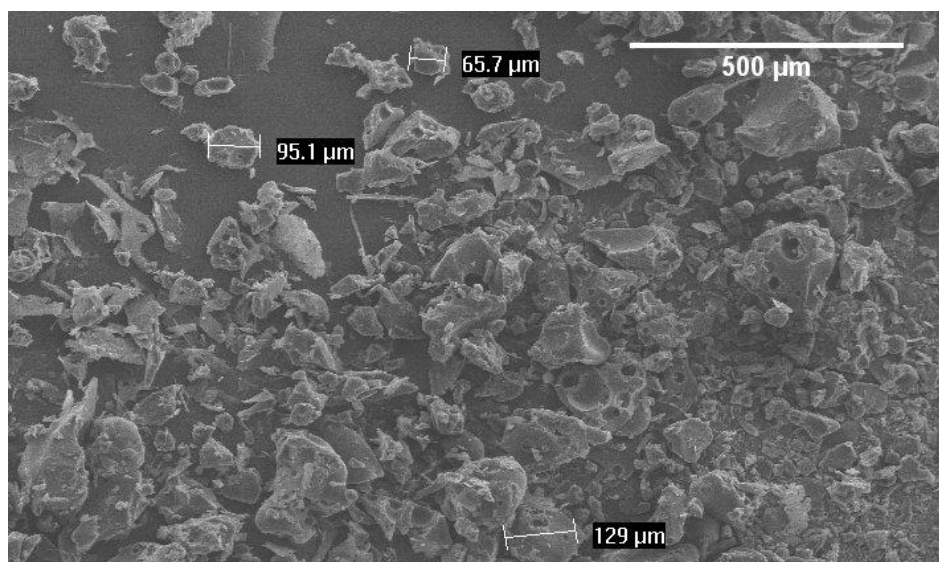


Figure 45: A representative SEM image of the polystyrene particles produced with a polystyrene in THF solution with PS M_w of 30 kg mol^{-1} and a coagulation bath composed of 1 : 0.1 water/THF. The particles present irregular shapes with some flakes. Size range is still very broad.

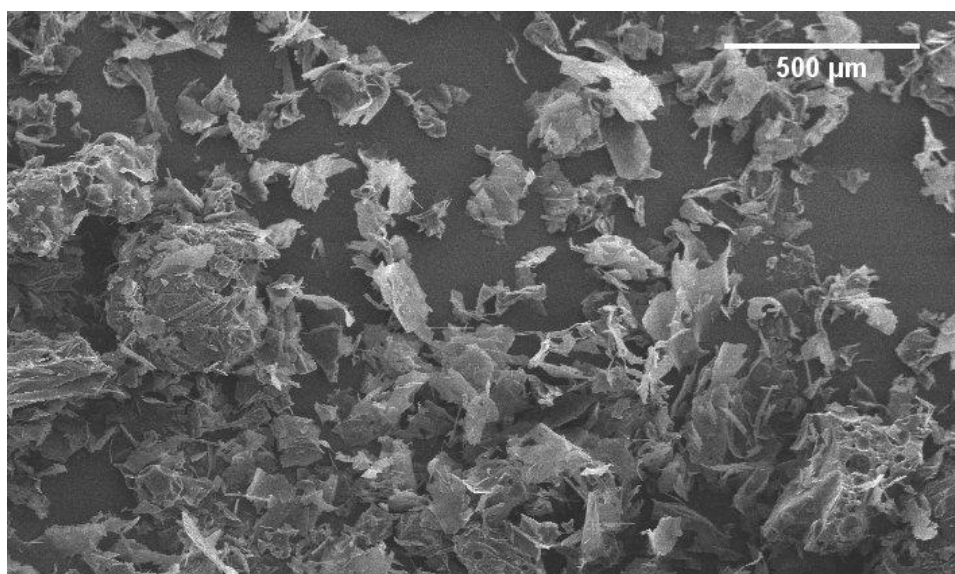


Figure 46: A representative SEM image of the polystyrene particles produced with a polystyrene in THF solution with PS M_w of 30 kg mol^{-1} and a coagulation bath composed of only water. The particles are flat and could be defined as flakes. Size range is very broad with some particles above 300 μm .

The particles size for all the bath compositions was broad, ranging from ≈ 10 to 300 μm . Internal porosity was observed in all the systems, with pore density increasing for systems with progressively less THF solvent in the coagulation bath. Details of the internal structures can be observed in the Figure 47, 48 and 49.

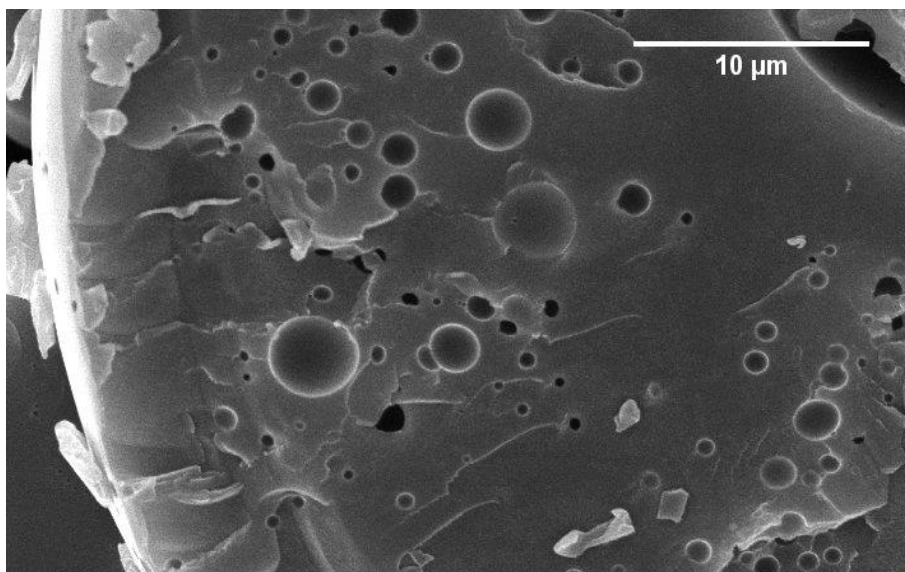


Figure 47: SEM of a cross section of a polystyrene particle produced with a polystyrene in THF solution with PS M_w of 30 kg mol^{-1} and a coagulation bath composed of 1 : 0.3 water/THF. Porosity is present within the internal structure, with spherical disconnected pores suggesting a phase separation by nucleation and growth. Pores are variable in size with a few in the desired range of 200 – 700 nm.

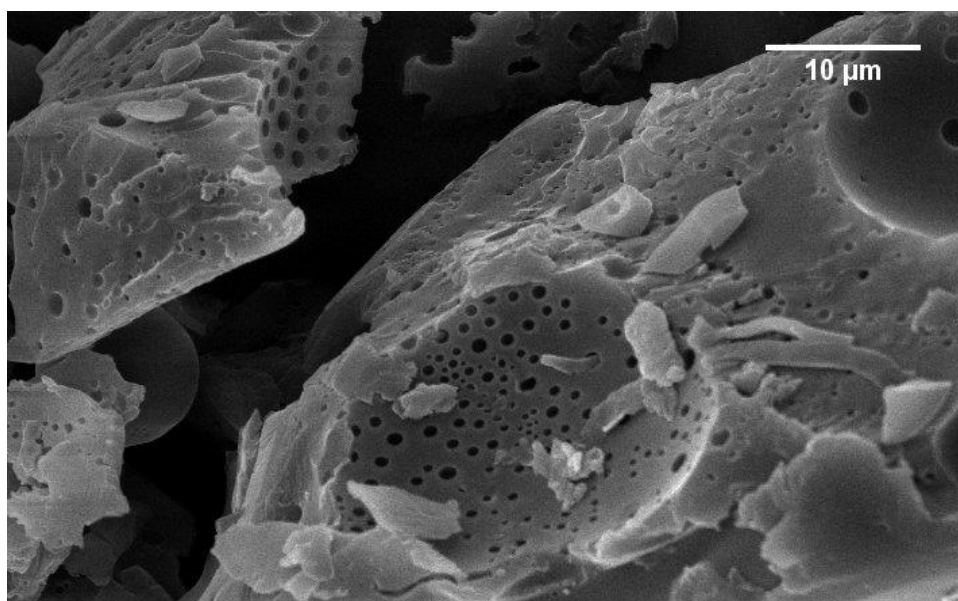


Figure 48: SEM of a cross section of a polystyrene particle produced with a polystyrene in THF solution with PS M_w of 30 kg mol^{-1} and a coagulation bath composed of 1 : 0.1 water/THF. A greater level of porosity is observed within the internal structure. A larger number of pores are within the desired range of 200 – 700 nm.

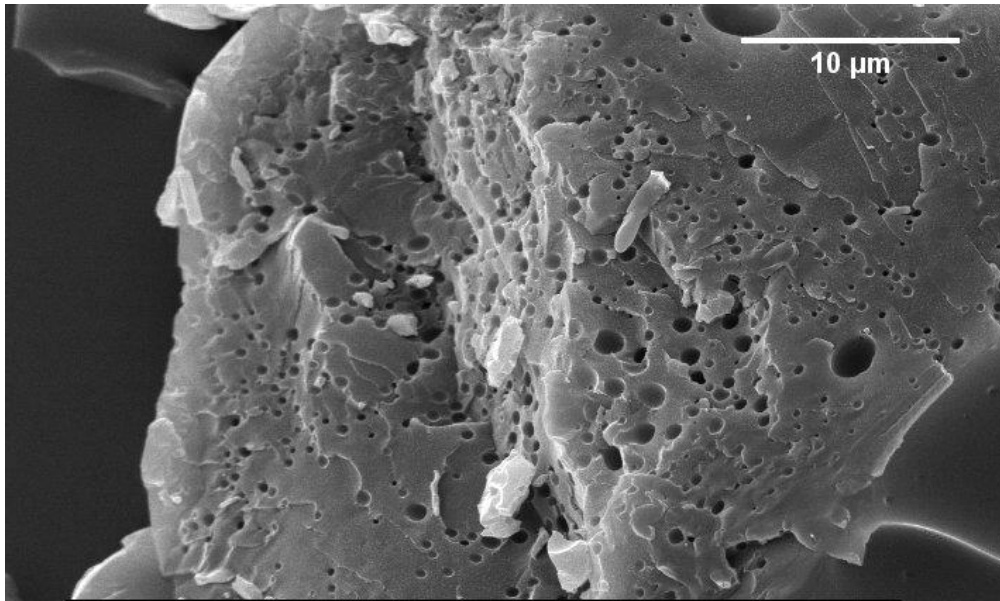


Figure 49: SEM of a cross section of a polystyrene particle produced with a polystyrene in THF solution with PS M_w of 30 kg mol^{-1} and a coagulation bath composed of only water. Extensive porosity is present within the internal structure. Pores are variable in size with a large number in the desired range of 200 – 700 nm.

This initial proof of concept demonstrated that porous polystyrene particles were achievable by using low molecular weight polystyrene and a coagulation bath with a high ratio of non-solvent to solvent. The particles demonstrated an internal porosity, produced by a mechanism of phase separation comprised of a nucleation and a growth, with spherical not interconnected pores, similar to the *Garrulus glandarius*'s foam structures. However, the control of the particles' shape and size was an issue to address.

FABRICATION PROCESS BY INK-JET.

In order to improve the control over the polystyrene particles' shape and size, an upgrade of the fabrication set up was required, and achieved by employing an Ink-Jet apparatus.

The Ink-Jet was able to provide a greater control over the droplets' size of the polystyrene solution delivered to the coagulation bath. In particular, the Ink-Jet was capable of producing a steady stream of small droplets, consistent in size. The apparatus, comprising a pressure controller connected simultaneously to a compressed air source, to a vacuum pump and to a reservoir chamber containing the polystyrene solution, allowed the creation of a slightly negative pressure in the reservoir (Figure 50). One end of the reservoir was linked to an Ink-Jet nozzle of 60 μm in diameter, containing a piezo-electric diaphragm along the wall of the nozzle, and connected to an electronic pulse controller. The electric current generated by the controller induced the contraction and the relaxation of the piezo-electric diaphragm, producing a series of pulses (waves) able to push the polystyrene solution out through the nozzle.⁷⁵ This way a steady stream of similarly sized droplets of about 60 μm in diameter was generated and delivered to a bath of water non-solvent, held in a glass vial, placed at a distance of \approx 6 or 7 cm from the nozzle (Figure 53).

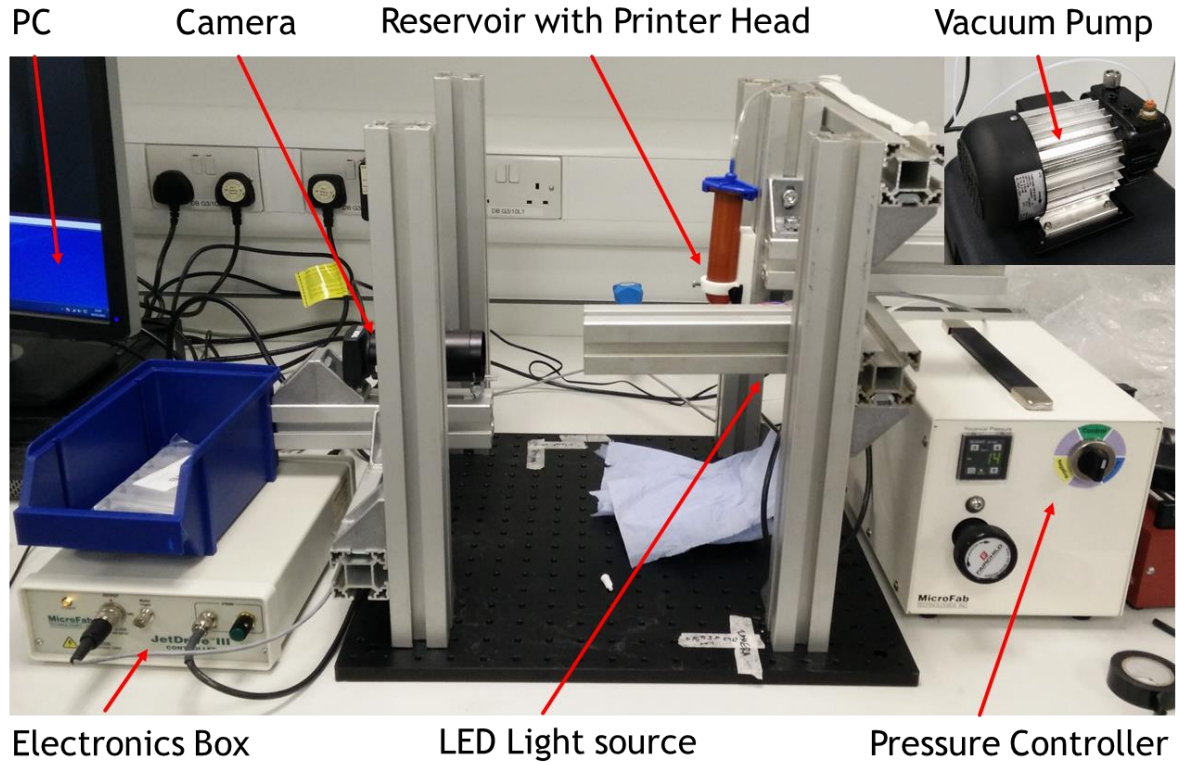


Figure 50: Ink Jet set up: on the right, a vacuum pump and a compressed air source (not visible) were connected to the pressure controller box and to the reservoir, allowing to generate a slightly negative pressure in the reservoir chamber containing the polystyrene solution. The electric box on the left was connected to the printer head attached to the bottom of the reservoir, allowing the control of the pulses produced by the piezo-electric diaphragm in the printer head and thus the generation of a steady stream of polystyrene solution droplets. The camera and the strobe LED light source were aligned with the printer head nozzle to visualise the stream of droplets in the PC monitor on the left.

The set up required the alignment of a camera with the printer head and the strobe LED light source, in order to visualise the droplets stream on a monitor (Figure 51). The pressure generated by the compressed air and the vacuum pump in the reservoir chamber was balanced using the pressure controller, in order to produce a slightly negative pressure of ≈ -14 mbar.

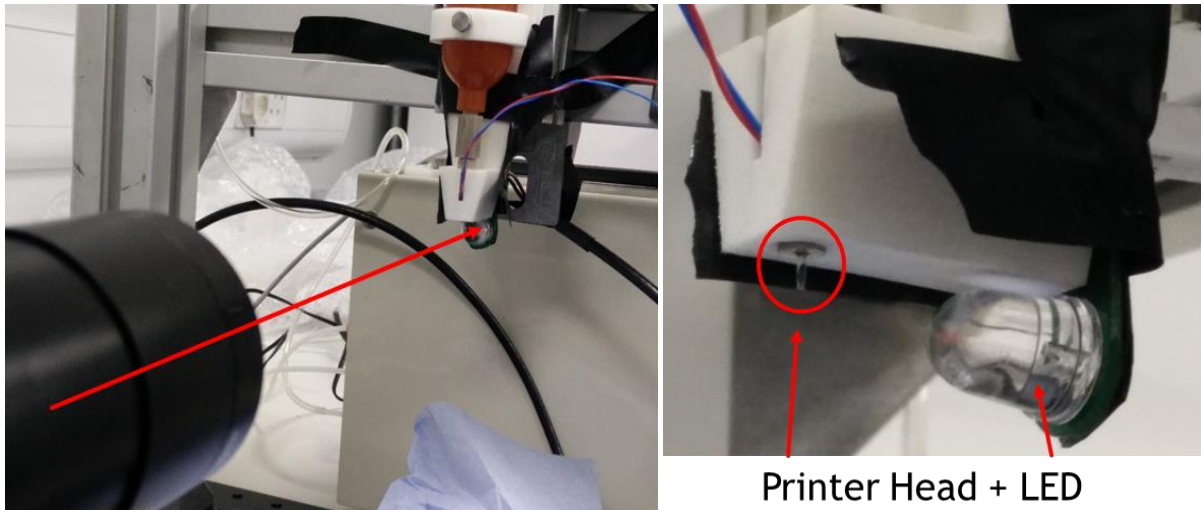


Figure 51: Alignment of camera – LED – Printer head: in order to visualise the droplets stream of polystyrene solution, a camera was aligned with the printer head and a strobe LED light source capable of producing short flashes of light. The strobe delay was set at $\approx 1000 \mu\text{s}$. The image of the droplets stream was monitored on a PC with UC 480 Viewer software.

The wave-form parameters that controlled the oscillation of the piezo-electric diaphragm in the printer head,⁷⁵ generating the droplets stream, were optimised by a trial and error process, until a steady stream was achieved. The wave-form consisted of two trapezoidal pulses (Figure 52): the first pulse (or resonating pulse) is controlled by the rise time 1, the dwell time and the fall time parameters, and it is responsible for the droplet jet.⁷⁶ The resonance of the piezo also generates a residual oscillation, which can be cancelled by inducing a negative trapezoidal pulse (called the quenching pulse).⁷⁷

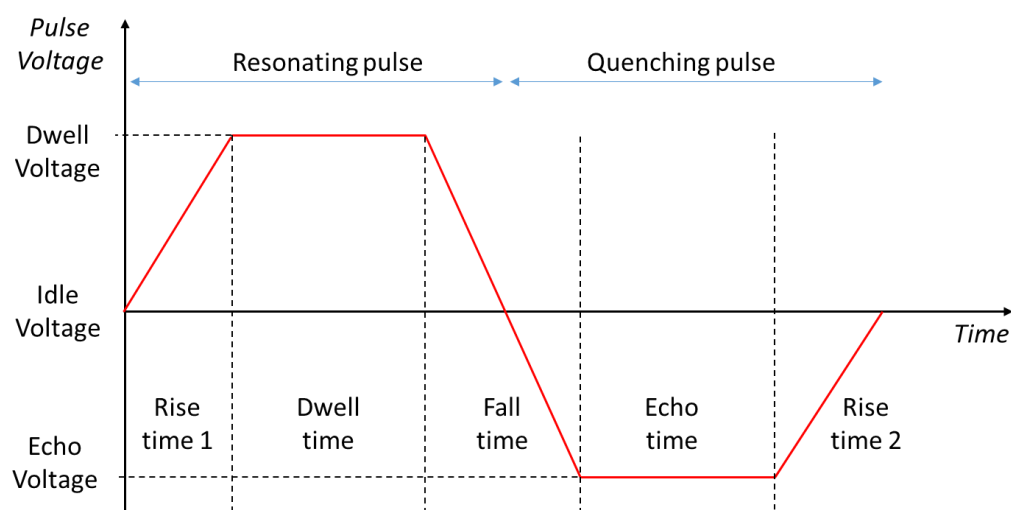


Figure 52: A schematic diagram of a bipolar pulse wave-form. The resonating pulse (producing the droplet jet) and the quenching pulse are highlighted. The Ink-Jet operating parameters controlling the pulses are indicated.

This cyclic sequence of a resonating pulse followed by a quenching pulse produces the steady droplets stream. The optimised configuration was obtained with the following values of the Ink-Jet operating parameters:⁷⁵

Resonating pulse / μs			Quenching pulse / μs		Voltage settings / V		
Rise time 1	Dwell time	Fall time	Echo time	Rise time 2	Idle	Dwell	Echo
4	15	15	25	25	0	30	-10

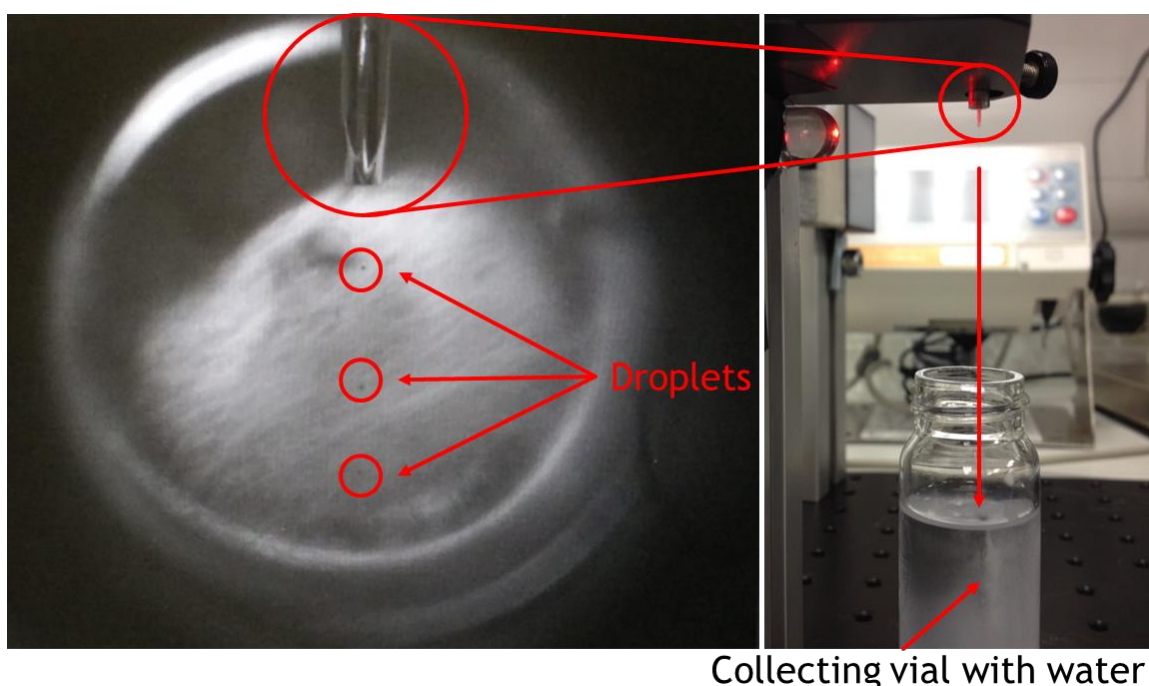


Figure 53: Visualisation of the droplets stream: on the left side, the image recorded by the camera and visualised on the PC using the UC 480 Viewer software, highlights the steady stream of droplets of the polystyrene solution. The printer head's nozzle and some droplets are visible. On the right, the stream of droplets delivered to the coagulation bath of water can be observed.

The Ink-Jet method was employed with a solution of polystyrene of M_w of 23 kg mol^{-1} in THF at room temperature, with a concentration of 10% by weight of the polymer (below C^*). The particles produced were isolated from the coagulation bath, containing only water, by vacuum filtration and characterised by SEM once fully dried. The same solution was also used to produce particles by the standard lab method by syringe (with a needle gauge of $\approx 0.7 \text{ mm}$ inner diameter) and syringe pump. The comparison of SEM images of the particles obtained from the same polymer solution employing the Ink-Jet (Figure 54) and the standard lab method (Figure 55) showed that the Ink-Jet was

successful in providing a greater control of particles' shape and size. The particles obtained by Ink-Jet were spherical, consistent in size, in the desired size-range, exhibiting internal porosity, with a greater pore density.

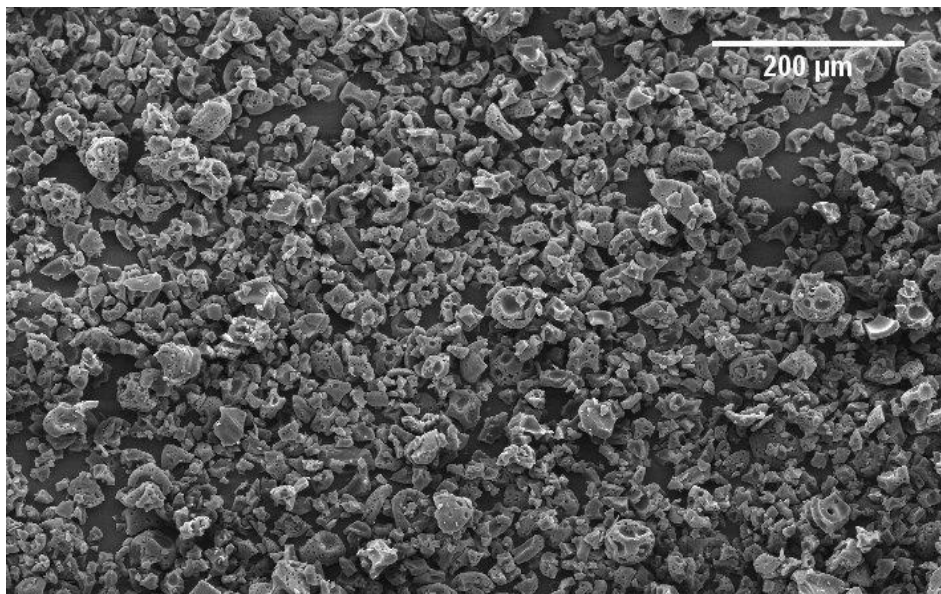


Figure 54: A representative SEM image of the polystyrene multi-voided particles produced with polystyrene of M_w 23 kg mol^{-1} in THF by the Ink-Jet process. The particles are rounded, smaller (up to $\approx 60 \mu m$ in diameter) and consistent in size. This image shows that the Ink-Jet process was successful in achieving a greater control of particles' shape and size.

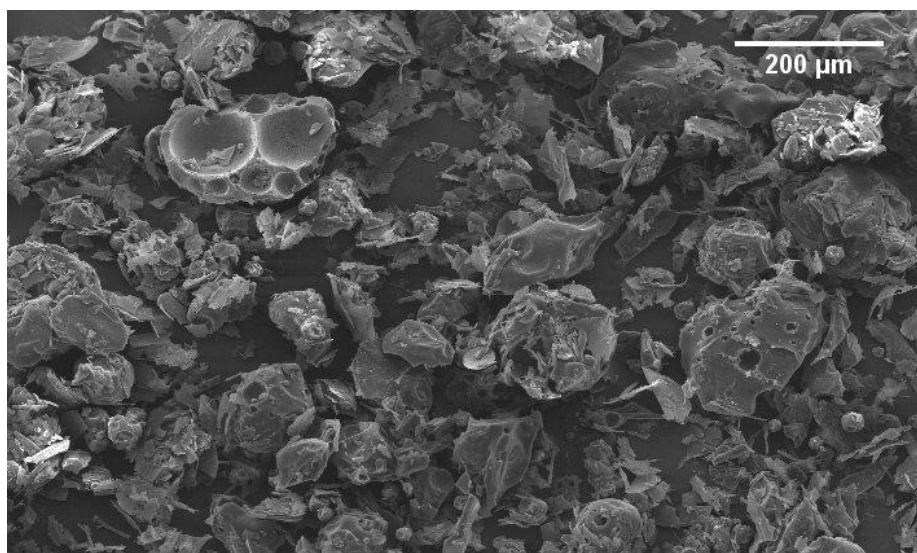


Figure 55: A representative SEM image of the polystyrene multi-voided particles produced with polystyrene of M_w 23 kg mol^{-1} in THF by the standard lab process employing a syringe (with a needle gauge of ≈ 0.7 mm of inner diameter) connected to a syringe pump. The particles have irregular shapes, are larger in size, up to $\approx 200 \mu m$ in diameter.

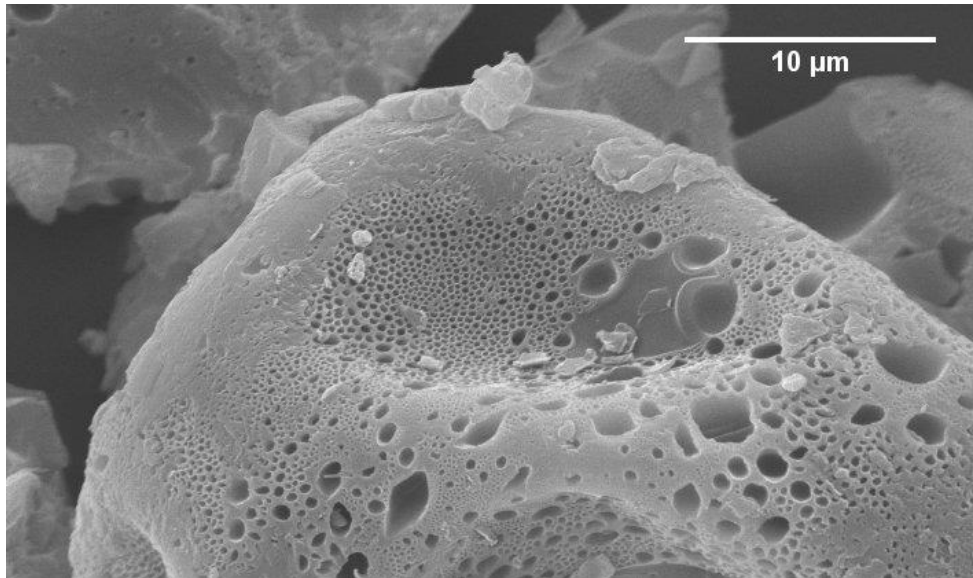


Figure 56: SEM of a cross section of a polystyrene particle produced with polystyrene of M_w 23 kg mol^{-1} in THF by the Ink-Jet process. The particle is spherical and $\approx 40 \text{ }\mu\text{m}$ in diameter. The pores are variable in size, with a large number within the desired range for visible light scattering, 200-700 nm.

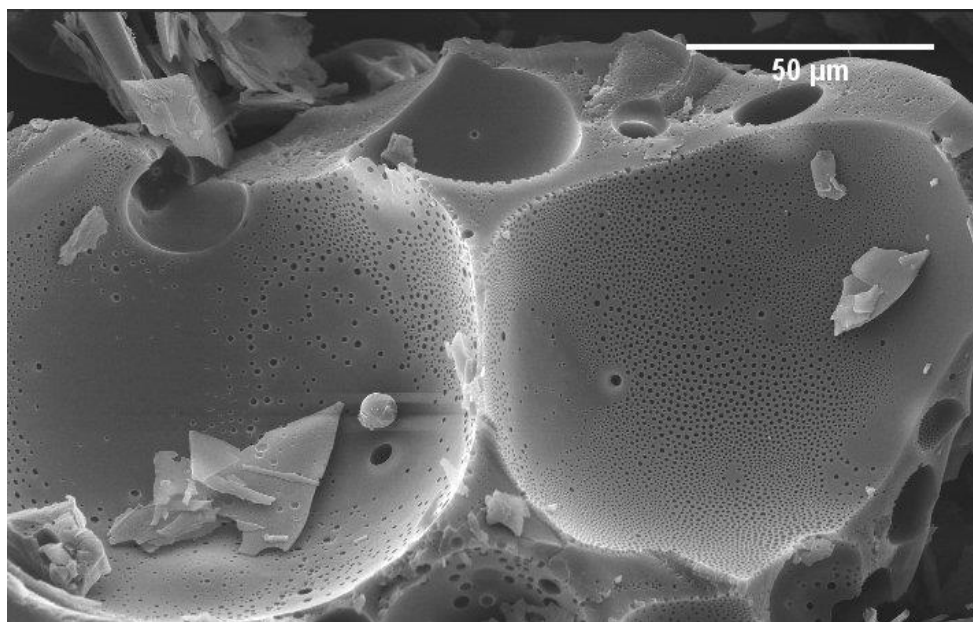


Figure 57: SEM of a cross section of a polystyrene particle produced with polystyrene of M_w 23 kg mol^{-1} in THF by the standard lab process. The particle is very large with an irregular shape. Pores present a greater variability in size, but with a large number still within the desired range for visible light scattering, 200-700 nm.

The Ink-Jet method solved the fabrication issues, giving the means to produce particles with the desired features in terms of shape, size and porosity. The greatest limitation of this method was the difficulty of scaling up the process in order to produce sufficient particles for testing. The Ink-Jet works with small volumes, it is relatively slow and the product that could be obtained in a daily

session was in the order of a tenth of a gram of particles. This did not offer the opportunity for a full characterisation (it was only sufficient for SEM imaging) and certainly not for testing the product within paint formulations, where about 50 g of material were required. Nonetheless, the Ink-Jet method proved that polystyrene multi-voided particles with the desired shape and morphological features were indeed achievable.

CHAPTER 6: MULTI-VOIDED POLYSTYRENE PARTICLES BY A PROCESS OF NON-SOLVENT INDUCED PHASE SEPARATION OF A POLYSTYRENE EMULSION.

NIPS BY EMULSION - FABRICATION PROCESS.

The Ink-Jet method was successful in achieving the target particles, with the right shape and size. The particles presented a foam-like internal structure, made of spherical closed pores generated by a process of phase separation by nucleation and growth. However, the limited amount of product that could be obtained by employing the Ink-Jet was insufficient for a full characterisation of the system and for the implementation of the multi-voided particles in paint formulations.

A different method for increasing the productivity of polystyrene porous particles was therefore necessary, and a possible option was the modification of the fabrication process from a NIPS by solution, where the polymer solution is directly delivered to the coagulation bath, to a NIPS by emulsion, where the polymer solution is first dispersed in the form of small droplets within a continuous phase of a second liquid, and then it is delivered to the coagulation bath.

The dispersion of the polystyrene solution in the form of small droplets within a continuous phase allows a greater degree of control over the particles' shape. Surface tension is responsible for the spherical shape of the polymer solution droplets. When the emulsion is delivered to the coagulation bath, the diffusion of the non-solvent induces the precipitation of the polystyrene within the spherical droplets. The precipitated polystyrene retains the shape of the original droplets, therefore producing spherical particles.

The particles' size is directly related to the polymer solution droplets size, which can be easily controlled by varying the shear rate during the emulsion mixing. Increasing the shear has the effect of breaking down the discontinuous phase into smaller droplets. The coagulation of the droplets can be prevented by increasing the levels of surfactant, thus reducing the surface tension within the system.

The NIPS by emulsion process had the potential of producing particles with controllable shape and size in bulk, and therefore in larger quantities compared to the previous process. Particles' shape and size could now be controlled due to the nature of the emulsion, rather than relying on the Ink-Jet, a sophisticated and slow apparatus, producing streams of small and consistent droplets.

In the non-solvent induced phase separation method by emulsion, the first step of the process is analogous to the method by solution previously discussed, and polystyrene in the form of pellets is dissolved in the toluene solvent at room temperature to produce polymer solutions of desired concentration by weight (Figure 58). In order to form and stabilise the emulsion, an amount of 2% by weight of non-ionic surfactant span 80 was added to the polymer solution and dispersed by magnetic stirring.

Deionised water was added to the polystyrene solution and span 80 mixture, in a 2 : 1 ratio by weight, and the whole mixture was stirred at ≈ 1000 rpm (rate per minute) for ≈ 20 minutes, in order to form a stable emulsion.

The high shear produced by the stirring had the effect of inter-dispersing the polystyrene solution and the deionised water: the non-ionic surfactant span 80, migrating at the interface between the two liquids, favoured the formation of polystyrene solution droplets dispersed into a continuous phase of water.

Continuous stirring at ≈ 1000 rpm broke down the polystyrene solution droplets until they reached average diameters in the range of $\approx 20 - 70$ μm , in order to achieve particles with dimensions comparable to those previously produced with the Ink-Jet method. The average droplets size of the emulsions was measured by dynamic light scattering (DLS) before proceeding with the final steps.

The emulsion was then transferred to a 60 ml syringe (with a needle gauge of ≈ 0.7 mm inner diameter) connected to a syringe pump. The flow rate was set to 100 ml hr^{-1} in order to deliver the emulsion to a stirring bath of ethanol non-solvent. The emulsion to non-solvent ratio was kept close to 1 : 10 by weight for all the samples. The precipitated polystyrene micro-spheres were isolated from the mixture by vacuum filtration and left to dry in a fume cupboard to remove all the liquids.

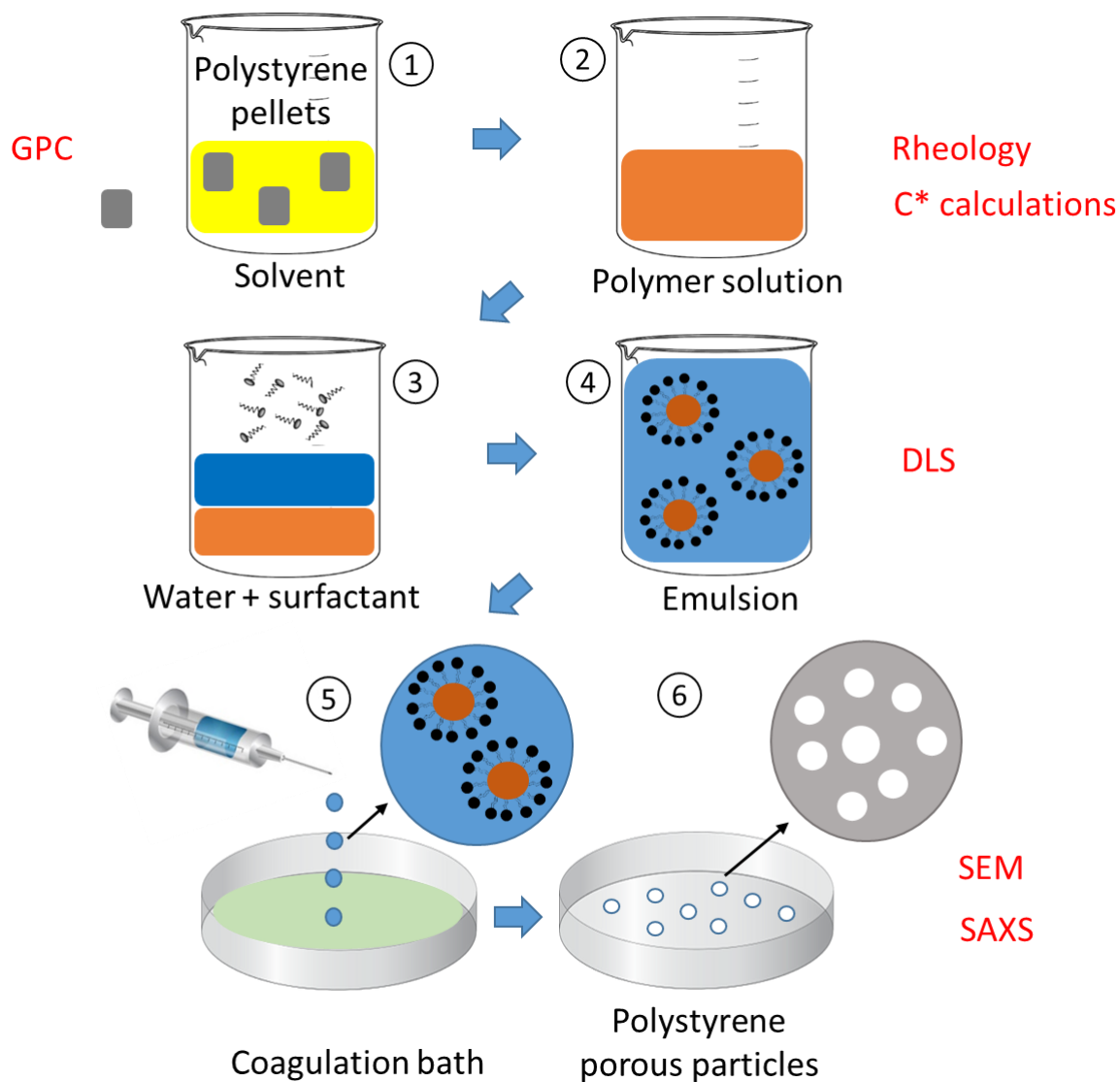


Figure 58: Non-solvent induced phase separation by emulsion process. Polystyrene is dissolved in toluene solvent (step 1) to produce a polymer solution of desired concentration by weight (step 2). Span 80 non-ionic surfactant and deionised water are added to the polymer solution (step 3). An emulsion, with polystyrene solution droplets dispersed in a continuous phase of deionised water, is produced by stirring the mixture (step 4). The emulsion is delivered drop-wise by a syringe (with a needle gauge of ≈ 0.7 mm inner diameter) connected to a syringe pump, to a coagulation bath of ethanol non-solvent (step 5). Polystyrene precipitates within the spherical droplets retaining the spherical shape. The particles are isolated from the mixture by vacuum filtration and left to dry (step 6) to remove the liquids. For each step of the process, the characterisation techniques used are highlighted in red: GPC was performed before step 1 to determine the polystyrene molecular weight. Rheology and C^* calculations were performed on the polystyrene solutions, in step 2. DLS was employed to determine the droplets size in the emulsions in step 4. SEM and SAXS were performed on polystyrene dried particles, after step 6.

In order to fully characterise the emulsion systems and to evaluate the effects of variables such as polystyrene molecular weight and polystyrene concentration in the polymer solution on the particles' morphology, three different uni-modal samples of polystyrene with molecular weights of

23, 207 and 317 kg mol⁻¹ were employed, along with a bi-modal sample with two populations of polymer chains of M_w of 53 and 107 kg mol⁻¹.

Five different polystyrene concentrations in toluene were investigated: 2, 5, 7, 10 and 15% by weight of polystyrene in solution.

The samples prepared with the emulsion process were listed in terms of the polystyrene molecular weights and polystyrene concentrations. For example, the products prepared with polystyrene M_w 23 kg mol⁻¹ at 2% w/w, M_w 207 kg mol⁻¹ at 5% w/w and bi-modal M_w 53 and 107 kg mol⁻¹ at 10% w/w concentration, would be referred to as “23-2”, “207-5” and “bi-modal 10” respectively.

CHARACTERISATION OF POLYSTYRENE BY GPC.

The molecular weight of the polystyrene samples used for the NIPS by emulsion process was measured by gel permeation chromatography (GPC).

The uni-modal lower M_w sample (Polymer Source Lot. Number P9397-S), was analysed at the University of Sheffield with a GPC set-up comprised of two 5 μ m “Mixed-C” columns, a WellChrom K-2301 refractive index detector operating at 950 nm, THF eluent containing 2% v/v triethylamine and 0.05% w/v butylhydroxytoluene (BHT) with a flow rate of 1.0 mL min⁻¹, calibrated with polystyrene standards from Polymer Laboratories (Church Stretton Salop, England). The analysis provided a molecular weight M_w of 23092 g mol⁻¹ (approximated to 23 kg mol⁻¹) with a polydispersity index of 1.24.

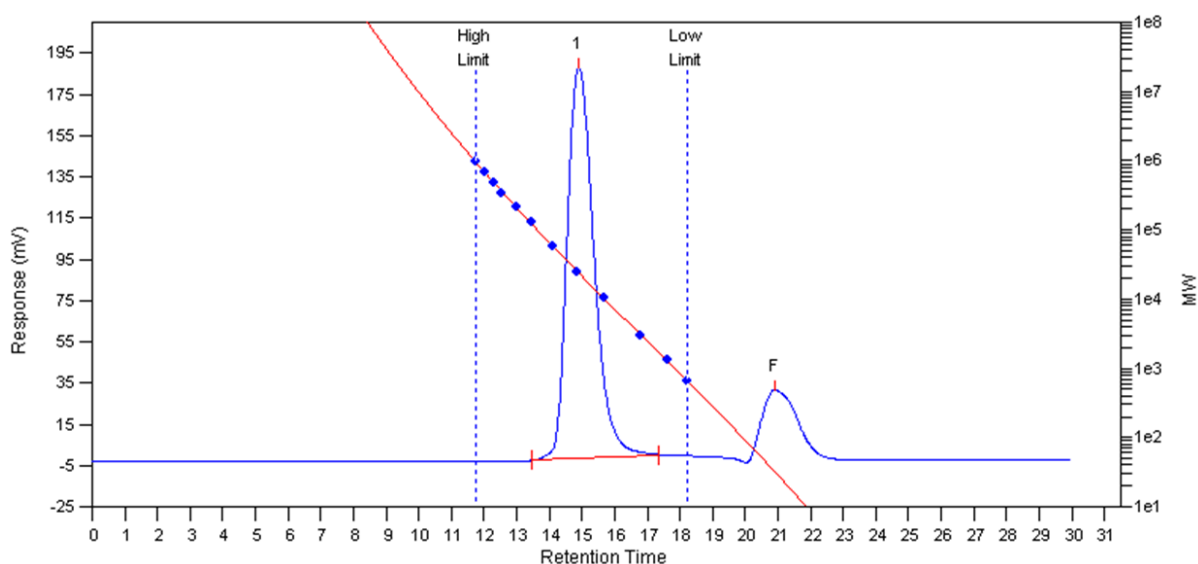
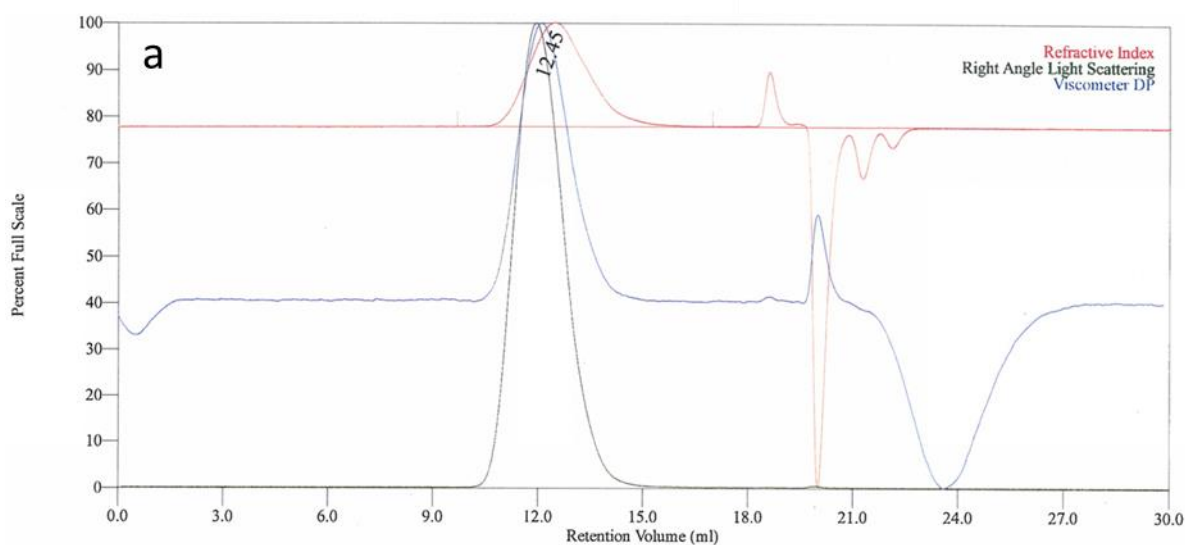


Figure 59: The GPC chromatogram for the polystyrene M_w 23 kg mol⁻¹ recorded at the University of Sheffield. The single peak at \approx 15 min confirms that this is a uni-modal sample, with a single chain population present. The calibration curve on the second vertical axis was used to assign the correct value of molecular weight to the sample.

GPC analysis for all the other samples was performed at the Durham University, using triple detection with light scattering, giving absolute data.

Polystyrene samples were dissolved in a tetrahydrofuran (THF) solvent; the flow rate was set to 1.0 ml min⁻¹, the injection volume was 100 µl, detector and column temperature was set at 35 °C.

The analysis provided a molecular weight M_w of 207,179 g mol⁻¹ (approximated to 207 kg mol⁻¹) with a polydispersity index of 2.10, for the uni-modal intermediate M_w sample (Sigma Aldrich, Lot. number 02726DE) and a M_w of 316,573 g mol⁻¹ (approximated to 317 kg mol⁻¹) with a polydispersity index of 2.95 for the uni-modal higher M_w sample (Sigma Aldrich, Lot. number MKBP1175V). The bi-modal sample (Sigma Aldrich, Lot. number MKBS6957V) showed two populations of polymer chains with molecular weights M_w of 53,309 and 106,970 g mol⁻¹ (approximated to 53 and 107 kg mol⁻¹). From the analysis of the area beneath the two peaks in the chromatogram (Figure 60 c), it was possible to estimate that the composition of the bi-modal blend was of 44.6 % for the polymer chain population of 53 kg mol⁻¹ and of 55.4 % for the polymer chain population of 107 kg mol⁻¹.



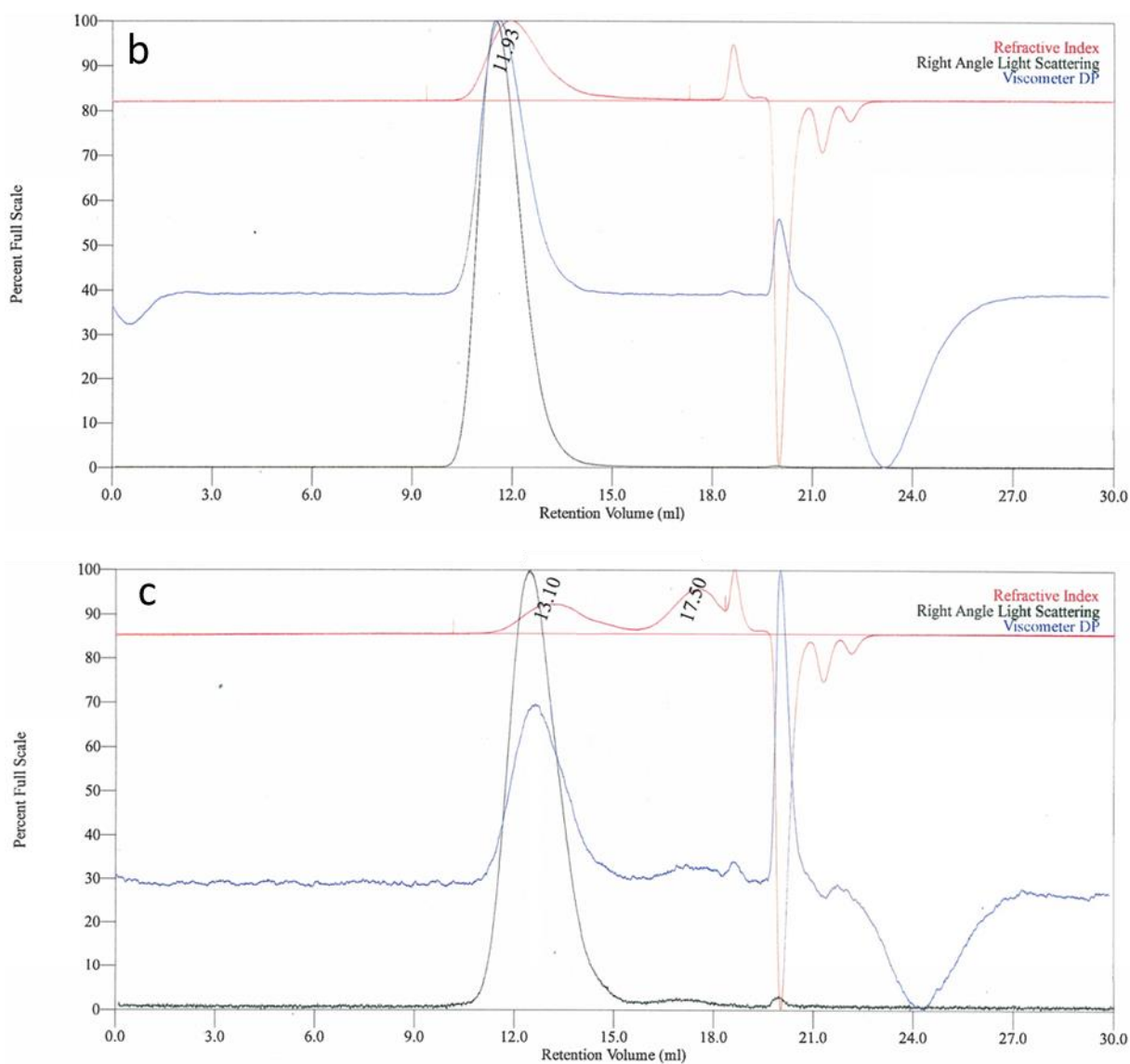


Figure 60: GPC chromatograms for the polystyrene M_w 207 kg mol⁻¹ (a), M_w 317 kg mol⁻¹ (b) and bi-modal M_w 53, 107 kg mol⁻¹ (c) recorded at the Durham University by Prof Hutchings' group. A triple detection by refractive index (red line), light scattering (black line) and viscosity (blue line) was used to measure the molecular weight of the samples. Polystyrene with M_w 207 kg mol⁻¹ (a) and M_w 317 kg mol⁻¹ (b) exhibit a single peak at 12.45 and 11.93 ml respectively, indicating uni-modal samples. Polystyrene bi-modal (c) shows two peaks at 13.10 and 17.50 ml, demonstrating that two chain populations are present.

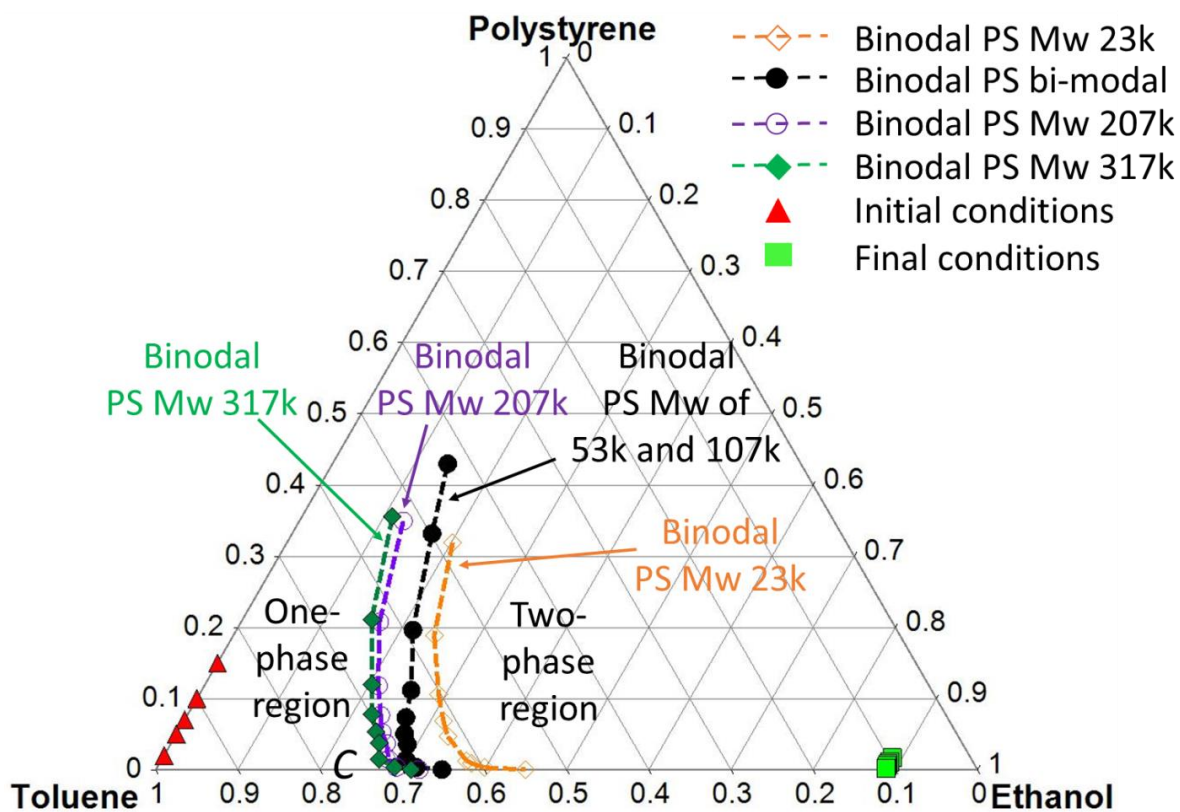
PHASE SEPARATION OF POLYSTYRENE – TOLUENE – ETHANOL SYSTEMS.

In order to determine the topography of the phase separation process on an isothermal ternary phase diagram for the polystyrene, toluene and ethanol system, cloud point measurements for polystyrene solutions were obtained. The cloud points were determined by turbidimetric titration at the temperature of 25 °C.

The volume of ethanol non-solvent, required to achieve cloudiness in solutions of different concentrations of polystyrene, were converted into weights. Each point on the ternary diagram in (Figure 61) is expressed in weight percentage of polystyrene, toluene and ethanol.

Linking the cloud points provides information on the position of the binodals, the boundary lines that separates the one-phase region, where the mixture is homogeneous, from the two-phase region, where the mixture separates into polymer-rich and polymer-poor regions.

The initial condition of the system, for polystyrene toluene solutions at the concentrations of 2, 5, 7, 10 and 15% w/w, lie on the polystyrene-toluene axis of the diagram (Figure 61, triangles). Upon the addition of the non-solvent, the system transits, crossing the binodal boundary, into the two-phase region, initiating phase separation. The diagram shows the final configuration of the system (Figure 61, filled squares) where ethanol is the dominant component and polystyrene is precipitated in the form of solid porous micro-spheres. The binodal boundary is progressively shifted towards the polystyrene-toluene axis as the polystyrene molecular weight increases. The obtained phase diagram (Figure 61) is consistent with a generic ternary diagram expected for such a system (Figure 27).



Initial conditions			Binodal PS 317 kg mol ⁻¹			Binodal PS 207 kg mol ⁻¹			Binodal PS bi-modal			Binodal PS 23 kg mol ⁻¹		
PS %	Tol %	EtOH %	PS %	Tol %	EtOH %	PS %	Tol %	EtOH %	PS %	Tol %	EtOH %	PS %	Tol %	EtOH %
15.00	85.00	0.00	35.60	53.40	11.00	34.95	52.42	12.64	42.99	42.99	14.02	31.94	47.90	20.16
10.00	90.00	0.00	21.07	63.20	15.73	20.79	62.37	16.84	33.19	49.79	17.02	18.89	56.67	24.44
7.00	93.00	0.00	11.95	67.72	20.33	11.83	67.02	21.15	19.63	58.89	21.48	10.64	60.27	29.09
5.00	95.00	0.00	7.76	69.81	22.44	7.65	68.82	23.53	11.18	63.34	25.48	6.84	61.58	31.58
2.00	98.00	0.00	5.31	70.55	24.14	5.26	69.85	24.89	7.32	65.91	26.77	4.68	62.12	33.20
Final conditions			3.73	70.93	25.33	3.69	70.11	26.20	5.06	67.20	27.74	1.26	61.57	37.18
1.69	9.56	88.75	1.47	72.04	26.49	1.45	70.95	27.61	3.56	67.61	28.83	0.93	61.12	37.95
1.12	10.12	88.75	0.36	70.82	28.83	0.35	70.55	29.09	1.41	68.85	29.75	0.30	59.84	39.86
0.79	10.46	88.75	0.03	68.94	31.02	0.03	67.96	32.01	0.34	68.14	31.52	0.03	55.02	44.95
0.56	10.69	88.75	-	-	-	-	-	-	0.03	65.16	34.81	-	-	-
0.22	11.02	88.75	-	-	-	-	-	-	-	-	-	-	-	-

Figure 61: An isothermal ternary phase diagram, showing the evolution of a polystyrene-toluene-ethanol system at 25°C. From the initial conditions of polystyrene toluene solutions at PS concentrations of 2, 5, 7, 10 and 15% w/w (triangles) the system transitions to the final state (squares) upon the addition of ethanol non-solvent. Experimentally determined binodal lines, obtained from cloud points, are shown for polystyrene molecular weights of 23 (open diamonds), 207 (open circles), 317 (full diamonds) and bi-modal of 53 and 107 (full circles) kg mol⁻¹, marking the boundary between one-phase and two-phase regions. The cloud points were measured up to 40% w/w initial PS concentration for PS M_w 23, 207, 317 kg mol⁻¹ and 50% w/w for PS bi-modal blend. Beyond these concentrations, the solutions are too viscous to perform the analysis. Phase separation occurs when the binodal line is crossed, initially producing a liquid-liquid mixture with polymer-rich and polymer-poor regions and, upon further addition of ethanol, a solid-liquid mixture occurs where polystyrene precipitates. In the table, the numerical data generating the phase diagram, expressed in polystyrene, toluene and ethanol weight percentages, are reported.

CHARACTERISATION OF POLYSTYRENE SOLUTIONS: CRITICAL CHAIN OVERLAP CONCENTRATION.

The chain overlap concentration C^* of a homogeneous polymer solution is defined as the critical concentration at which polymer coils begin to overlap.⁶¹

It is expected that above the critical chain overlap concentration, the mobility of polystyrene systems is drastically reduced due to the increased viscosity.

C^* can be calculated from the radius of gyration of a polymer in a solvent, using the Equation 31 previously described in the characterisation techniques section.

The values for the radius of gyration R_g of polystyrene in toluene were obtained using two approaches (Table 1 and Table 2). The first approach was based on the values reported in the literature⁶² (Table 1). The values of R_g chosen for the calculations were those that were the closest to the molecular weights of the studied polystyrene. It was found that for the 23 kg mol⁻¹ series, the 15% w/w concentration sample is the only system above C^* . For the 207 kg mol⁻¹ series, the 2% w/w concentration is the only system below C^* and the 317 kg mol⁻¹ series is entirely above C^* . The bi-modal system is below C^* at 2, 5 and 7% and above C^* at 15%, while at 10% the short and long chains are below and above C^* respectively (Table 1).

Table 1: Calculations of C^* using eq. 31 and experimental values of R_g from literature.⁶² The systems with the concentrations above C^* , where the phase separation process is kinetically controlled, are highlighted in orange. B = Below C^* , A = Above C^* .

PS M_w kg mol ⁻¹	R_g / nm	C^* / g cm ⁻³	2%	5%	7%	10%	15%
23	4.58	0.096	B	B	B	B	A
bi-modal 53 & 107	5.36 & 8.20	0.136 & 0.077	B	B	B	B/A	A
207	13.40	0.034	B	A	A	A	A
317	23.30	0.010	A	A	A	A	A

The second approach used for the C^* calculation is based on the R_g values obtained from the Kuhn length of polystyrene in a theta-solvent.

In this case R_g is calculated from the relation between the contour length and the Kuhn length (Equation 29). The Kuhn length of polystyrene used is 1.67 nm, as reported in literature⁶⁴.

The contour length of polystyrene was calculated from Equation 30 using the values of 0.154 nm for carbon-carbon bond length of the polystyrene skeleton, 70.53° for the tetrahedron angle, and the

number of repeat units in the polymer chain, N , was obtained by dividing the molecular weight M_w of polystyrene by the molecular weight M_u of the monomer styrene unit ($104.15 \text{ g mol}^{-1}$).

Thus, R_g calculated from Equation 29 was used for the C^* calculations (Equation 31). The results show (Table 1 and Table 2) that both approaches predict a similar behaviour for the studied systems. There is a slight difference observed for the high molecular weight solutions (Table 2, compositions highlighted by patterned boxes). The results of the first approach (Table 1) based on literature values of R_g were used in the further analysis.

Table 2: C^* estimation using the values of R_g calculated from the Kuhn length and the contour length of polystyrene.⁶⁴ In the orange boxes the systems with concentrations above the critical chain overlap concentration, where the phase separation process is kinetically controlled. The composition exhibiting slight deviations of C^* from the previous method are highlighted by the patterned boxes. B = Below C^* , A = Above C^* .

PS $M_w \text{ kg mol}^{-1}$	R_g / nm	$C^* / \text{g cm}^{-3}$	2%	5%	7%	10%	15%
23	3.93	0.150	B	B	B	B	A
bi-modal 53 & 107	5.97 & 8.48	0.099 & 0.070	B	B	B	B/A	A
207	11.79	0.050	B	B	A	A	A
317	14.57	0.041	B	A	A	A	A

CHARACTERISATION OF POLYSTYRENE SOLUTIONS: VISCOSITY.

The viscoelastic properties of polystyrene, toluene and ethanol systems were measured using a rotational stress-controlled rheometer (Anton Paar, MCR 502) equipped with a cone-and-plate geometry (diameter 50 mm and cone angle 2°) at 25 °C, using the continuous shear mode. The dependence of the viscosity (η) on the shear rate ($\dot{\gamma}$) was measured within $\dot{\gamma}$ intervals from 1 to 100 rad s^{-1} . This range was selected in order to obtain reliable values of zero shear rate viscosity for solutions at low polystyrene concentration. The viscosity η in this range was independent of shear rate (Figure 62). The zero shear viscosity η_0 was extrapolated to $\dot{\gamma} = 0$. Time sweeps performed before each run have shown that the effect of solvent evaporation was negligible for the measurements time used.

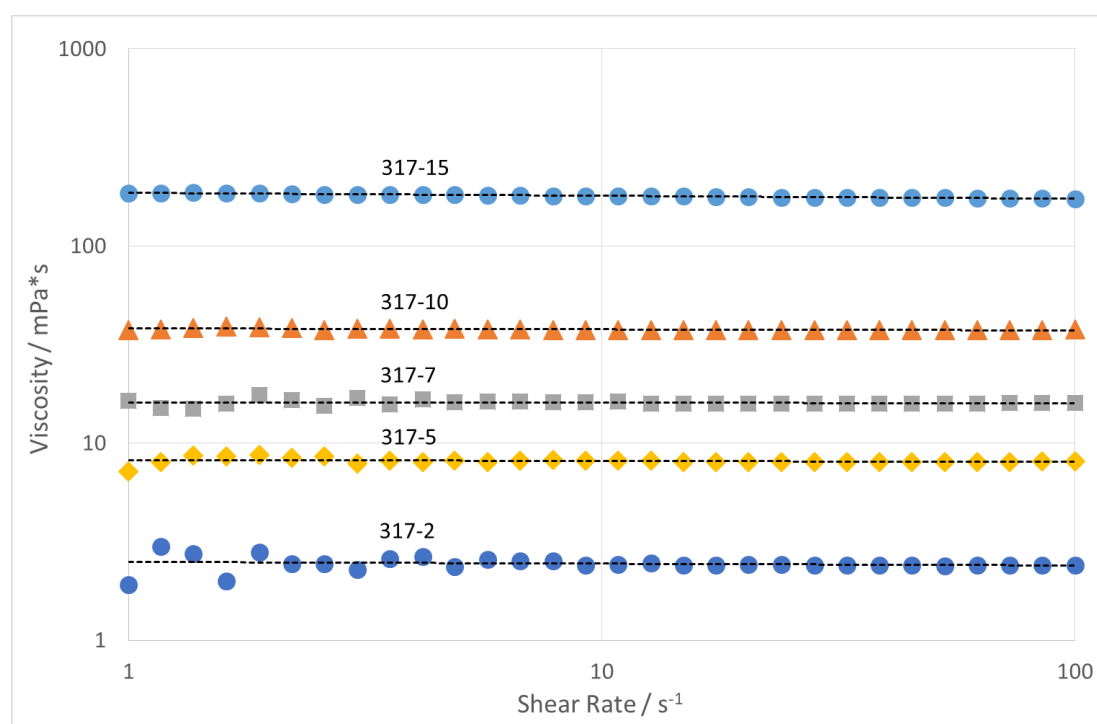
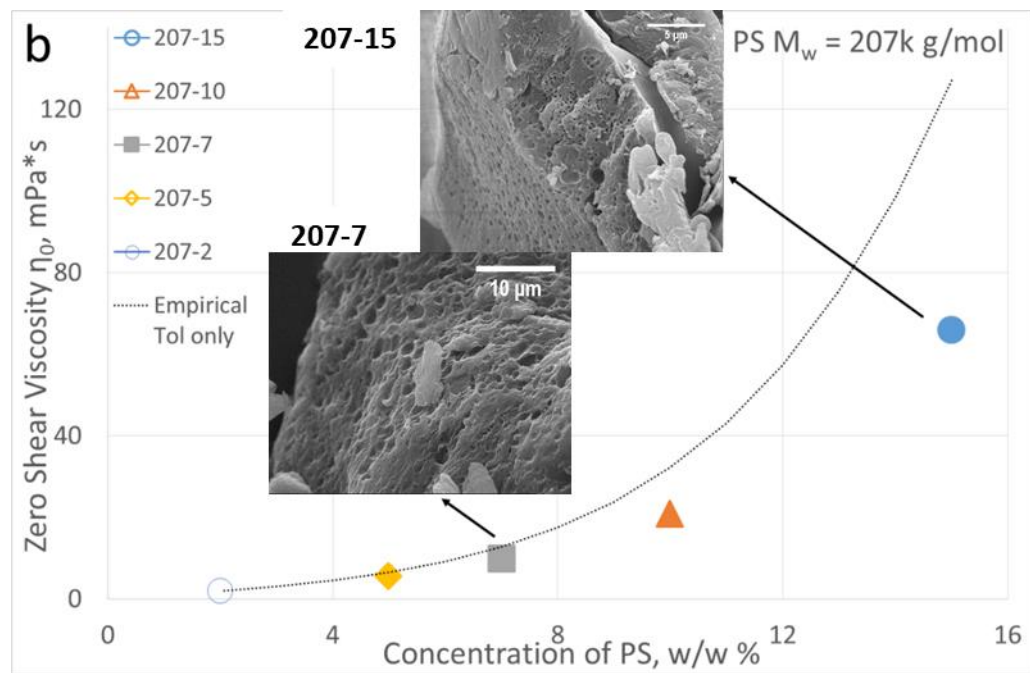
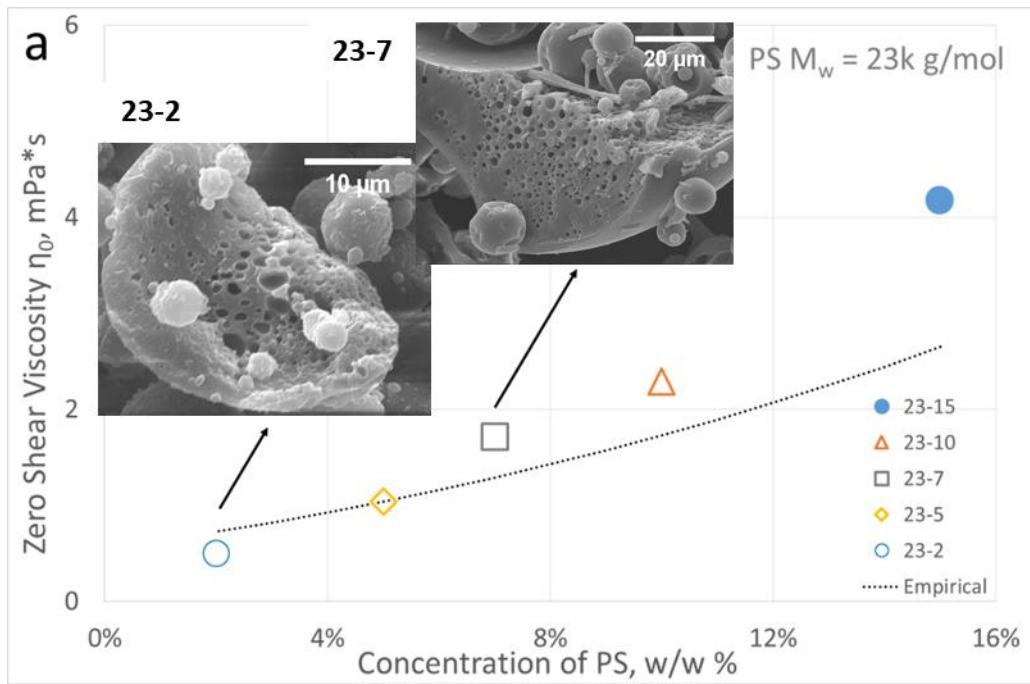


Figure 62: A representative measurement of shear viscosity of the polystyrene solutions with PS $M_w = 317 \text{ kg mol}^{-1}$ and PS concentration of 2 to 15 % wt. The diagram shows that the viscosity η is independent of shear rate.

Solutions of polystyrene in toluene at the initial concentrations of 2, 5, 7, 10 and 15% w/w were prepared for each of the polystyrene molecular weights. The Zero shear viscosity η_0 data were then obtained (Figure 63).



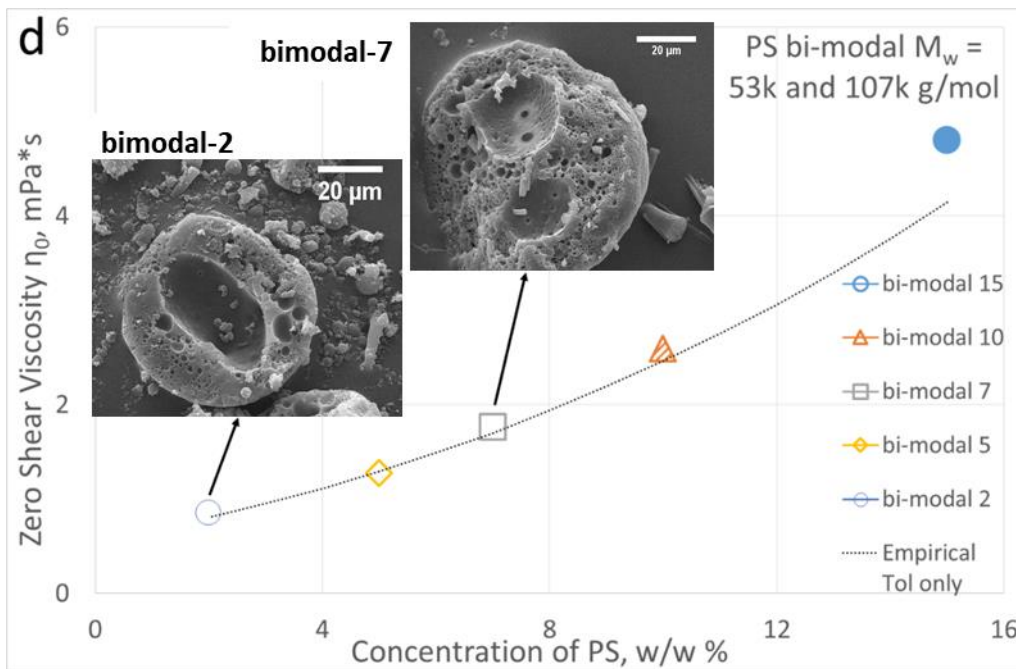
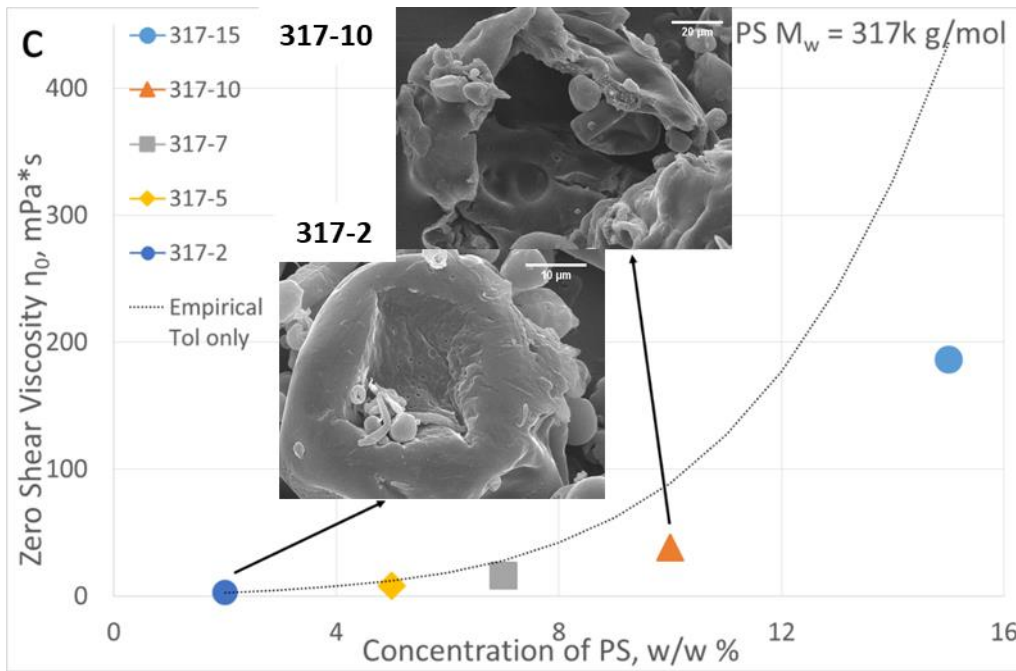


Figure 63: Zero shear viscosity η_0 versus polystyrene concentration measured for polymer solutions with $M_w = 23$ kg mol⁻¹ (a), 207 kg mol⁻¹ (b), 317 kg mol⁻¹ (c) and bi-modal 53 and 107 kg mol⁻¹ (d). Filled symbols represent concentration above C^* where polymer chains entanglement occurs and the phase separation is kinetically controlled. Open symbols represent concentrations below C^* . The hatched symbol for “bi-modal 10” indicates that only the long chains of the bi-modal sample are above C^* . The dotted line was obtained using an empirical relationship between zero shear viscosity, polystyrene molecular weight and polystyrene concentration for polystyrene-toluene systems from literature⁷⁸ (Equation 42). The relationship predicts the zero shear viscosity of polymer-solvent solutions. Inserts show representative SEM cross-section images of polystyrene particles obtained from these solutions.

A dotted-line overlapping the experimental data was generated by using an empirical equation from literature that relates the zero shear viscosity η_0 of polystyrene-toluene systems to polystyrene molecular weight M_w and polystyrene concentration C .⁷⁸

$$\eta_0 = 4.81 \times 10^{-3} \times C \times M_w^{0.736} + 1.658 \times 10^{-5} \times C^2 \times M_w^{1.472} + 5.579 \times 10^{-13} \times C^{4.55} \times M_w^{3.35} + 0.558 \quad \text{Equation 42}$$

The predicted viscosity is in good agreement with the experimental data for the low molecular weight polymer and for the high molecular weight polymer at low concentrations. Slight deviations were observed for the high molecular weights at higher concentrations.

CHARACTERISATION OF EMULSION DROPLETS SIZE.

The droplet size of the emulsions of polystyrene solutions dispersed in water was measured by dynamic light scattering (DLS), using a Malvern Zetasizer Nano-S series instrument with 1 ml cuvettes. The instrument was operated under the following conditions: temperature of 25 °C, detector angle at 90°, incident laser wavelength of 633 nm. DLS has shown that droplet diameters in the emulsions for all the prepared samples were in the size range $\approx 20 - 70 \mu\text{m}$.

Table 3: The values of average droplets diameters (Z-average) and polydispersity index (pdi), obtained by DLS measurements.

PS 23 kg mol ⁻¹			PS 207 kg mol ⁻¹		
Sample	Z-Average / μm	pdi	Sample	Z-Average / μm	pdi
23-2	19	0.60	207-2	52	0.38
23-5	67	0.72	207-5	31	0.47
23-7	44	0.43	207-7	30	0.77
23-10	50	0.22	207-10	17	0.68
23-15	18	0.13	207-15	22	0.59
PS 317 kg mol ⁻¹			PS bi-modal 53 & 107 kg mol ⁻¹		
Sample	Z-Average / μm	pdi	Sample	Z-Average / μm	pdi
317-2	45	0.19	bi-modal 2	29	0.38
317-5	62	0.48	bi-modal 5	47	0.39
317-7	72	0.24	bi-modal 7	35	0.43
317-10	37	0.38	bi-modal 10	59	0.67
-	-	-	bi-modal 15	54	0.28

The reason why the droplets show such a broad size range is due to the way the emulsions mixing was achieved. The shear that was provided by the stirrer was not homogeneous throughout the sample. The high shear obtained in the close proximity of the stirrer could not be reproduced in the more peripheral regions of the emulsion. This led to droplets of different size across the sample. However, this was not considered to be an issue due to the fact that a scale up of the process would require the mixing of large volumes of emulsion. The large vessels used in industry, together with the use of overhead mixers, would produce an analogous situation whereby the shear across the sample would not be homogeneous and the same broad size range would be observed. Therefore, the laboratory mixing is representative of the industrial process, making the method industrially robust. The aim of the DLS analysis was simply to make sure that the particles produced were comparable in size to those achieved with the Ink-Jet equipment and close to the ideal range of $\approx 10 - 50 \mu\text{m}$ previously indicated.

CHARACTERISATION OF MULTI-VOIDED POLYSTYRENE PARTICLES BY SAXS.

SAXS measurements were either performed at a synchrotron source (ESRF, beamline ID02, Grenoble, France) or using a laboratory SAXS instrument at the University of Sheffield (Xeuss 2.0, Xenocs, France) equipped with liquid gallium Metal-Jet X-ray source (Excillum, Sweden). A monochromatic X-ray radiation (wavelength $\lambda = 0.0995$ nm or 0.134 nm, respectively) and 2D detector (Rayonix MX-170HS CCD or Dectris Pilatus 1M pixel detector, respectively) were used for these experiments. The SAXS camera length was set to cover the q range from 0.01 nm^{-1} to 1.0 nm^{-1} , where $q = 4\pi\sin\theta/\lambda$ is the modulus of the scattering vector and θ is half of the scattering angle. Glass capillaries (approximate diameter of 2 mm) were used as a sample holder for the dried polystyrene particles. X-ray scattering data were reduced (integration and normalization) using standard routines from the beamline or the software package Foxtrot for the laboratory SAXS instrument. Irena SAS macros⁷⁴ for Igor Pro software were utilized for background subtraction and the scattering patterns were analysed using the Unified fit⁷³ method.

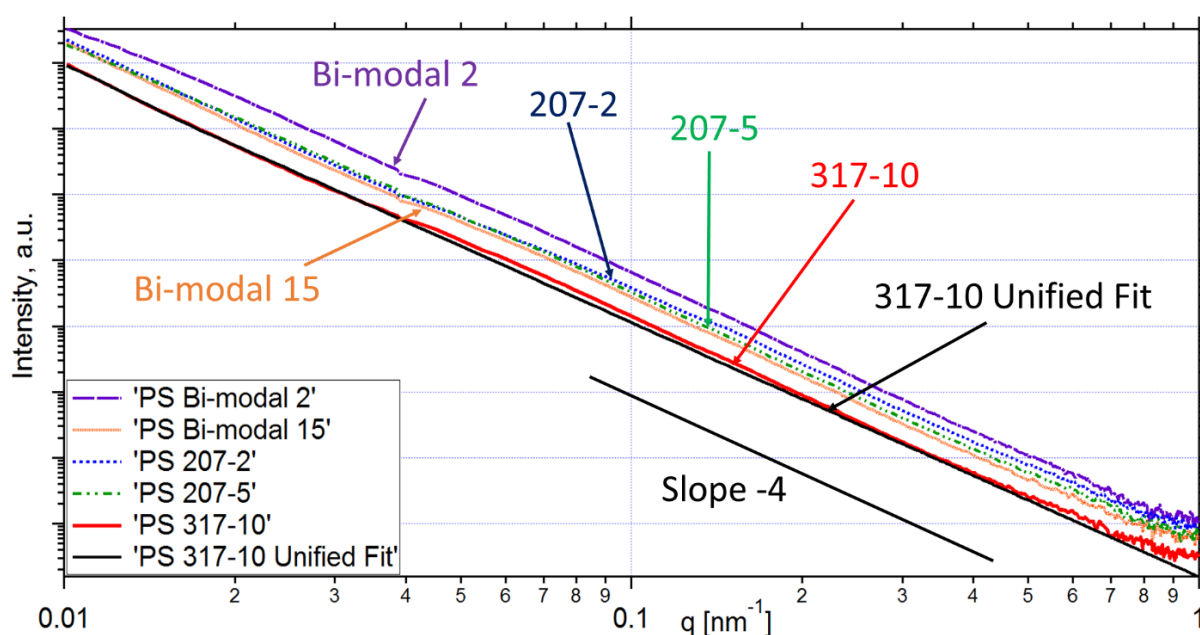


Figure 64: Representative SAXS patterns of polystyrene multi-voided particles, displayed in a double logarithmic format, acquired at the ID02 beamline (ERSF, Grenoble, France). The patterns were fitted using a one-level model of the unified approach⁷³ implemented in Irena SAS macros⁷⁴ for Igor Pro software. It was assumed for the model that, at high q , $I(q) \propto q^{-4}$. The solid black line shows a representative fit using the unified approach. The slope -4 line is given for guidance.

The polystyrene multi-voided particles are a typical two-phase polymer-air system having sharp distinct interfaces. The SAXS patterns produced by these particles obey the Porod's law at large q .

The approach illustrated in the characterisation section (Equation 36 - 41) was used to characterise the multi-voided particles, in order to estimate the surface area S_v and the average pore diameters l_p of the particles, along with the air volume fraction and the packing density of the samples.

Multiple scattering patterns for each sample were collected and independently analysed to estimate pores' surface areas and diameters, and the respective margins of error. The results of the SAXS analysis are displayed in Table 4.

The surface area of the polystyrene particles ranges from $5.40 \pm 0.09 \text{ m}^2 \text{ cm}^{-3}$ for the sample "23-2" with lowest molecular weight (23 kg mol⁻¹) and lowest polystyrene concentration in toluene (2% w/w), to $1.02 \pm 0.06 \text{ m}^2 \text{ cm}^{-3}$ for the sample "317-10" with the highest molecular weight (317 kg mol⁻¹) and the highest polystyrene concentration in toluene (10% w/w). The results of SAXS analysis have shown that the pore size l_p ranges from $476 \pm 8 \text{ nm}$ for "23-2" to $3286 \pm 181 \text{ nm}$ for "317-10" and the voids volume fraction ranges from 55 to 84%.

Table 4: Results of the SAXS data analysis: sample packing density (ρ_{sam}), air volume fraction (ϕ_p), interface surface area per unit volume (S_v) and pore chord length (l_p). The samples above C^* are indicated in bold.

Sample	Packing density $\rho_{sam} \text{ (g x cm}^{-3}\text{)}$	Air volume fraction $\phi_p / \%$	Surface area S_v $\text{(m}^2 \text{ x cm}^{-3}\text{)}$	Pore chord $l_p \text{ (nm)}$
23-2	0.382	64	5.40 ± 0.09	476 ± 8
23-5	0.483	55	4.40 ± 0.13	498 ± 15
23-7	0.383	64	4.89 ± 0.10	525 ± 10
23-10	0.388	64	4.77 ± 0.13	534 ± 14
23-15	0.416	61	4.52 ± 0.08	540 ± 9
207-2	0.323	70	2.53 ± 0.03	1105 ± 15
207-5	0.205	81	1.92 ± 0.15	1689 ± 130
207-7	0.299	72	2.42 ± 0.16	1192 ± 78
207-10	0.373	65	3.02 ± 0.26	867 ± 73
207-15	0.384	64	2.39 ± 0.15	1075 ± 68
317-2	0.440	59	4.20 ± 0.24	561 ± 33
317-5	0.301	72	2.65 ± 0.15	1085 ± 58
317-7	0.334	69	2.56 ± 0.20	1079 ± 82
317-10	0.173	84	1.02 ± 0.06	3286 ± 181
bi-modal 2	0.278	74	4.31 ± 0.05	686 ± 8
bi-modal 5	0.263	75	3.88 ± 0.25	780 ± 51
bi-modal 7	0.384	64	2.71 ± 0.03	947 ± 11
bi-modal 10	0.367	66	2.03 ± 0.18	1302 ± 121
bi-modal 15	0.424	60	2.50 ± 0.27	974 ± 110

For low molecular weight systems (23 kg mol^{-1} and bi-modal $53, 107 \text{ kg mol}^{-1}$) below the chain overlap concentration C^* , a correlation between the polymer concentration in the solvent and pore chord can be identified: an increase in concentration corresponds to an increase in the average diameters of the void domains and a reduction of the surface area.

In the systems with higher molecular weight (207 and 317 kg mol^{-1}) this trend is not observed, which is likely to the fact that the chain entanglement in these samples determines different dynamics in the phase separation processes.

CHARACTERISATION OF MULTI-VOIDED POLYSTYRENE PARTICLES BY SEM.

The structural morphology of the polystyrene multi-voided particles was also characterised by SEM, using either a Philips XL-20 instrument operating at a voltage of 15 kV or a Jeol JSM-6010LA instrument also operating at a voltage of 15 kV. The samples were fractured between microscope glass slides in order to image their cross-sections, representing the internal structural morphology. The samples were then coated with gold using an Edwards S150B sputter coater. In order to estimate the pore size distribution, the SEM images were analysed using the Image J⁶⁸ software (version 1.50d).

The particles display a spherical shape, as they were formed from spherical droplets of polystyrene solution, dispersed within the emulsion (Figure 65). The particles' size was comparable to the droplets' size measured by DLS.

The particles presented a smooth external skin with closed internal pores, the result of nucleation and growth processes during the phase separation. The internal morphology resembles the foam structure of the type existent in bird feathers. This morphology enables the particles to act as broad-band scatterers, producing white.

A distribution of pore size within the particles was observed, with smaller pores located in proximity of the external regions and a large cavity towards the centre (Figure 66). This pore distribution is a consequence of the phase separation mechanism that starts from the external regions of the droplets forming the particles' smooth skin. Since the surface is quickly frozen by the loss of solvent and less mobile than the central region, during the solvent loss polystyrene migrates from the centre to conserve density. This results in a large central cavity, as shown in the cross section of the sample "bi-modal 7" (Figure 66 c).

It should be noted that the two populations of pores observed by SEM were not considered in the SAXS analysis. However, we expect that the effect of these large cavities on the surface area derived from modelling the SAXS should be small. Assuming that the diameter of cavities is about 20 times larger than the diameter of small pores and that the volume fraction of both the cavities and the small pores is equal, the cavities would contribute only $\approx 5\%$ of the total surface area corresponding to these two populations.

The particles produced by systems with significantly higher molecular weight (317 kg mol^{-1}) and concentration above C^* , exhibited a different morphology, characterised by a considerably larger central cavity contained within a relatively thin porous shell. This type of structure is clearly observable in the "317-10" sample (Figure 66 h), where the cross section of the sphere reveals a

large empty volume, encompassed within a thin layer of polystyrene. The porosity observed within the thin shell of this particle, presenting a morphology that resembles an open porous network, is possibly produced by spinodal decomposition. A representative selection of the particles produced employing the NIPS emulsion process is shown in Figure 66.

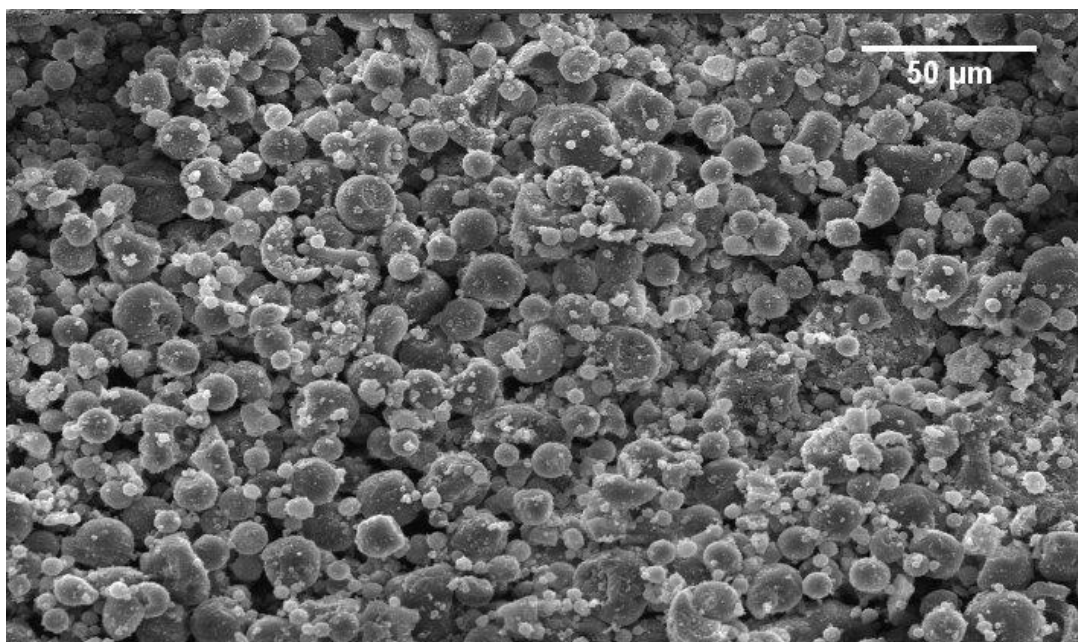
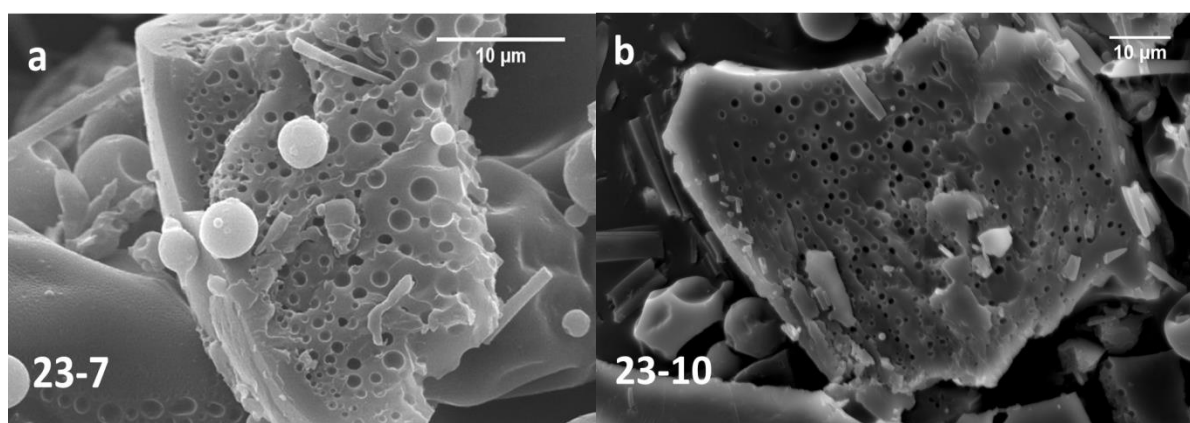


Figure 65: A representative SEM image of the polystyrene particles produced with the NIPS emulsion process, with PS M_w of 23 kg mol^{-1} and polystyrene concentration of 2% w/w in the initial polymer solution. The particles present a spherical shape, as they retain the shape of the emulsion droplets from which they were formed. There is a distribution of particles size, with the larger particles having diameters $\approx 30 \mu\text{m}$. The particles' size is comparable to the droplets' size of the emulsion measured by DLS, Table 3.



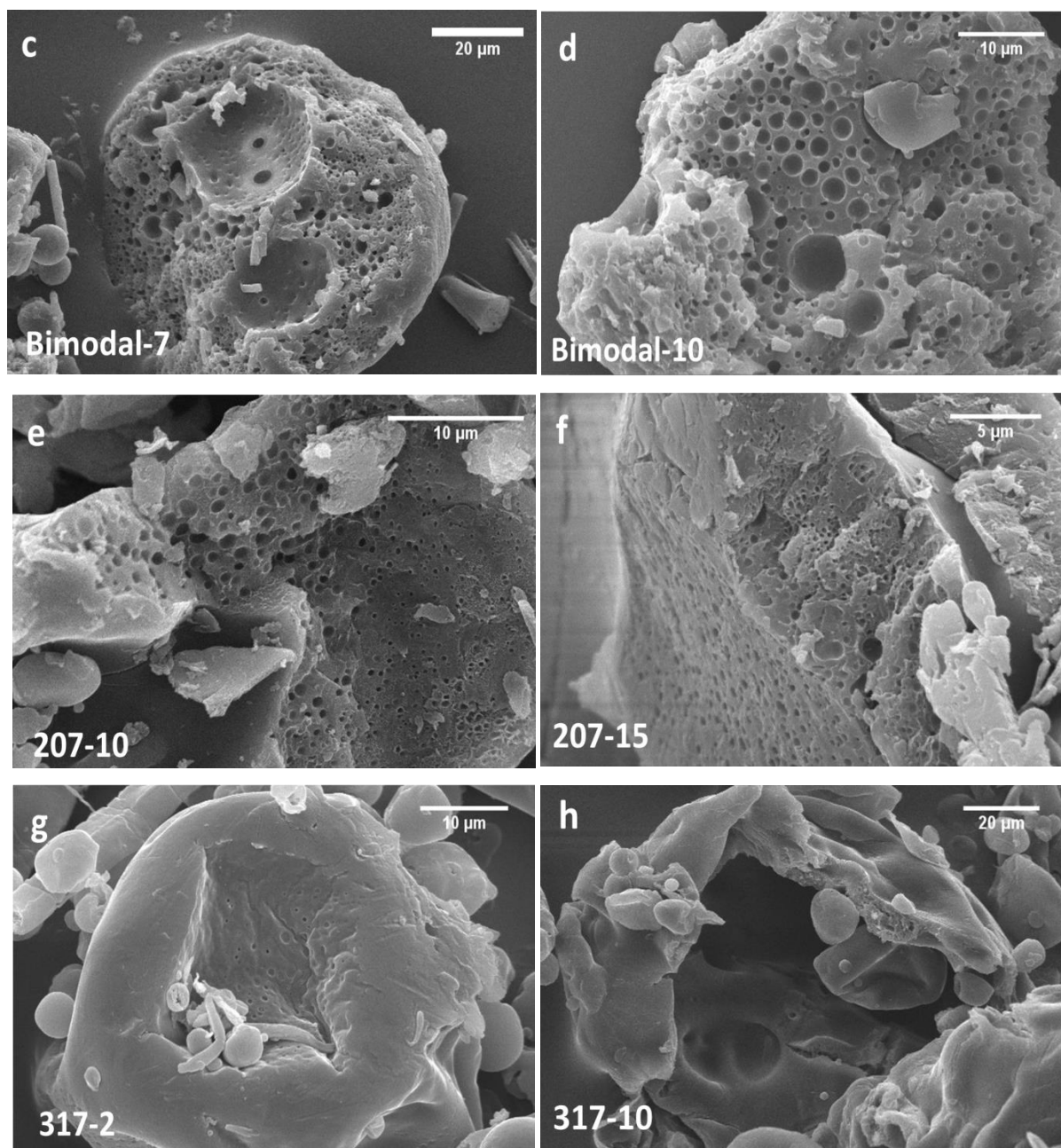
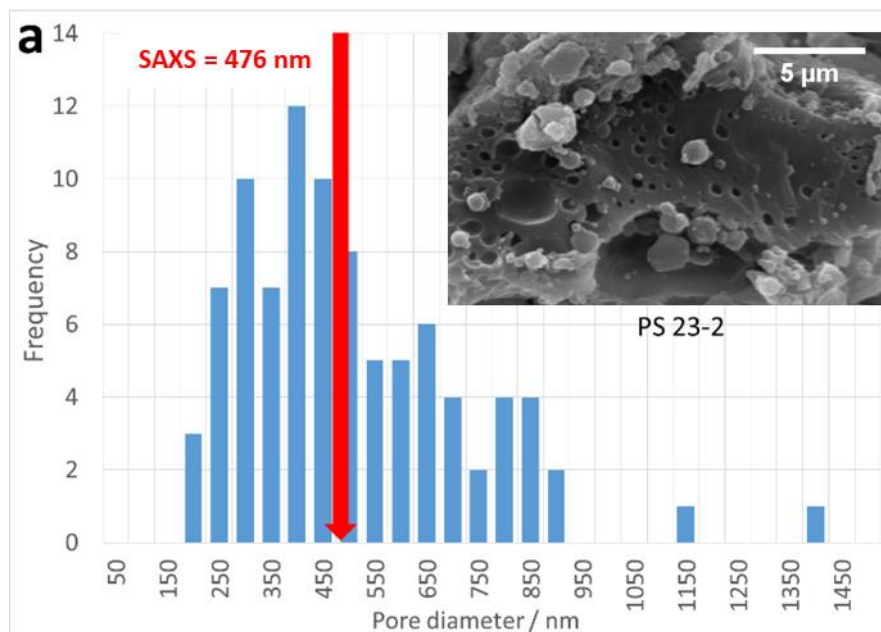


Figure 66: Representative SEM images of the particles produced by the NIPS emulsion process. The cross-sections of fractured particles was imaged. (a) PS M_w of 23 kg mol^{-1} and PS concentration of 7% w/w; (b) PS M_w of 23 kg mol^{-1} and PS concentration of 10% w/w; (c) PS bi-modal and PS concentration of 7% w/w; (d) PS bi-modal and PS concentration of 10% w/w; (e) PS M_w of 207 kg mol^{-1} and PS concentration of 10% w/w; (f) PS M_w of 207 kg mol^{-1} and PS concentration of 15% w/w; (g) PS M_w of 317 kg mol^{-1} and PS concentration of 2% w/w; (h) PS M_w of 317 kg mol^{-1} and PS concentration of 10% w/w. In image (c) the large central cavities are clearly observable. In image (h) a large empty volume, encompassed within a thin layer of polystyrene, is present: the thin shell exhibits an internal structure that recalls an open porous network, perhaps result of spinodal decomposition. All the other samples present non interconnected closed pores, produced by a nucleation and growth mechanism of the phase separation.

In order to estimate the pore size distribution within the samples and to compare the information obtained by SEM with the values for the average void size measured by SAXS, Table 4, the images were processed using Image J⁶⁸ software. The images selected were close-ups of the external regions of the particles, where most of the porosity was observed.

This analysis presented several limitations. Firstly, only small areas of the particles were considered: therefore, the images may not be representative of the entire sample. The image processing relied on the ability of the software to discriminate between pores (dark areas) and polymeric structure (light areas) by chromatic contrast. However, when this contrast is not particularly sharp, errors in determining pore size may be introduced. The assumption that pores were perfectly spherical was made and pore diameters were calculated from the area of the two-dimensional circular cross-sections. When a particle is fractured, spherical pores may be randomly cut at any section of the pore. Since the probability to be sliced in two perfect hemispheres is low, it is very likely that the almost entirety of the observed pores in the SEM images presented a diameter smaller than the true diameter of the void.

Despite the number of assumptions listed above, the pore size distributions of most of the samples estimated by this method was in a reasonably good agreement with the averaged void size obtained by SAXS analysis. The SAXS values fall within the pore-size distributions estimated by SEM, supporting the accuracy and complementary of the two different structural characterisation techniques.



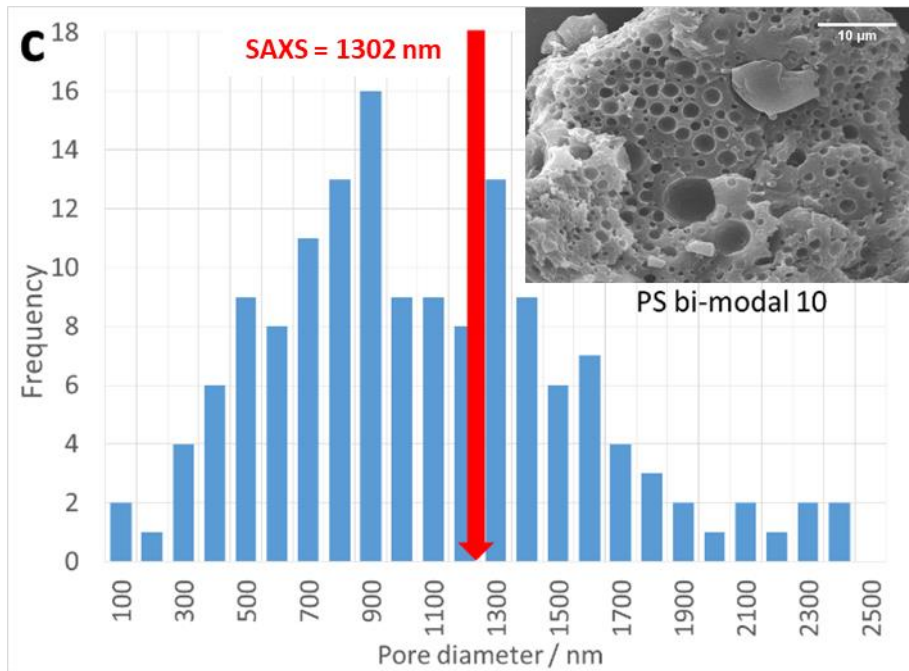
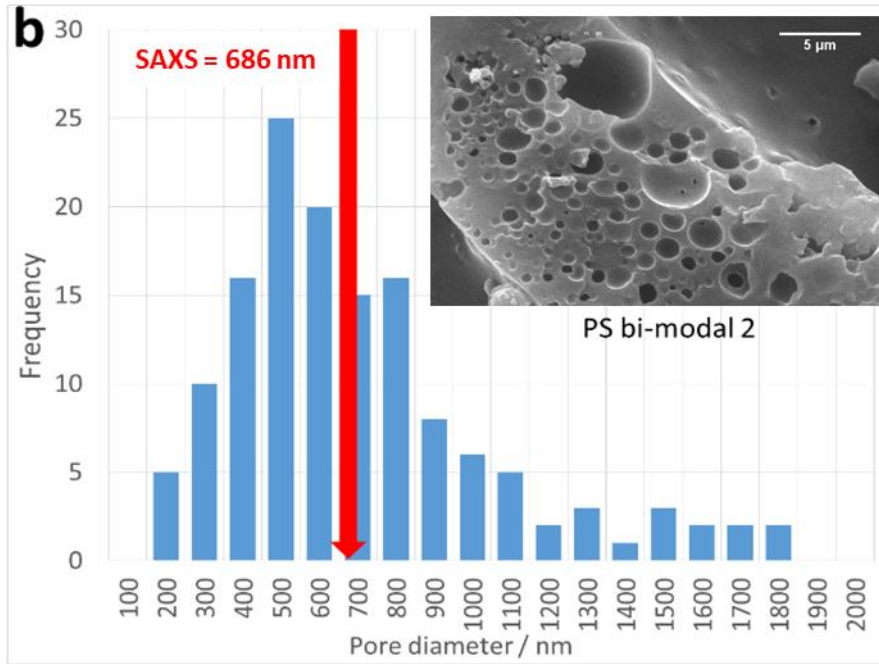


Figure 67: A selection of histograms of the number of air voids versus their diameter, showing pore size distributions obtained from 2D SEM images of cross-section regions of the fractured samples “23-2” (a), “bi-modal 2” (b) and “bi-modal 10” (c). In the top corner of each diagram a representative SEM image that generated the distribution is shown. The vertical red arrows indicate the average size of the voids calculated by SAXS.

CORRELATIONS BETWEEN POLYMER CONCENTRATION OF POLYSTYRENE–TOLUENE SOLUTIONS AND STRUCTURAL MORPHOLOGY OF THE PARTICLES.

Analysis of the structural information on particles' pore size obtained by SAXS measurements and supported by SEM imaging, together with the polymer concentration of the polystyrene-toluene systems, has shown a strong correlation between these parameters (Figure 68). It was found that there is a linear dependence between $1/\text{pore diameter}$ and *polystyrene concentration* for the systems below C^* .

The linear trend is clearly observed for the 23 kg mol^{-1} and for the bi-modal polystyrene systems where most of the polymer solutions have concentrations below C^* .

The samples that deviate from the linear trend are the samples prepared from 15% w/w polystyrene solutions. These are above C^* , where polymer chain entanglement takes place. For the systems with concentrations above C^* , the proportionality relationship is no longer observed. The data points are scattered across the plot without an obvious trend.

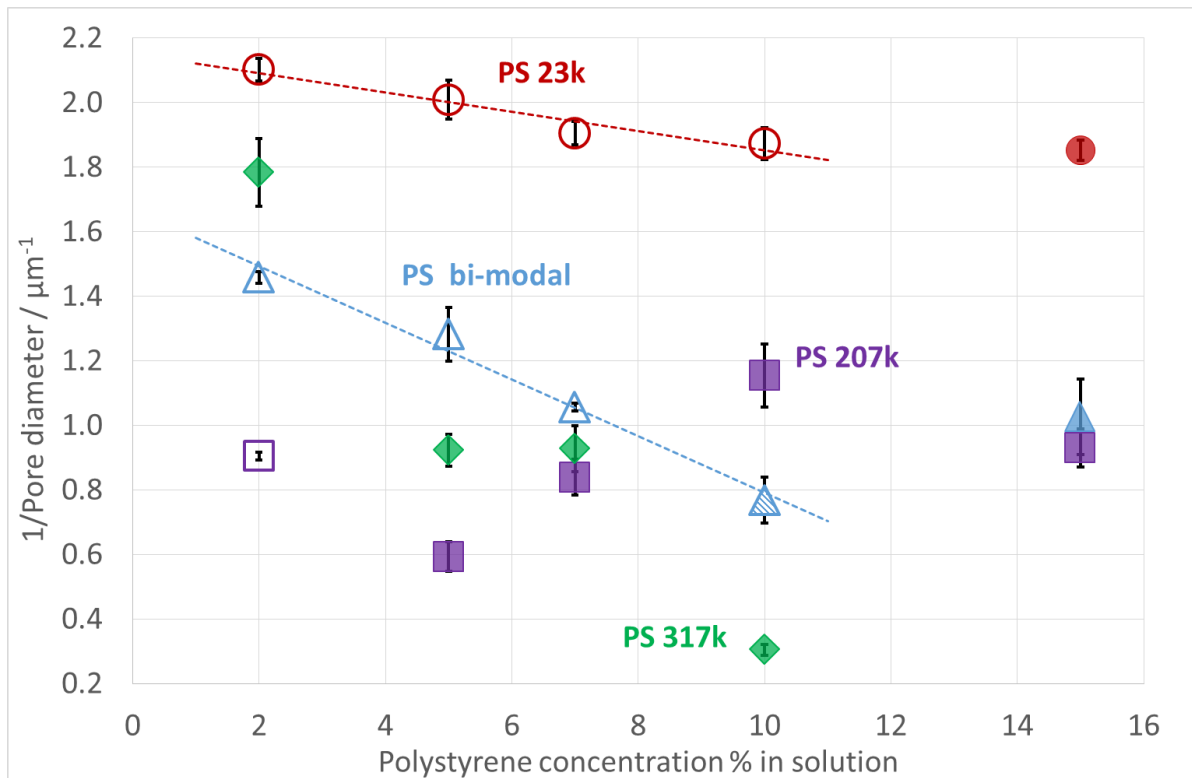


Figure 68: $1/\text{pore diameter}$ vs polystyrene concentration in polymer solutions plot for the 23 kg mol^{-1} (circles), bi-modal $53, 107 \text{ kg mol}^{-1}$ (triangles), 207 kg mol^{-1} (squares) and 317 kg mol^{-1} (diamonds) polystyrene systems. The open symbols correspond to samples obtained from polystyrene-toluene solutions with polymer concentrations below C^* where the phase separation is thermodynamically controlled. Solid symbols represent polystyrene-toluene solutions with concentration above C^* , where the phase separation is kinetically controlled. The pattern-filled symbol for “bi-modal 10” shows that only the long chains of the bi-modal sample are above C^* . The diagram clearly highlights a linear correlation between $1/\text{pore diameter}$ and polystyrene concentration when $C < C^*$ in the 23 kg mol^{-1} and in the bi-modal systems. The correlation is no longer observable for 207 kg mol^{-1} and 317 kg mol^{-1} where $C > C^*$. The error bars show the margins of error for pores’ diameters.

Since the viscosity of the polymer solutions used to fabricate the particles is proportional to the concentration of polystyrene in solution, an analogous linear trend is also observable between the zero-shear viscosity η_0 of the polystyrene solutions and $1/\text{pore diameter}$ when $C < C^*$ (Figure 69).

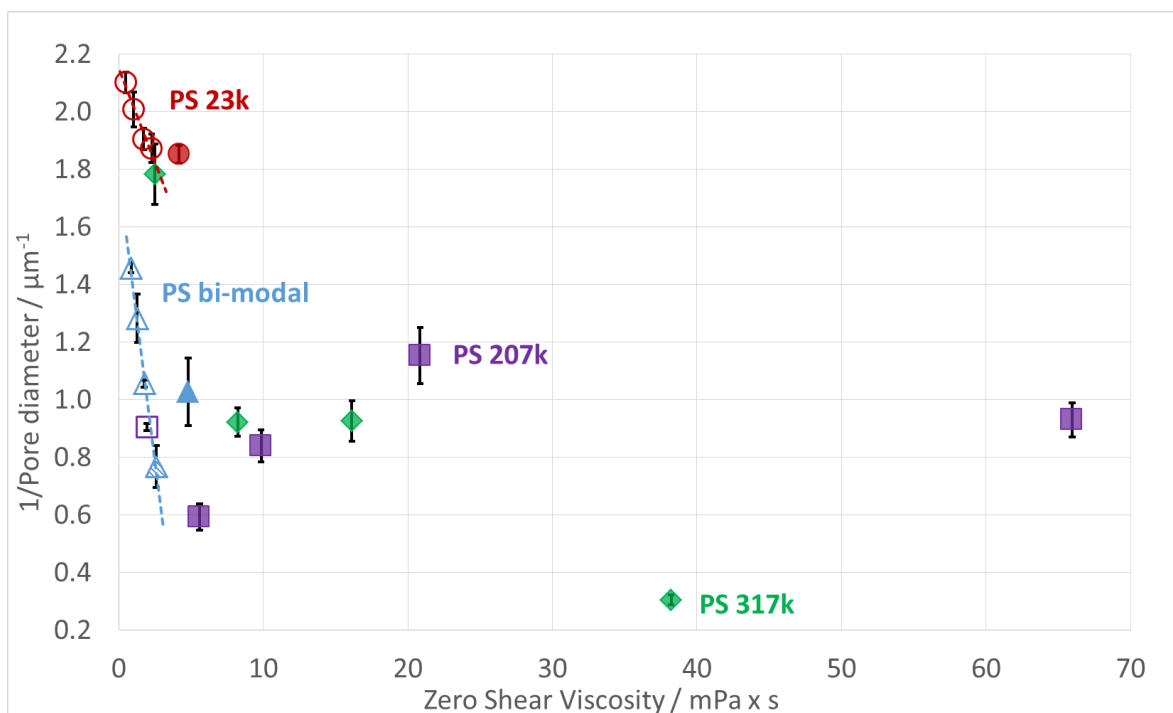


Figure 69: $1/\text{pore diameter}$ vs zero-shear viscosity η_0 plot for the 23 kg mol^{-1} (circles), bi-modal $53, 107 \text{ kg mol}^{-1}$ (triangles), 207 kg mol^{-1} (squares) and 317 kg mol^{-1} (diamonds) polystyrene systems. The open symbols correspond to samples obtained from polystyrene-toluene solutions with polymer concentrations below C^* , solid symbols represent polystyrene-toluene solutions with concentration above C^* , where the phase separation is kinetically controlled. The pattern-filled symbol for “bi-modal 10” shows that only the long chains of the bi-modal sample are above C^* . The diagram clearly highlights a linear correlation between $1/\text{pore diameter}$ and zero-shear viscosity η_0 when $C < C^*$ in the 23 kg mol^{-1} and in the bi-modal systems. The correlation is no longer observable for 207 kg mol^{-1} and 317 kg mol^{-1} where $C > C^*$. The error bars show the margins of error for pores’ diameters.

The observed reciprocal relationship between the *polymer concentration* and $1/\text{pore diameter}$, for polystyrene-toluene-ethanol systems when the concentration of the system is lower than the critical chain overlap concentration C^* , may have a practical application and could be used to produce porous polystyrene micro-spheres with “tunable” voids size.

Moreover, the reciprocal correlation between *pore diameter* and *zero shear viscosity* demonstrated in this study could be used as a relatively simple tool to control the properties of the polystyrene-toluene-ethanol systems.

It could be predicted that when the glass transition temperature of the polymer intersects the temperature of the system upon the addition of the non-solvent, the phase separation arrests⁴⁴ and the morphology achieved at this stage is fixed. Since the glass transition temperature of a polymer in solution increases with increasing polymer concentration,⁷⁹ a polymer solution at high concentration of polystyrene is expected to intersect the temperature of the system in a shorter interval of time

than a solution at low concentration of polystyrene. As a consequence, in a high concentration solution, phase separation would arrest earlier and produce pores of smaller size than in a low concentration solution. For systems with a fixed pore nucleation density, it would be expected to observe smaller pores (and consequently smaller surface area) in particles generated with high concentration solutions, and progressively larger pores (and larger surface area) in particles generated with low concentration solutions.

This trend of “high concentration - small pores” is observed in polycarbonate in chloroform⁵¹ where increasing the polymer concentration produced monoliths with smaller pores.

However, the results obtained in the current study demonstrate the opposite trend, where polystyrene solutions with increasingly higher concentrations produced porous particles with increasingly larger pores (Figure 68). The glass transition behaviour alone is insufficient to justify the trend, but a deeper analysis of the phase diagram provides further insights about the processes taking place in these ternary systems, which could be helpful for the interpretation of the results.

A section of the ternary phase diagram (Figure 61) can be enlarged to highlight the region of interest (Figure 70). As a representative example, the behaviour of only two polymer systems corresponding to M_w 23 kg mol⁻¹ and the bi-modal polystyrene at the initial polymer concentrations of 2% and 7% w/w are considered. In this case, the starting conditions of the samples (polystyrene in toluene solutions plotted on the polystyrene-toluene axis, represented as triangles), the final non-solvent conditions reached upon ethanol addition (squares) and the transition from the one-phase to the two-phase region (arrows) are clearly represented, along with the binodal boundaries.

The phase separation starts on crossing the binodal line: for the bi-modal systems, this occurs in point *A* for the bi-modal-7 and in point *C* for the bi-modal-2. Similarly it takes place in point *B* for the 23-7 sample and in point *D* for the 23-2.

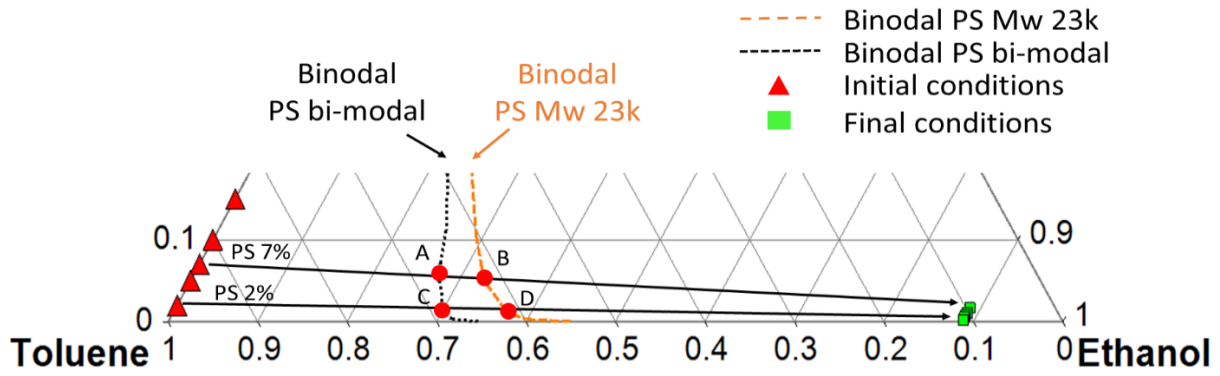


Figure 70: A section of the ternary phase diagram of Figure 61. The initial conditions are represented by the red triangles on the toluene-polystyrene axis (left side of the diagram). The final conditions are represented by the green squares. The binodal boundaries for the bi-modal and the 23 Kg mol⁻¹ polystyrene are shown by dotted lines. The arrows represent the transition of the systems with initial polystyrene concentrations of 2% and 7% w/w from the one-phase to the two-phase region. The points A and C mark the starting points of phase separation of the bi-modal samples. The points B and D mark the starting points of phase separation for the 23k samples.

The composition of the systems at these points is reported in Table 5 in the form of weight percentage of polystyrene, toluene and ethanol. The ratio of non-solvent to solvent (ethanol to toluene, ϕ_3/ϕ_1) is higher for low concentration polymer solutions [ϕ_3/ϕ_1 (C) > ϕ_3/ϕ_1 (A) and ϕ_3/ϕ_1 (D) > ϕ_3/ϕ_1 (B)]. At the same initial concentration, the solutions with lower molecular weight show a higher ethanol to toluene ratio [ϕ_3/ϕ_1 (B) > ϕ_3/ϕ_1 (A) and ϕ_3/ϕ_1 (D) > ϕ_3/ϕ_1 (C)].

Table 5: Composition of the systems at the points A, B, C and D (Figure 70) expressed in polystyrene, toluene and ethanol weight percentage. Ethanol to Toluene ratio (ϕ_3/ϕ_1), surface area of the particles generated by using these polymer solutions and the average pore diameters are also shown.

Sample	Point	PS wt%	Tol wt%	EtOH wt%	ϕ_3/ϕ_1	Surface Area (m ² x cm ⁻³)	Pore size (nm)
bi-modal 7	A	0.051	0.672	0.277	0.41	2.71 ± 0.03	947 ± 11
23-7	B	0.047	0.621	0.332	0.53	4.89 ± 0.10	525 ± 10
bi-modal 2	C	0.014	0.688	0.298	0.43	4.31 ± 0.05	686 ± 8
23-2	D	0.012	0.616	0.372	0.60	5.40 ± 0.09	476 ± 8

It could be concluded that a greater amount of non-solvent present in the system at the beginning of the phase separation process, induces phase separation in a larger number of sites within the emulsion droplets: this results in a larger number of smaller pores, in the particles generated by systems with higher ethanol to toluene ratio (Figure 71). This hypothesis is supported by SAXS results obtained for the particles surface area S_v : larger ϕ_3/ϕ_1 corresponds to larger S_v , suggesting

that a larger number of voids is present within these particles. Samples with larger surface area have voids with smaller average diameters. The ternary diagram (Figure 70) suggests that the relative concentration of ethanol non-solvent at the point of phase separation reduces either with the increase of polystyrene concentration or with the increase of polymer molecular weight. Thus, it should be expected that the pore surface area has to be increased (and, consequently, the pore size has to be reduced) either by reducing the molecular weight at a constant concentration of polymer (Table 5, compare samples bi-modal 2 and 23-2 or bi-modal 7 and 23-7) or by decreasing the polymer concentration for the same molecular weight (Table 5, compare samples 23-2 and 23-7 or bi-modal 2 and bi-modal 7). It has to be noted that this conclusion is only valid for the porous particles obtained from solutions with polymer concentrations below C^* .

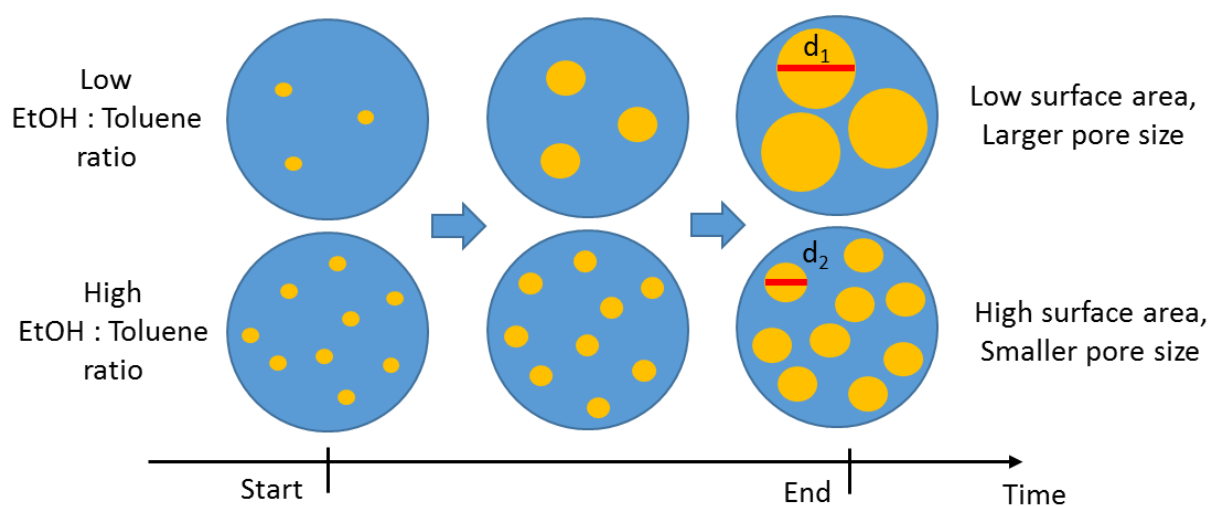


Figure 71: The relative amount of ethanol non-solvent at the start of the phase separation determines the pore density within the particles, affecting pore size and pore surface area. High ethanol to toluene ratio induces more nucleation sites in the polymer solution droplets, resulting in a larger number of pores with smaller diameters ($d_2 < d_1$) in the particles. This conclusion is supported by SAXS results, showing larger surface area and smaller average pore size for particles generated from systems with high ethanol to toluene ratio. The pore size can be reduced and, consequently, the pore surface area can be increased, either by reducing polymer concentration in the initial solution, or by decreasing polymer molecular weight in the sample composition.

CHAPTER 7: NIPS BY EMULSION SCALE UP.

The NIPS by emulsion process proved to be a successful method to produce polystyrene multi-voided particles with the desired structural features. It was finally possible to obtain particles with a spherical shape in the desired size range of $\approx 10 - 50 \mu\text{m}$ (Figure 65). It was possible to achieve particles with a closed external surface and an internal porous structure, mimicking the foam structure of *Garrulus glandarius's* feathers (Figure 66). The reciprocal relationship between the *polymer concentration* and the *pore diameter* could be exploited in order to select the right initial conditions, in terms of polymer molecular weight and polymer concentration, to obtain particles with the desired pore size. And, most important, the NIPS by emulsion is a scalable process, which finally provided the opportunity to produce enough particles to be implemented in the paint formulations supplied by the industrial partner AkzoNobel®. It was now possible to assess the scattering power of the polystyrene multi-voided particles and to compare their performance with that of titanium dioxide (the main white pigment used in the paint industry) and one of the main extenders, Ropaque⁸⁰ (an organic extender, produced by the Dow Chemical Company, Michigan, United States. Ropaque is a polystyrene particle with a single air-filled cavity, which also exploits the difference in refractive index Δn between polymer and air to achieve light scattering).

Studies of the biological structures, analysed in the structural colour chapter, highlighted that the *Cyphochilus* beetle achieves structural white with pores having average diameters of $580 \pm 120 \text{ nm}$ and an air-volume fraction of 40 - 50%.³² Models based on the beetles' structures suggested that an ideal system should have pores with average diameters of 500 nm.³² The white sections of the Jay feathers showed that structural white is achieved in those systems when the air-filled voids have size larger than 200 nm and present a broad size distribution.³⁸

The SAXS analysis of polystyrene multi-voided particles (Table 4) showed that systems capable of producing porous structures with features comparable to the biological target structures were those with low M_w polystyrene (23 kg mol^{-1}), with an average pore size in the range of $\approx 476 - 540 \text{ nm}$ and an air volume fraction range of $\approx 55 - 65 \%$. The conditions that produced an average pore size ($498 \pm 15 \text{ nm}$) closest to the pore size of an ideal system (500 nm) were achieved with PS M_w 23 kg mol^{-1} and PS concentration in the initial polymer solution of 5% w/w (Table 4). Therefore these were the conditions selected for the scale up of the NIPS process by emulsion.

The experimental work took place in the AkzoNobel® Research & Development site (Slough, UK). The R&D facilities provided the necessary equipment and support to work with larger volumes of solvent

and, most importantly, the materials and the technical expertise to produce prototypes of paint formulations and to measure the scattering power of the paint films.

Due to the strict health and safety requirements in the AkzoNobel® laboratories, toluene solvent and ethanol non-solvent had to be replaced with the less harmful equivalents, xylene and isopropanol (IPA) respectively (Figure 72).

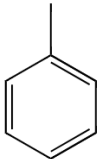
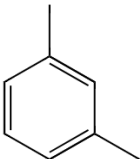
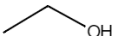
Solvents		Non solvents	
Toluene	Xylene	Ethanol	Isopropanol
			

Figure 72: Replacement materials for the scale up of the NIPS by emulsion process in the AkzoNobel® laboratories. Toluene and ethanol were replaced with the less harmful equivalents xylene and isopropanol, respectively.

In order to establish that this slight modification of the ternary system did not alter the structural morphology of the polystyrene particles, a trial experiment was performed in Sheffield and the products were screened by SEM (Figure 73).

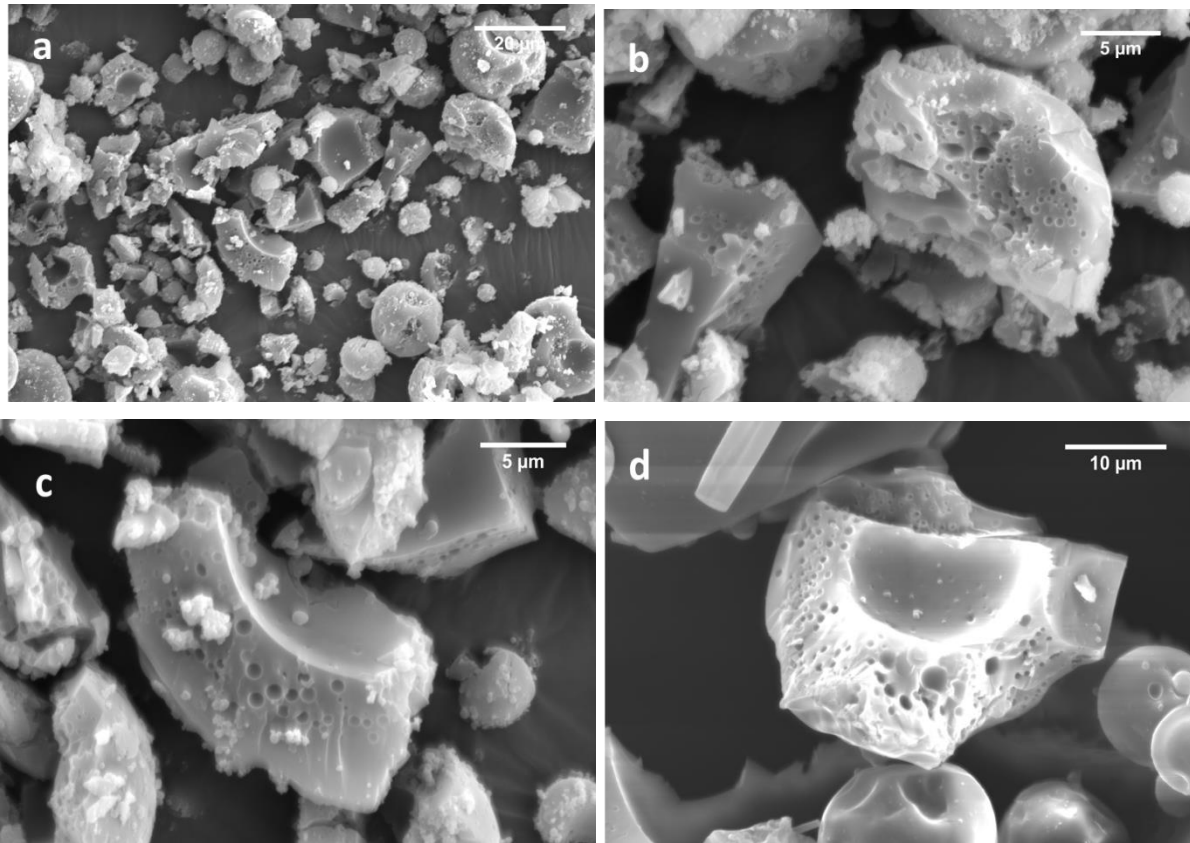


Figure 73 a-d: SEM images of the polystyrene multi-voided particles produced in research laboratory conditions with the modified ternary system, including polystyrene M_w 23 kg mol^{-1} and PS concentration of 5% w/w, xylene and isopropanol. (a) An overview of the particles: shape and size are equivalent to those of the particles achieved with the toluene-ethanol system. (b) (c) and (d) cross-sections of the fractured particles, displaying closed pores produced by a mechanism of phase separation by nucleation and growth. The porosity is equivalent to that achieved by the toluene-ethanol system.

The SEM assessment showed that the particles' shape and size, and the morphology of the porous regions, were equivalent to those of the particles produced with the toluene-ethanol system.

Image J processing of the SEM images showed that the porosity observed was in the expected size range (Figure 74) with the majority of pores having diameters of $\approx 450 - 500 \text{ nm}$ and a broad-size distribution, ideal for achieving white.

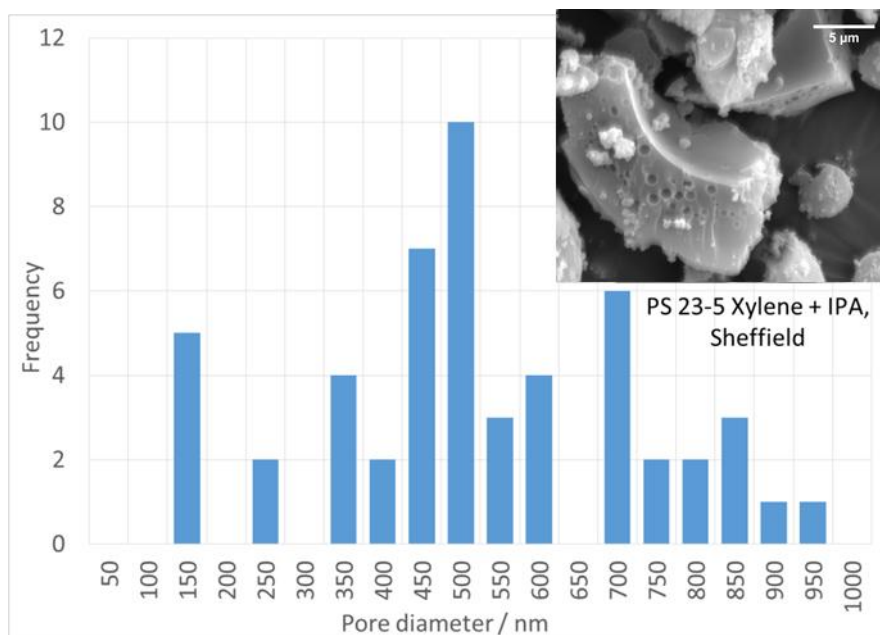


Figure 74: Image J analysis of a cross-section of a particle produced with the modified ternary system, PS M_w 23 kg mol⁻¹ at 5% w/w, xylene and isopropanol. The histogram shows the pore size distribution with a peak at \approx 450 – 500 nm and a broad size distribution ideal for structural white. In the top corner the SEM image that generated the distribution.

The polystyrene used for the scale up of the NIPS process was synthesised by the AkzoNobel® industrial plant. The GPC report, provided by the Material Characterisation Section in Slough, showed that the polystyrene samples delivered to the AkzoNobel® R&D laboratories had a M_w of 25055 g mol⁻¹ (approximated to 25 kg mol⁻¹) with a polydispersity index of 1.72 and a M_w of 25097 g mol⁻¹ with a polydispersity index of 1.77. These were very close to the polystyrene used in Sheffield, with M_w of 23092 g mol⁻¹ (approximated to 23 kg mol⁻¹) with a polydispersity index of 1.24, purchased from Polymer Source (Lot. Number P9397-S).

The polystyrene samples were delivered in the form of polystyrene solutions in xylene, with a concentration of 40% by weight. Xylene solvent and isopropanol non-solvent were also provided by the plant in Slough. Span 80 non-ionic surfactant was purchased from Sigma Aldrich, while deionised water was obtained from a Millipore water purifier.

The aim of the scale up of the NIPS process was the fabrication of \approx 60 g of polystyrene multi-voided particles. This required the use of 150 g of the polystyrene solutions provided (with a PS concentration of 40% by weight) diluted with an extra 1050 g of xylene solvent, in order to reduce the polystyrene concentration to the 5% by weight required. The amounts of 24 g of span 80 non-ionic surfactant and of 3000 g of deionised water were added, in order to produce \approx 4200 g of emulsion. The emulsion was then delivered to 42 kg of isopropanol non-solvent (1 to 10 ratio). The

polystyrene multi-voided particles were isolated by filtration and left to dry to remove any residual solvent.

The high volume of solvents required for the process demanded the set-up of a specific apparatus, capable of transferring large amounts of emulsion to the coagulation bath of isopropanol, and then to transfer large volumes of the emulsion–isopropanol mixture to a filtration system, for the isolation of the polystyrene particles.

The 4.2 kg emulsion was prepared in a large beaker and mixed using an overhead stirrer. The beaker with the emulsion was then placed on a scale and connected to the delivery system illustrated in Figure 75.

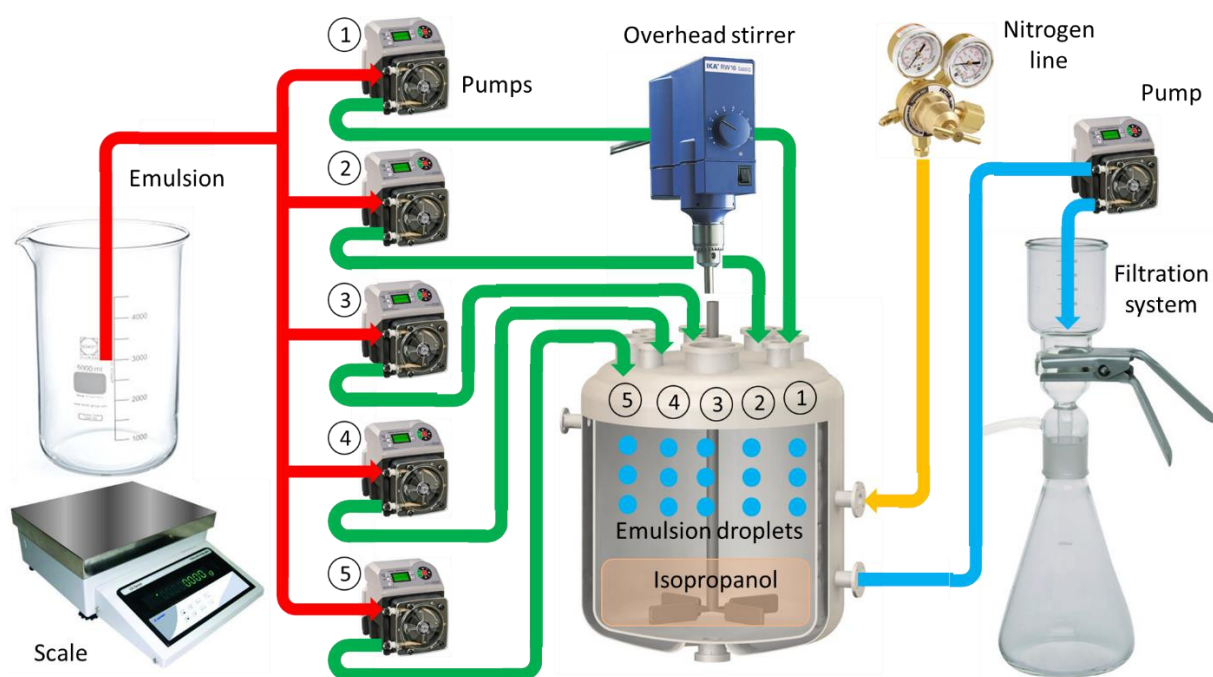


Figure 75: A sketch of the delivery system used to transfer the emulsion to the coagulation bath (isopropanol) in the vessel, and to transfer the coagulation mixture from the vessel to a filtration system for the isolation of the polystyrene particles. The emulsion was prepared in a large beaker and placed on a scale. The emulsion reservoir was connected to the inlets of five Watson-Marlow peristaltic pumps by a series of silicon tubes (red lines). The outlets of the five peristaltic pumps were connected to a second series of tubes (green lines), with the other end fixed to the inlets of a sealed vessel containing the coagulation bath of isopropanol. The sealed vessel was simultaneously connected to an overhead mixer to stir the isopropanol bath, to a nitrogen line (yellow) in order to keep a nitrogen atmosphere inside the vessel and reduce the risk of solvent ignition, and to a larger peristaltic pump (blue line). This final pump delivered the coagulation mixture to a vacuum filtration system, in order to isolate the polystyrene multi-voided particles.

The delivery apparatus consisted of five peristaltic pumps, connected to the emulsion reservoir by a system of silicon tubes. The outlet of each peristaltic pump was connected to a second series of

silicon tubes, with the other end fixed to the inlets of a sealed vessel containing the coagulation bath of isopropanol. The bath was continuously stirred using an overhead mixer. The activation of the peristaltic pumps allowed the transfer of the emulsion, through the five lines of tubes, from the reservoir beaker to the coagulation bath vessel (Figure 75). The vessel had a capacity of ≈ 6 litres, therefore the delivery of the emulsion could not be completed in a single cycle. The amount of 4.0 kg of isopropanol was placed in the vessel, the overhead stirrer was activated and a nitrogen line connected to the sealed vessel was opened. The beaker with the emulsion was placed on the scale and the pumps activated: since the ratio of emulsion to non-solvent is 1 to 10 by weight, when the scale indicated that 400 g of emulsion were delivered, the pumps were paused and the emulsion flow interrupted.

At this stage the polystyrene multi-voided particles produced were precipitated in the coagulation bath: a larger peristaltic pump connected to the vessel delivered the mixture to a vacuum filtration apparatus in order to isolate the particles. The empty vessel was then refilled with another 4.0 kg of isopropanol and a second cycle was started. The full delivery of the 4.2 kg of emulsion to the 42 kg of isopropanol required a total of eleven cycles. The final yield of polystyrene multi-voided particles was 51.4 g, out of the theoretical 60 g, with a yield percentage of 85.6%. This amount was sufficient for the incorporation into paint formulations and for SEM screening.

The particles produced with the scaled up NIPS process were characterised by SEM and SAXS, in order to establish that the upgrade of the fabrication process still preserved the porous internal structure. A selection of SEM images of the cross-sections of the fractured particles showed that the internal structure was consistent with the expectations. Spherical particles in the desired size range, with a closed external surface and closed spherical pores, produced by nucleation and growth of the solvent-rich phase, were achieved (Figure 76).

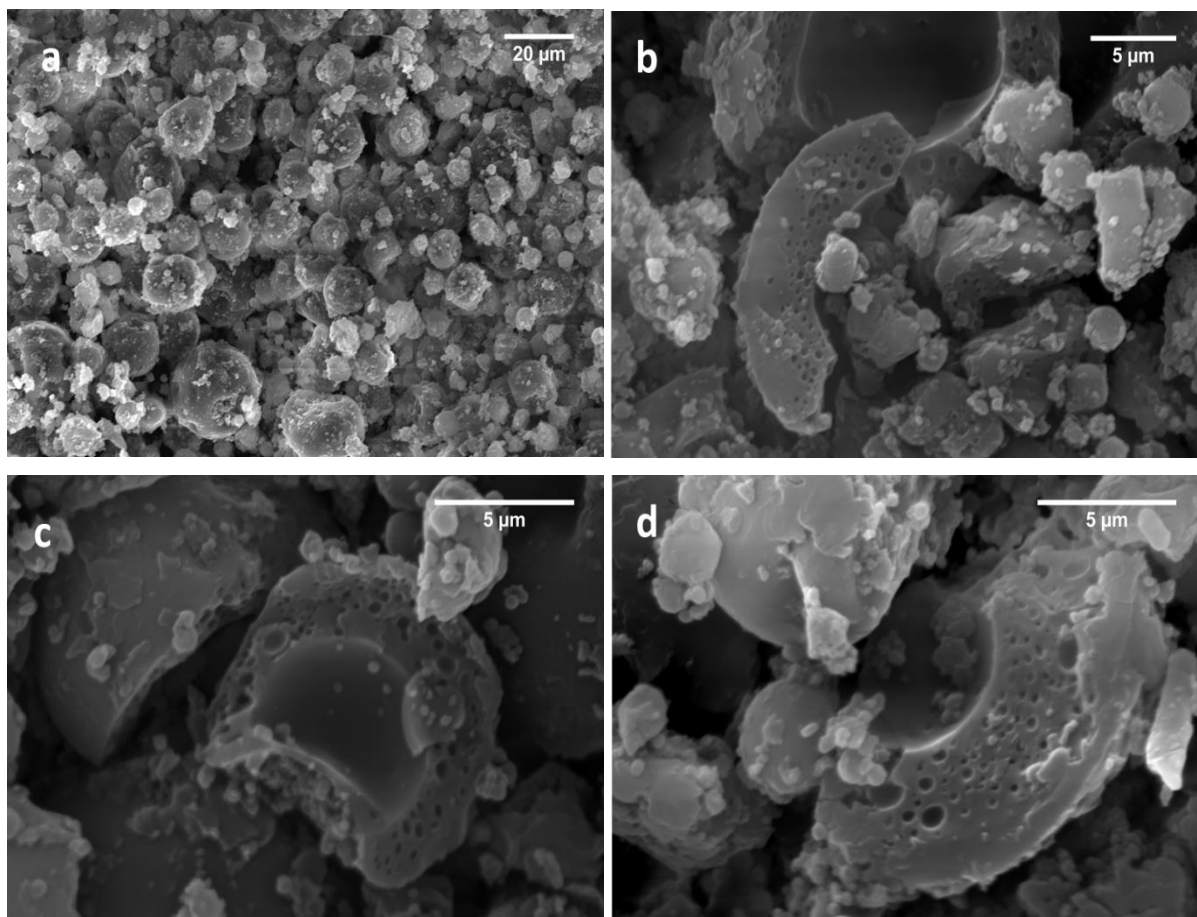


Figure 76: SEM images of the polystyrene multi-voided particles produced with the scaled up NIPS process using AkzoNobel® facilities. The ternary system included polystyrene M_w 25 kg mol⁻¹ at 5% w/w concentration, xylene and isopropanol. (a) An overview of the particles, displaying spherical shapes and size in the 10 – 50 μm range. (b) (c) and (d) Cross-sections of the fractured particles, displaying closed pores produced by a mechanism of phase separation by nucleation and growth of the solvent-rich phase.

Image J processing showed that the porosity observed was in line with the expectations, with a peak around 450 nm and a broad-size distribution (Figure 77), consistent with the light scattering needed for structural white. SAXS analysis, performed at the ESRF at the beamline ID02, estimated an average pore size of 524 nm.

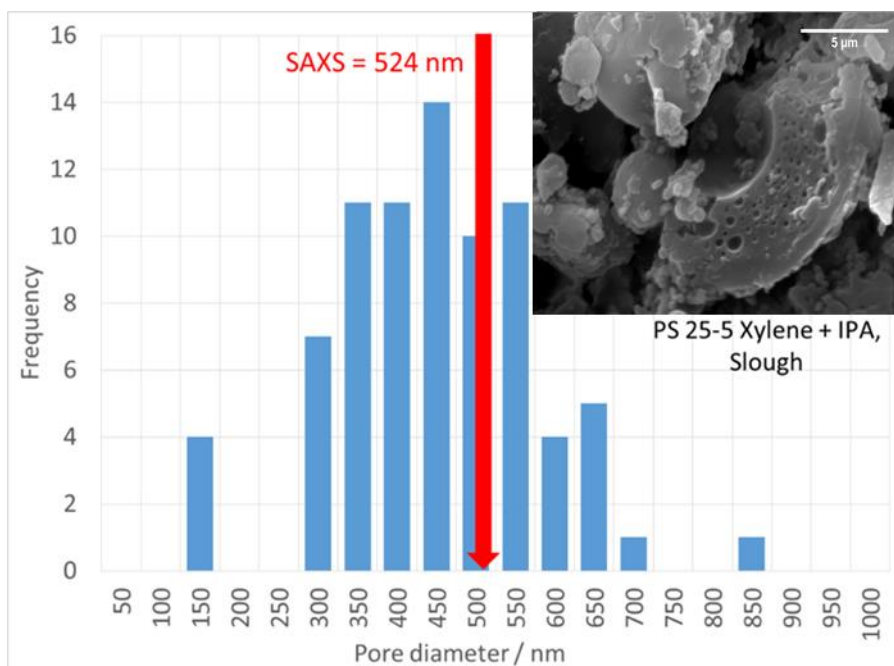


Figure 77: Image J analysis of a cross-section of a particle produced with the scaled up NIPS process. The histogram shows the pore size distribution with a peak around 450 nm and a broad size distribution needed for structural white. In the top corner the SEM image that generated the distribution. The vertical red arrow indicates the average size of the voids calculated by SAXS.

The next step required the incorporation of the polystyrene multi-voided particles into the paint formulation prototypes, prepared in the AkzoNobel® laboratories.

All the formulations sheared the following ingredients: water, Acrysol X935-60 (binder-thickener), Mirecide ON37 (antibacteria), Dispelair CF246 (anti-foam), Disponil A1580 (non-ionic surfactant), Bermocoll EBM solution (non-ionic surfactant) and Dispex N40 (dispersing agent). The opacifying materials titanium dioxide (in the form of a slurry), Ropaque Ultra E and the polystyrene NIPS multi-voided particles newly produced, were added in specific amounts, as illustrated in Table 6.

The formulations have been divided in three main groups according to the levels of TiO_2 and labelled α -group (0 % TiO_2), β -group (2 % TiO_2) and γ -group (4 % TiO_2). The values of PVC (pigment volume concentration %), Volume % of solids and DNV (density of non-volatiles) are reported. It is important to note that PVC is related only to the volume % of the opacifying materials, while the Volume % of solids parameter is inclusive of all the solid components in the paint.

For instance, if the paint formulation α -01 is considered as a representative example, having Volume % solids of 28%, PVC total of 24% and DNV of 1.03 g cm^3 , this means that the initial volume for the wet paint is constituted by solvent for 72% and by solid materials for 28%. Once the paint is dry due to the evaporation of all the solvent, the initial 28% of solid materials is all that is left and this constitutes 100% of the dry paint film. This solid material has a density of 1.03 g cm^3 . Out of the solid

materials making up the dry film, 24% is the volume of scattering materials (in this case polystyrene multi-voided particles), while the remaining 76% is non scattering materials (binders and other film-forming, film-protecting agents).

Table 6: A list of the 18 paint formulations prepared in order to measure the scattering power of the paint films containing the polystyrene multi-voided particles. The values of PVC % (pigment volume concentration %), Volume % of all the solids and the paint DNV (density of non-volatiles) are reported. The levels of opacifiers (TiO₂, Ropaque and Polystyrene NIPS) vary from formulation to formulation; however the total amount of solids is kept constant at 28%. The data in the table are better visualised in the diagram in Figure 78.

Formulation	TiO ₂ - PVC %	Ropaque E - PVC %	PS NIPS - PVC %	PVC Total %	Volume % solids	DNV / g cm ⁻³
α-00	0	0	0	0	28	1.17
α-01	0	0	24	24	28	1.03
α-10	0	24	0	24	28	1.03
α-11	0	24	24	48	28	0.89
α-M	0	12	12	24	28	1.13
α-N	0	18	6	24	28	1.13
β-00	2	0	0	2	28	1.23
β-01	2	0	24	26	28	1.09
β-10	2	24	0	26	28	1.09
β-11	2	24	24	50	28	0.95
β-M	2	12	12	26	28	1.13
β-N	2	18	6	26	28	1.13
γ-00	4	0	0	4	28	1.29
γ-01	4	0	24	28	28	1.15
γ-10	4	24	0	28	28	1.15
γ-11	4	24	24	52	28	1.01
γ-M	4	12	12	28	28	1.13
γ-N	4	18	6	28	28	1.13

The data in Table 6 may be better visualised in Figure 78, in a tri-dimensional parameter space. The bottom layer of the cube represents the α-plane with TiO₂ PVC of 0%, the middle layer is the β-plane with TiO₂ PVC of 2% and the top layer is the γ-plane with TiO₂ PVC of 4%. Each of the three layers of the cube has four vertex (corresponding to minima and maxima levels of Ropaque and polystyrene), a middle point *M* and an extra point *N*. This data configuration is suitable for a two-level factorial design analysis of the scattering results.

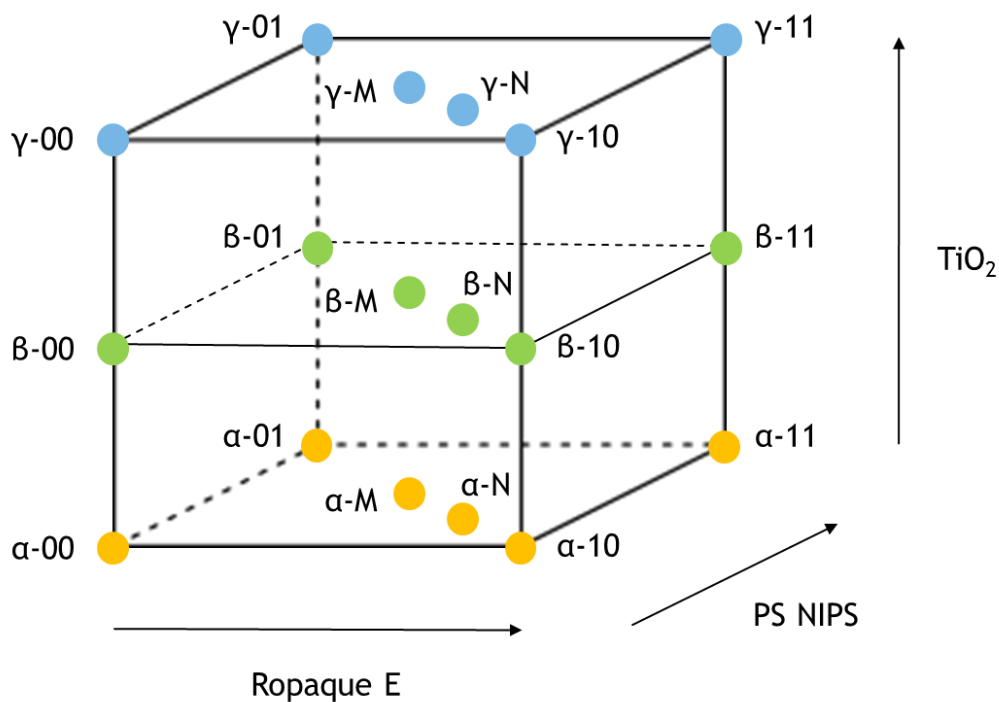


Figure 78: The diagram is a tri-dimensional representation of the data displayed in Table 6. The bottom layer of the cube represents the α -plane with TiO_2 PVC of 0%, the middle layer is the β -plane with TiO_2 PVC of 2% and the top layer is the γ -plane with TiO_2 PVC of 4%. Each of the three layers of the cube has four vertex (corresponding to minima and maxima levels of Ropaque E and Polystyrene), a middle point M and an extra point N. The three axis, indicating Ropaque E, polystyrene NIPS particles and titanium dioxide, are highlighted.

The paint formulations were stirred using a laboratory speed-mixer, in order to homogeneously disperse all the solid particles. It has to be noted that the dispersion of the polystyrene particles was not perfect: the paint formulations supplied by AkzoNobel® were not optimised to incorporate this new ingredient and small aggregates of polystyrene particles were still observable after applying high shear for the mixing. However, due to the small size of the aggregates and their even distribution within the paint film, this was not considered a major issue.

The following task required the application of the paints on a transparent substrate, to produce films of a desired thickness. The 18 formulations were spread on Melinex polyester substrates, using a film applicator with a gap of 300 μm . The films were then left to dry overnight in a fume cupboard. Once fully dry, the film thickness reduced to $\approx 150 \mu\text{m}$.

PERFORMANCE OF MULTI-VOIDED PARTICLES IN PAINT FORMULATIONS.

The scattering coefficient S characterising a dried paint film can be calculated using the Kubelka-Munk theory (equations 43-45).⁸¹ S is expressed in reciprocal microns (μm^{-1}) and it is a measure of the scattering power of a film with a thickness of 1 μm . The scattering coefficient is therefore a useful parameter to evaluate the scattering abilities of paint films, incorporating different individual opacifiers or combinations of these.

In the Kubelka-Munk theory a paint film is considered to be the sum of a large number of very thin homogenous layers.⁸² Even though a paint film is actually made of several discrete components, some contributing to the opacity (pigments, extenders), some contributing to the structural functions of the film (binders, surfactants, etc.), the theory treats the paint layers as a homogeneous medium.⁸³ Therefore a paint film of thickness X can be conceived as the sum of n identical layers of thickness dx , with n being a large number (Figure 79).⁸²

If the paint film is irradiated with a monochromatic radiation flux I , light is both scattered and absorbed by the thin layers dx .⁸¹

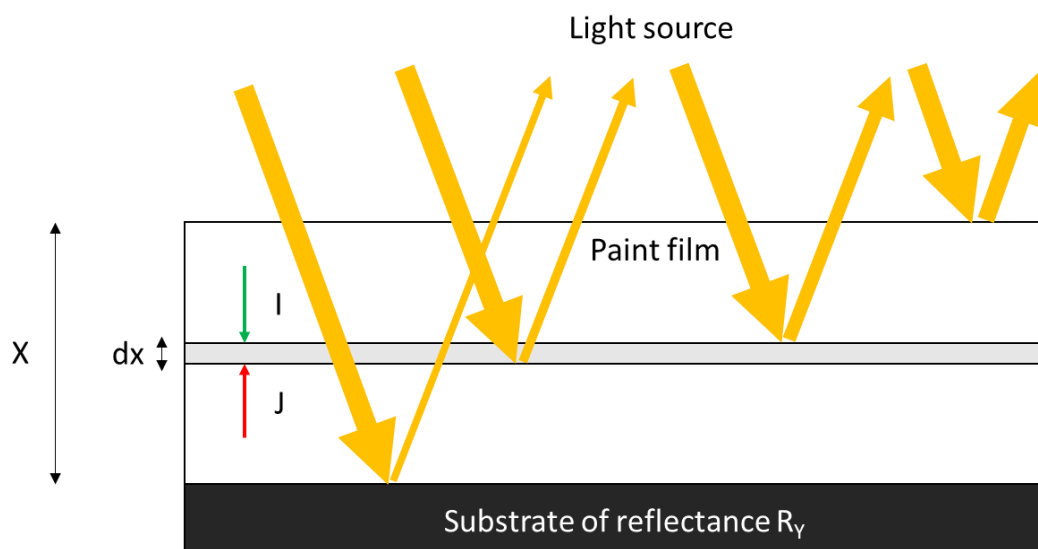


Figure 79: A sketch of the interaction between a collimated light beam and a paint film. The film of total thickness X is considered to be comprised of a number n of thin layers dx . The paint film is applied to a substrate with reflectance R_v . The light is scattered across the entire film: scattering from the surface, the internal regions and the substrate are represented. Absorption and scattering phenomena can increase or reduce the radiation flux I (green) directed towards the substrate and the radiation flux J (red) directed towards the surface.

The diffused radiation flux in the two opposite directions of the paint film can be designated as I (for the light travelling towards the substrate) and J (for the light travelling towards the surface).⁸¹

If, in passing through the dx layer, the downward flux I is decreased by an amount $WIdx$ by absorption, and increased by an amount $SIdx$ by scattering, and a similar reasoning is made for the upward flux J , then the following differential equations can be derived:⁸¹

$$\frac{-dI}{dx} = -(W + S)I + SJ \quad \text{Equation 43}$$

$$\frac{-dJ}{dx} = -(W + S)J + SI \quad \text{Equation 44}$$

where W and S are the absorption and the scattering coefficients of the paint film, respectively. The most general solution of these equations, known as the Kubelka-Munk equation, is:^{81 83}

$$R_F = \frac{1 - R_Y (a - f \coth fSX)}{a - R_Y + f \coth fSX} \quad \text{Equation 45}$$

where R_F is the reflectance of the paint film over a background of reflectance R_Y , $\coth fSX$ is the hyperbolic cotangent of fSX , X is the film thickness, and the parameters a and f are respectively:⁸¹

$$a = 1 + \frac{W}{S} \quad \text{Equation 46}$$

$$f = (a^2 - 1)^{\frac{1}{2}} \quad \text{Equation 47}$$

SX can be calculated as:⁸¹

$$SX = \frac{1}{f} \coth^{-1} \left(\frac{1 - a R_Y}{f R_Y} \right) \quad \text{Equation 48}$$

Measuring the reflectance R_F of the paint film and the reflectance R_Y of the substrate, and knowing the density of non-volatiles (DNV) of the paint, along with the film's weight and area, the scattering coefficient S can be calculated.

The reflectance measurements of the paint films were performed using a Datacolor 500 Family spectrophotometer with an aperture of 30 mm, calibrated with a black and a white tile. For each film sample, the reflectance R_F was measured in 6 different areas, using the black and the white tiles as substrates. Therefore, each film required a total of 12 measurements. In this way, any

inhomogeneity in terms of film thickness or particles dispersion (especially for polystyrene) could be averaged.

A few drops of Exxsol D40 (a low mass aromatic hydrocarbon solvent) were placed between the paint film and the tile prior to every measurement, in order to remove the layer of air between the sample and the substrate. The reflectance contributions of the transparent Melinex polyester substrate and of the Exxsol D40 oil are negligible compared to the reflectance of the paint and of the tile substrates.

Once all the reflectance measurements were performed, the same 6 areas of the paint films were cut into circles of 11.52 cm², using a punch press. The weight of the paint films circles was obtained by difference, by subtracting the weight of the Melinex polyester substrate from the weight of the Melinex substrate plus the paint. The separation of the paint layer from the Melinex layer was achieved by immersing the circles into a bath of acetone. The density of non-volatiles (DNV) of the paints was known from the formulation parameters provided by AkzoNobel® and reported in Table 6.

To calculate the scattering coefficient S of the paints, the Kubelka-Munk equations needed to be modified, in order to take into account the peculiarities of this specific system, including reflectance values over both black and white substrates, and the instrument calibration using black and white tiles. The standard method employed by AkzoNobel® for the measurement of the scattering coefficient of paint films required the calibration of the spectrophotometer for black, using a black ceramic tile capable of absorbing light with great efficiency, and also a calibration for white. This is necessary since there are no perfect white materials that reflect 100% of light at all the wavelengths of the spectral range of the instrument.⁸⁴ Usually a ceramic material is used, with a reflectance of about 90%. Such working standards are calibrated by the instrument manufacturer against a theoretical 100% reflecting white reference standard material certified by an international standard laboratory. From the calibration values, the manufacturer calculates how to adjust the measured values so that they are as if measured against the theoretical 100% white standard.⁸⁴ The calibration for both black and white therefore guarantees a greater accuracy. In order to account for this type of calibration and for the measurement over black and white substrates, the Equation 45 was rearranged and modified to give the parameter a :⁸⁴

$$a = \frac{1 + R_{wS} \times R_{wT} + [(1 + R_{bT} \times R_{bS}) \times (R_{wT} - R_{wS})]}{(R_{bS} - R_{bT})} \quad \text{Equation 49}$$

$$R_{wS} \times \left(1 - \frac{R_{bT} + R_{bS}}{R_{bS} - R_{bT}}\right) + R_{wT} \times \left(1 + \frac{R_{bT} + R_{bS}}{R_{bS} - R_{bT}}\right)$$

where R_{bT} is the reflectance of the black tile alone, used for the instrument calibration, R_{bS} is the reflectance of the sample paint over the black tile used as substrate; R_{wT} is the reflectance of the white tile alone, used for the instrument calibration, and R_{wS} is the reflectance of the sample paint over the white tile used as substrate.

The parameter f was defined by Equation 47, while Equation 48 to calculate SX was modified into:

$$SX = \frac{\ln \left[\frac{1 - R_{bT} \times a + R_{bS} \times (R_{bT} - a)}{f \times (R_{bS} - R_{bT})} + 1 \right]}{\frac{1 - R_{bT} \times a + R_{bS} \times (R_{bT} - a)}{f \times (R_{bS} - R_{bT})} - 1}}{2f} \quad \text{Equation 50}$$

The scattering coefficient S can finally be calculated as:

$$S = SX \times \frac{\text{film area}}{\text{film weight}} \times DNV \quad \text{Equation 51}$$

S is a measure of the scattering power of 1 μm of paint film and it is expressed in μm^{-1} .

It has to be noted that the film thickness X could easily be measured (it is known from the draw down that it should be $\approx 150 \mu\text{m}$ for the dry film) and the scattering S could simply be calculated dividing SX by X . However it is very unlikely that the thickness of a paint film is consistent across the entire sample. A more accurate way of calculating the thickness of a paint film is by knowing the area of the film, its weight and its density as in Equation 51. This ensures that any difference in thickness present across a paint film could be averaged.

The values for the scattering coefficient of the 18 paint formulations are reported in Table 7 and in Figure 80, in the tri-dimensional diagram. For paint α -00 the scattering coefficient was assumed to be zero by default, since no scattering material was present in the formulation.

Table 7: The values of the scattering coefficient S for the 18 paints tested. The S value for the α -00 sample was assumed to be zero by default, since no scattering material was present in the formulation. The pigment volume concentration (PVC) for the opacifiers TiO_2 , Ropaque and polystyrene NIPS is also reported.

Formulation	Scattering Coefficient S (μm^{-1})	TiO_2 - PVC	Ropaque E - PVC	PS NIPS - PVC
α -00	0	0	0	0
α -01	0.0207	0	0	24
α -10	0.0366	0	24	0
α -11	0.0433	0	24	24
α -M	0.0258	0	12	12
α -N	0.0326	0	18	6
β -00	0.0094	2	0	0
β -01	0.0493	2	0	24
β -10	0.0894	2	24	0
β -11	0.0787	2	24	24
β -M	0.0552	2	12	12
β -N	0.0730	2	18	6
γ -00	0.0574	4	0	0
γ -01	0.0753	4	0	24
γ -10	0.1392	4	24	0
γ -11	0.1040	4	24	24
γ -M	0.0901	4	12	12
γ -N	0.1080	4	18	6

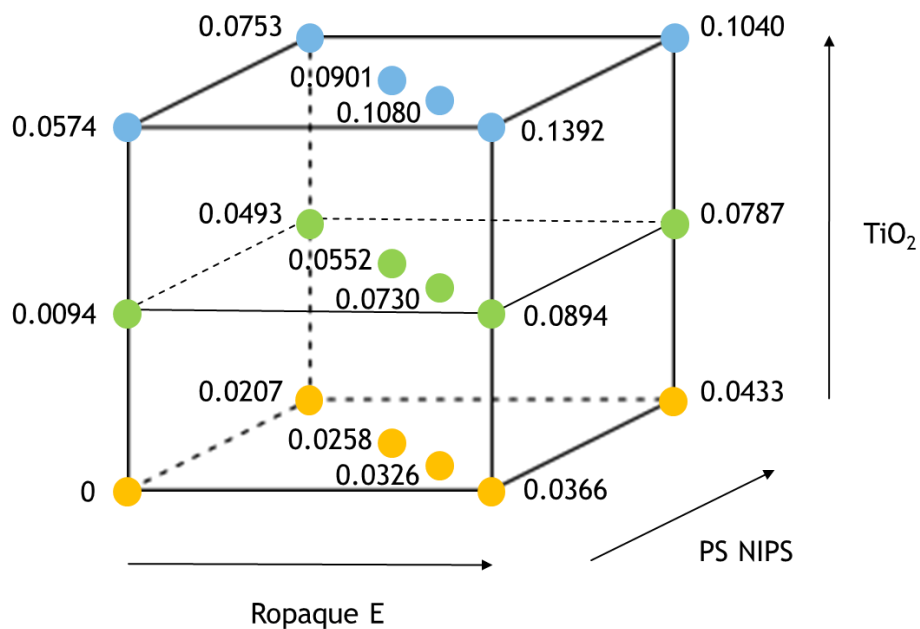


Figure 80: The diagram is a tri-dimensional representation of the data presented in Table 7. The scattering values corresponding to the respective paint formulations are indicated.

It has to be noted that a direct comparison of the scattering power of the polystyrene multi-voided particles with those of titanium dioxide and Ropaque could already be done at this point. If only the formulations with a single component are considered (α -01 for polystyrene, α -10 for Ropaque and γ -00 for titanium dioxide), a comparison of the respective scattering coefficients would show that the scattering power of polystyrene multi-voided particles is 57% that of Ropaque and 6% that of titanium dioxide. (Note that for a direct comparison the scattering of TiO_2 at 24% PVC should be used, Equation 53).

$$\frac{S_{\text{polystyrene}}}{S_{\text{Ropaque}}} \times 100 = \frac{0.0207}{0.0366} \times 100 = 57 \% \quad \text{Equation 52}$$

$$\frac{S_{\text{polystyrene}}}{S_{\text{titanium dioxide}}} \times 100 = \frac{0.0207}{\left(0.0574 \times \frac{24}{4}\right)} \times 100 = \frac{0.0207}{0.3444} \times 100 = 6 \% \quad \text{Equation 53}$$

However this simple comparison may not tell the whole story: it does not account for possible **synergistic effects** between the three opacifying materials. A synergistic effect may be defined as an interaction between two or more agents, which produces an effect greater than the sum of their individual effects. In this simple comparison it is impossible to determine whether the scattering resulting from a combination of two out of the three materials investigated, or the scattering resulting from the combination of all three the materials, would be greater, smaller or equal to the sum of the individual contributions.

Therefore, in order to investigate both the scattering abilities of the polystyrene multi-voided particles, titanium dioxide and Ropaque, and the effects of their interactions, a two-level factorial design analysis⁸⁵ was performed.

Factorial designs are used in experiments involving several factors, where it is important to investigate the **joint effects** of the factors on a response variable.⁸⁶ In the basic case, each of the k factors considered has two levels: a minimum (-) and a maximum (+). Factorial design analysis is indicated with the notation 2^k , where the base is the number of levels and the exponent k is the number of factors considered.⁸⁷

In this particular case, since three factors are involved (TiO_2 , Ropaque and polystyrene particles), a 2^3 factorial design analysis is performed. The general version of a 2^3 factorial design considers the eight possible combinations between the three factors (Table 8), geometrically arranged into a cubic

parameter space (Figure 81): these combinations are indicated with lower case letters, as indicated in the diagram (Figure 81).⁸⁵

Table 8: The design matrix with all the possible combinations between the three factors A, B and C. By default the combination with all low levels is labelled as (1). Lower case letters are used to indicate the combination of the three factors (each combination is assigned only letters corresponding to factors with positive sign). A tri-dimensional representation of the design matrix is given in Figure 81 in a cubic parameter space.

Combination	Factors		
	A	B	C
(1)	-	-	-
a	+	-	-
b	-	+	-
ab	+	+	-
c	-	-	+
ac	+	-	+
bc	-	+	+
abc	+	+	+

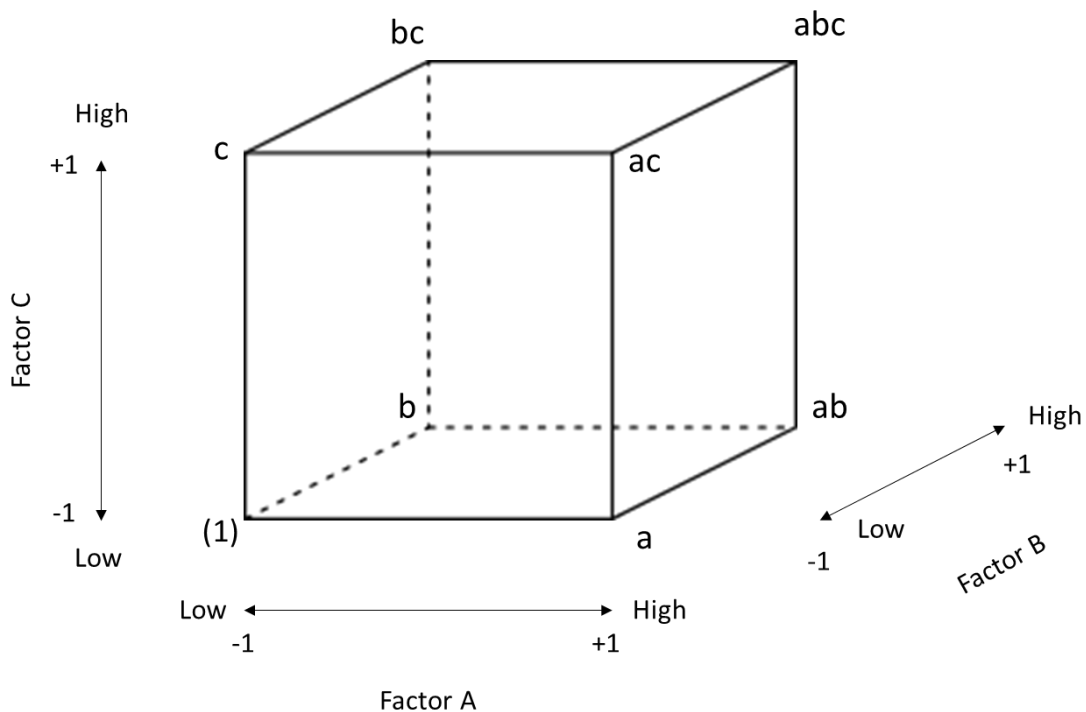


Figure 81: A representation of the design matrix for a 2^3 factorial design in a cubic parameter space. The low and high levels for each factor A, B and C are coded as (-1) and (+1) respectively. The factor A is on the X-axis, the factor B on the Y-axis and the factor C on the Z-axis. The combinations of the factors are indicated in lower case letters. Adapted from "Response Surface Methodology: Process and Product Optimization Using Designed Experiments", Myers and Montgomery, 2009.⁸⁶

The design matrix can be expanded (Table 9) in order to account also for the effects of the interactions between the factors *A*, *B*, and *C*. There are three possible two-factor interactions *AB*, *AC* and *BC*, and a three-factor interaction *ABC*. The parameter *I* is given by all the high levels (+).⁸⁶

Table 9: A comprehensive design matrix including the two-factor and three-factor interactions, along with the parameter *I*. The interactions signs are obtained by multiplying the signs of the main factors (*A*, *B*, and *C*) involved in the effect. *I* includes all the high effects.

Combination	Factorial effect							
	I	A	B	C	AB	AC	BC	ABC
(1)	+	-	-	-	+	+	+	-
a	+	+	-	-	-	-	+	+
b	+	-	+	-	-	+	-	+
ab	+	+	+	-	+	-	-	-
c	+	-	-	+	+	-	-	+
ac	+	+	-	+	-	+	-	-
bc	+	-	+	+	-	-	+	-
abc	+	+	+	+	+	+	+	+

The idea behind the use of a factorial design analysis is to quantify the impact of the three factors and their interactions on the response variable.⁸⁵ In this specific case the aim is to quantify the contributions of the three factors (TiO_2 , Ropaque and polystyrene particles) and that of their interactions to the scattering power *S* of the paint films.

The effects of the three factors and their interactions can be geometrically represented as illustrated in Figure 82. The main effects *A*, *B* and *C* are obtained as a difference between the faces of the cube, while the effects of the two-factor interactions *AB*, *AC* and *BC* are obtained as a difference between the edges of the cube. Finally, the three-factor interaction *ABC* is given by the difference between the vertices of the cube.⁸⁶

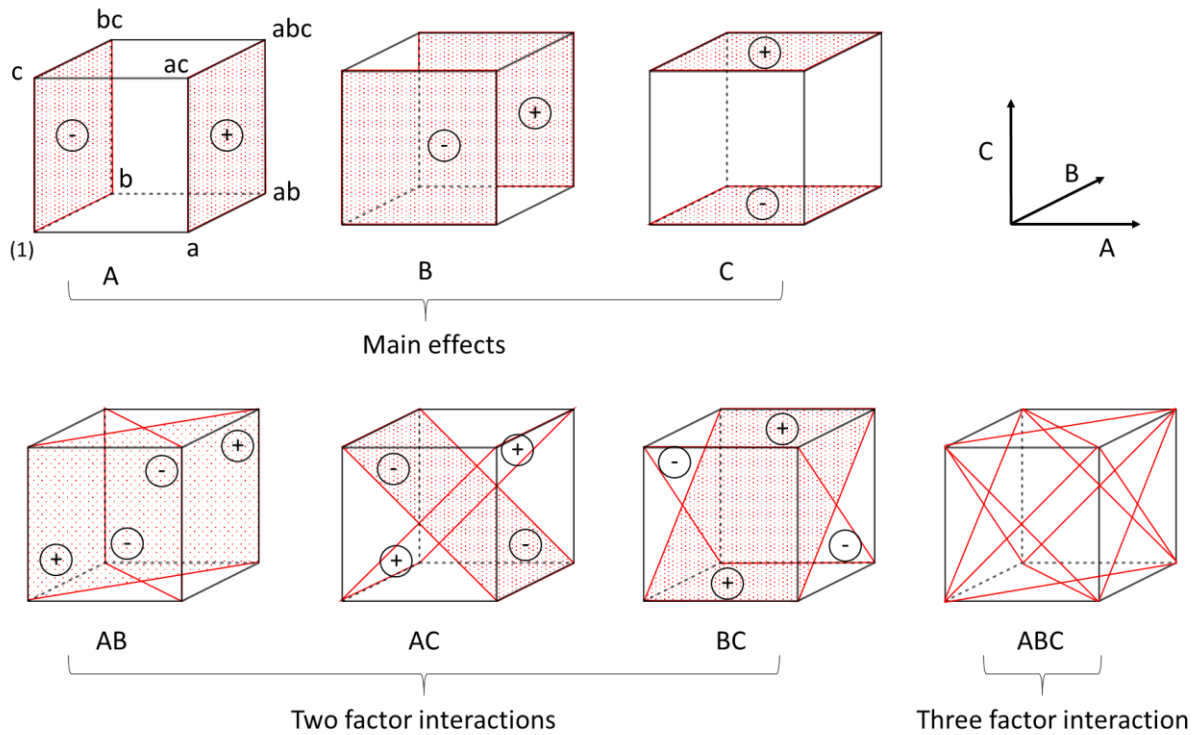


Figure 82: A geometric representation of the main effects and interactions in a 2^3 factorial design. The main effects are given by the difference between the faces of the cube. The two-factor interactions are given by the difference between the edges of the cube. The three-factor interaction is given by the difference between the vertices of the cube. Adapted from "Response Surface Methodology: Process and Product Optimization Using Designed Experiments", Myers and Montgomery, 2009.⁸⁶

The effects in a 2^3 factorial design can therefore be calculated as follows:⁸⁶

$$A = \frac{a + ab + ac + abc}{4n} - \frac{(1) + b + c + bc}{4n} \quad \text{Equation 54}$$

where n is the number of replicate measurements and the combinations values are the sum of the n measurement values. For convenience the Equation 54 can be re-arranged as:⁸⁶

$$A = \frac{1}{4n} [a + ab + ac + abc - (1) - b - c - bc] \quad \text{Equation 55}$$

Similarly the other effects can be calculated as:⁸⁶

$$B = \frac{1}{4n} [b + ab + bc + abc - (1) - a - c - ac] \quad \text{Equation 56}$$

$$C = \frac{1}{4n} [c + ac + bc + abc - (1) - a - b - ab] \quad \text{Equation 57}$$

$$AB = \frac{1}{4n} [abc - bc + ab - b - ac + c - a + (1)] \quad \text{Equation 58}$$

$$AC = \frac{1}{4n} [(1) - a + b - ab - c + ac - bc + abc] \quad \text{Equation 59}$$

$$BC = \frac{1}{4n} [(1) + a - b - ab - c - ac + bc + abc] \quad \text{Equation 60}$$

$$ABC = \frac{1}{4n} [abc - bc - ac + c - ab + b + a - (1)] \quad \text{Equation 61}$$

$$I = \frac{1}{4n} [(1) + a + b + ab + c + ac + bc + abc] \quad \text{Equation 62}$$

The sums of squares SS for the effects have statistical relevance to determine the impact of the factors and their interactions on the response variable. They can be calculated as:⁸⁶

$$SS = \frac{(\text{contrast})^2}{8n} \quad \text{Equation 63}$$

The contrast is defined as the difference between faces, edges, or vertices, according to the type of interaction considered. For instance, the sum of squares of the effect A is given by:⁸⁶

$$SS_A = \frac{[a + ab + ac + abc - (1) - b - c - bc]^2}{8n} \quad \text{Equation 64}$$

Once all the effects have been calculated, a regression model can be fitted to the 2^3 factorial design:⁸⁶

$$y = \beta_0 + \beta_1 x_1 + \beta_2 x_2 + \beta_3 x_3 + \beta_{12} x_1 x_2 + \beta_{13} x_1 x_3 + \beta_{23} x_2 x_3 + \beta_{123} x_1 x_2 x_3 \quad \text{Equation 65}$$

where the values for coefficients β_n are reported in Table 10:⁸⁶

Table 10: the coefficients for the regression model are given by one-half of the effects

$\beta_0 = I / 2$	$\beta_1 = A / 2$	$\beta_2 = B / 2$	$\beta_3 = C / 2$
$\beta_{12} = AB / 2$	$\beta_{13} = AC / 2$	$\beta_{23} = BC / 2$	$\beta_{123} = ABC / 2$

and x_1 , x_2 and x_3 represent the design factors A, B and C respectively.⁸⁶

The regression model equation can be used to generate response surface diagrams and to compare the impact of the factors and their interactions on the response variable by comparing the respective β coefficients.⁸⁶

In order to illustrate the application of a 2^3 factorial design, a simplified version of the parameter space in Figure 80 can be considered, where only the eight vertices of the cube are included: four from the α -plane corresponding to the combinations (1), a, b and ab and four from the γ -plane corresponding to the combinations c, ac, bc and abc. A design matrix (Table 11) with the levels of the three factors coded as (-1) for minimum and (+1) for maximum is used to generate the model. The geometrical representation of the parameter space is displayed in Figure 83. The factorial design analysis was performed using both JMP⁸⁸ and Design-Expert⁸⁹ statistical software.

Table 11: A design matrix with the three factors A = Ropaque, B = Polystyrene and C = TiO₂ is used to generate the model. The factor levels are coded as (-1) for minimum and (+1) for maximum. The response variable is the scattering coefficient S. The eight combinations are reported in the left column.

Combination	Factors			Response Scattering S (μm^{-1})
	A Ropaque	B Polystyrene	C TiO ₂	
(1)	-1	-1	-1	0
a	+1	-1	-1	0.0366
b	-1	+1	-1	0.0207
ab	+1	+1	-1	0.0433
c	-1	-1	+1	0.0574
ac	+1	-1	+1	0.1392
bc	-1	+1	+1	0.0753
abc	+1	+1	+1	0.1040

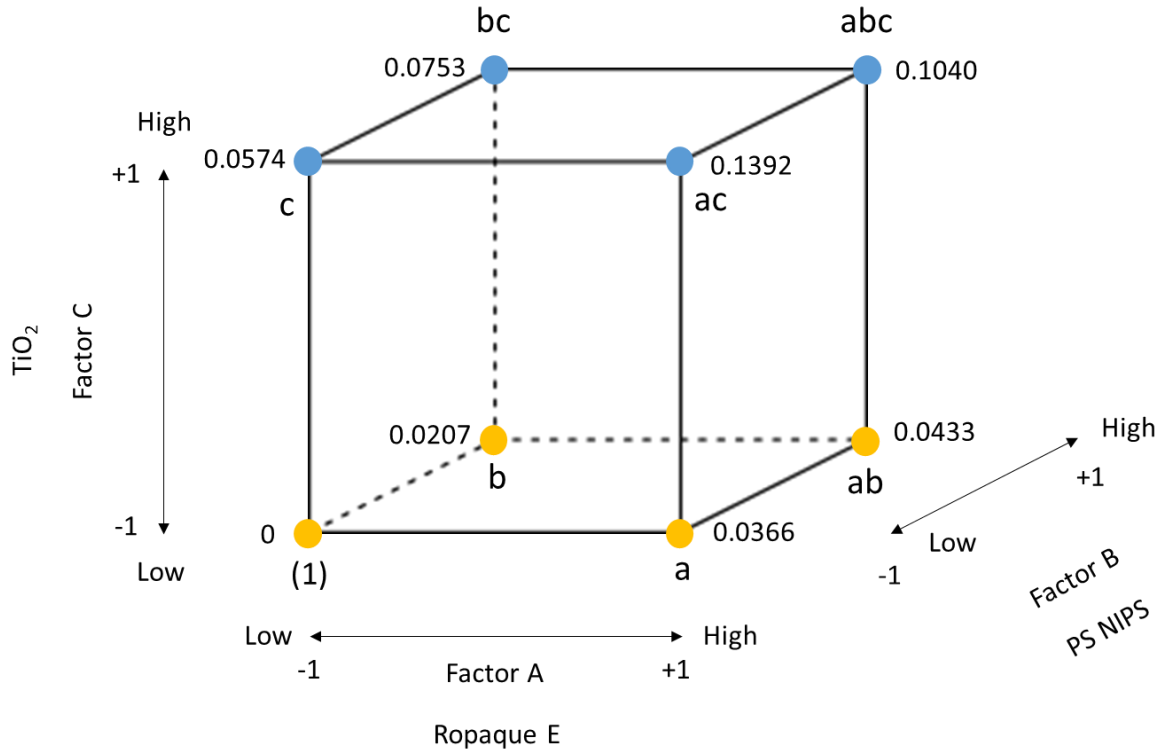


Figure 83: A geometrical representation of the simplified parameter space, including the eight vertices corresponding to the combinations for the basic model. The factor levels are coded as (-1) and (+1). The scattering values S corresponding to the combinations are displayed.

The effects are given by:

$$A = \frac{1}{4} [0.0366 + 0.0433 + 0.1392 + 0.1040 - 0 - 0.0207 - 0.0574 - 0.0753] \quad \text{Equation 66}$$

$$= 0.042425$$

$$B = \frac{1}{4} [0.0207 + 0.0433 + 0.0753 + 0.1040 - 0 - 0.0366 - 0.0574 - 0.1392] \quad \text{Equation 67}$$

$$= 0.002525$$

$$C = \frac{1}{4} [0.0574 + 0.1392 + 0.0753 + 0.1040 - 0 - 0.0366 - 0.0207 - 0.0433] \quad \text{Equation 68}$$

$$= 0.068825$$

$$AB = \frac{1}{4} [0.1040 - 0.0753 + 0.0433 - 0.0207 - 0.1392 + 0.0574 - 0.0366 - 0] \quad \text{Equation 69}$$

$$= -0.016775$$

$$AC = \frac{1}{4} [0 - 0.0366 + 0.0207 - 0.0433 - 0.0574 + 0.1392 - 0.0753 + 0.1040] \quad \text{Equation 70}$$

$$= 0.012825$$

$$BC = \frac{1}{4} [0 + 0.0366 - 0.0207 - 0.0433 - 0.0574 - 0.1392 + 0.0753 + 0.1040] \quad \text{Equation 71}$$

$$= -0.011175$$

$$ABC = \frac{1}{4} [0.1040 - 0.0753 - 0.1392 + 0.0574 - 0.0433 + 0.0207 + 0.0366 - 0] \quad \text{Equation 72}$$

$$= -0.009775$$

$$I = \frac{1}{4} [0 + 0.0366 + 0.0207 + 0.0433 + 0.0574 + 0.1392 + 0.0753 + 0.1040] \quad \text{Equation 73}$$

$$= 0.119125$$

The sums of squares for the effects are:

$$SS_A = \frac{[0.0366 + 0.0433 + 0.1392 + 0.1040 - 0 - 0.0207 - 0.0574 - 0.0753]^2}{8} \quad \text{Equation 74}$$

$$= 0.00359976$$

$$SS_B = \frac{[0.0207 + 0.0433 + 0.0753 + 0.1040 - 0 - 0.0366 - 0.0574 - 0.1392]^2}{8} \quad \text{Equation 75}$$

$$= 0.00001275$$

$$SS_C = \frac{[0.0574 + 0.1392 + 0.0753 + 0.1040 - 0 - 0.0366 - 0.0207 - 0.0433]^2}{8} \quad \text{Equation 76}$$

$$= 0.00947376$$

$$SS_{AB} = \frac{[0.1040 - 0.0753 + 0.0433 - 0.0207 - 0.1392 + 0.0574 - 0.0366 - 0]^2}{8} \quad \text{Equation 77}$$

$$= 0.00056280$$

$$SS_{AC} = \frac{[0 - 0.0366 + 0.0207 - 0.0433 - 0.0574 + 0.1392 - 0.0753 + 0.1040]^2}{8} \quad \text{Equation 78}$$

$$= 0.00032896$$

$$SS_{BC} = \frac{[0 + 0.0366 - 0.0207 - 0.0433 - 0.0574 - 0.1392 + 0.0753 + 0.1040]^2}{8} \quad \text{Equation 79}$$

$$= 0.00024976$$

$$SS_{ABC} = \frac{[0.1040 - 0.0753 - 0.1392 + 0.0574 - 0.0433 + 0.0207 + 0.0366 - 0]^2}{8} \quad \text{Equation 80}$$

$$= 0.00019110$$

The total sum of squares is obtained as:⁸⁶

$$SS_T = SS_A + SS_B + SS_C + SS_{AB} + SS_{AC} + SS_{BC} + SS_{ABC} = 0.01441890 \quad \text{Equation 81}$$

The coefficient of determination R^2 , which is a statistical measure of how well the regression model approximates the real data points, can be calculated as:⁸⁶

$$R^2 = \frac{SS_{model}}{SS_T} \times 100 \quad \text{Equation 82}$$

If only the main effects A , B and C are considered for the SS_{model} ($SS_{model} = SS_A + SS_B + SS_C$) then R^2 is equal to 90.8%. The inclusion of the two-factor interactions AB , AC and BC increases R^2 to 98.7%, meaning that the regression model is a very good fit to the data points. If all the interactions are considered, including the three-factor interaction ABC , then R^2 is 100% and the regression model is a perfect fit for the data points. The regression model, including all the interactions, is given by the equation:

$$y = 0.059563 + 0.0212125 A + 0.0012625 B + 0.0344125 C - 0.0083875 AB \quad \text{Equation 83}$$

$$+ 0.0064125 AC - 0.0055875 BC - 0.0048875 ABC$$

where A is Ropaque, B is polystyrene and C is titanium dioxide.

A modification of the design matrix (Table 11) in order to replace the coded levels (-1) and (+1) with the actual PVC (pigment volume concentration) levels for titanium dioxide (0, 4), Ropaque (0, 24) and polystyrene (0, 24) as in (Table 12) and (Figure 84),

Table 12: The modified design matrix with the non-coded factor levels, expressed in PVC (pigment volume concentration percentage): TiO_2 (0, 4); Ropaque (0, 24) and polystyrene (0, 24). The response variable is the scattering coefficient S . The eight combinations are reported in the left column.

Combination	Factors			Response Scattering S (μm^{-1})
	A Ropaque	B Polystyrene	C TiO_2	
(1)	0	0	0	0
a	24	0	0	0.0366
b	0	24	0	0.0207
ab	24	24	0	0.0433
c	0	0	4	0.0574
ac	24	0	4	0.1392
bc	0	24	4	0.0753
abc	24	24	4	0.1040

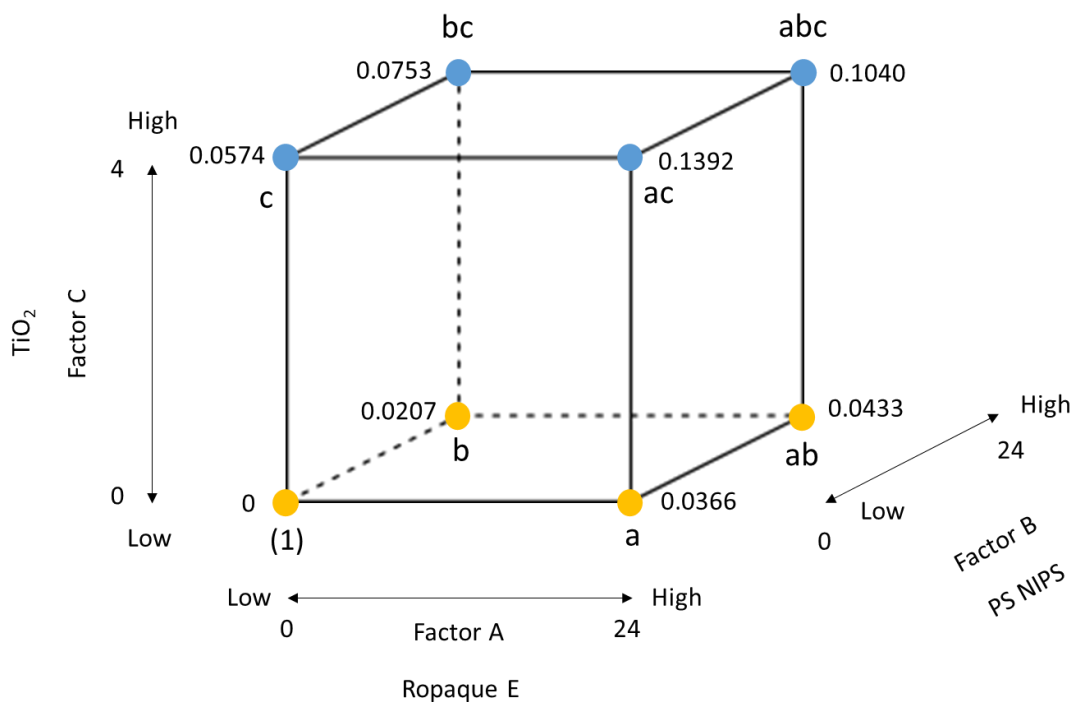


Figure 84: A geometrical representation of the parameter space, with non-coded factor levels, expressed in PVC (pigment volume concentration percentage): TiO_2 (0, 4); Ropaque (0, 24) and polystyrene (0, 24). The scattering values S corresponding to the combinations are displayed.

modifies the coefficients of the regression model (Equation 83) into:

$$y = 6.9 \times 10^{-18} + 0.0015250 A + 0.0008625 B + 0.0143500 C - 0.0000243 AB + 0.0004708 AC - 0.0000292 BC - 0.0000170 ABC \quad \text{Equation 84}$$

It is possible to prove that the regression model (Equation 84) is correct by replacing the factors A , B and C with the respective maximum levels of PVC. The correct responses S are obtained:

$$(1) = 6.9 \times 10^{-18} \approx 0 \quad \text{Equation 85}$$

$$a = 0.0015250 \times 24 = 0.0366 \quad \text{Equation 86}$$

$$b = 0.0008625 \times 24 = 0.0207 \quad \text{Equation 87}$$

$$ab = (-0.0000243 \times 24 \times 24) + a + b = 0.0433 \quad \text{Equation 88}$$

$$c = 0.0143500 \times 4 = 0.0574 \quad \text{Equation 89}$$

$$ac = (0.0004708 \times 24 \times 4) + a + c = 0.1392 \quad \text{Equation 90}$$

$$bc = (-0.0000292 \times 24 \times 4) + b + c = 0.0753 \quad \text{Equation 91}$$

$$abc = (-0.0000170 \times 24 \times 24 \times 4) + a + b + c + (-0.0000243 \times 24 \times 24) + (0.0004708 \times 24 \times 4) + (-0.0000292 \times 24 \times 4) = 0.1040 \quad \text{Equation 92}$$

Comparing the coefficients β of the main factors A , B and C in the regression model (Equation 84) it is possible to estimate that the scattering power S of the polystyrene multi-voided particles is $\approx 57\%$ that of Ropaque and $\approx 6\%$ that of titanium dioxide:

$$\frac{\beta_{\text{polystyrene}}}{\beta_{\text{Ropaque}}} \times 100 = \frac{0.0008625}{0.0015250} \times 100 = 57 \% \quad \text{Equation 93}$$

$$\frac{\beta_{\text{polystyrene}}}{\beta_{\text{titanium dioxide}}} \times 100 = \frac{0.0008625}{0.0143500} \times 100 = 6 \% \quad \text{Equation 94}$$

This result is analogous to that obtained by a direct comparison of the scattering coefficients S of the single component formulations α -01 (polystyrene), α -10 (Ropaque) and γ -00 (titanium dioxide) shown in Equation 52 and Equation 53. However the factorial design analysis also provides a level of information that was not immediately available and obvious: from the regression model (Equation 84) it is possible to establish that there is a synergistic effect between the factors A (Ropaque) and C (titanium dioxide) given by the positive coefficient for AC (+ 0.0004708), while the interaction of B (polystyrene) with any of the other factors results into a slight antagonistic effect, as shown by the negative coefficients for AB (- 0.0000243), BC (- 0.0000292) and ABC (- 0.0000170). The synergistic effect between Ropaque and titanium dioxide is one order of magnitude larger than the antagonistic effects induced by the introduction of the polystyrene multi-voided particles in the paint formulations.

The full parameter space (Table 13), including the β -plane, the middle-points and the extra points on each plane, plus some replicates to increase statistical reliability, was used to generate the complete model (Figure 85). The regression model generated by the full parameter space has a R^2 of 99%, meaning that it is a very good fit to the data points, and it is given by:

$$y = -0.0059554 + 0.0018822 A + 0.0011345 B + 0.0139356 C - 0.0000364 AB + 0.0004539 AC - 0.0000222 BC - 0.0000166 ABC \quad \text{Equation 95}$$

Using the full model (Equation 95) to compare the coefficients β of the main factors A , B and C , it is possible to conclude that the scattering power S of the polystyrene multi-voided particles is $\approx 60\%$ that of Ropaque and $\approx 8\%$ that of titanium dioxide. These values are very close to what obtained with the simplified model (Equation 84).

$$\frac{\beta_{polystyrene}}{\beta_{Ropaque}} \times 100 = \frac{0.0011345}{0.0018822} \times 100 = 60 \% \quad \text{Equation 96}$$

$$\frac{\beta_{polystyrene}}{\beta_{titanium\ dioxide}} \times 100 = \frac{0.0011345}{0.0139356} \times 100 = 8 \% \quad \text{Equation 97}$$

Again, a synergistic effect between Ropaque and titanium dioxide is present and it is one order of magnitude larger than the antagonistic effects due to the introduction of polystyrene multi-voided particles in the system.

Table 13: The full parameter space, including the β -plane, the middle-points and the extra points on each plane, plus three replicates (highlighted in red) to increase the statistical reliability of the model.

Formulation	Scattering Coefficient S (μm^{-1})	TiO ₂ - PVC	Ropaque E - PVC	PS NIPS - PVC
α -00	0	0	0	0
α -01	0.0207	0	0	24
α -10	0.0366	0	24	0
α -10 replicate	0.0388	0	24	0
α -11	0.0433	0	24	24
α -M	0.0258	0	12	12
α -N	0.0326	0	18	6
β -00	0.0094	2	0	0
β -01	0.0493	2	0	24
β -10	0.0894	2	24	0
β -10 replicate	0.0918	2	24	0
β -11	0.0787	2	24	24
β -M	0.0552	2	12	12
β -N	0.0730	2	18	6
γ -00	0.0574	4	0	0
γ -01	0.0753	4	0	24
γ -10	0.1392	4	24	0
γ -10 replicate	0.1385	4	24	0
γ -11	0.1040	4	24	24
γ -M	0.0901	4	12	12
γ -N	0.1080	4	18	6

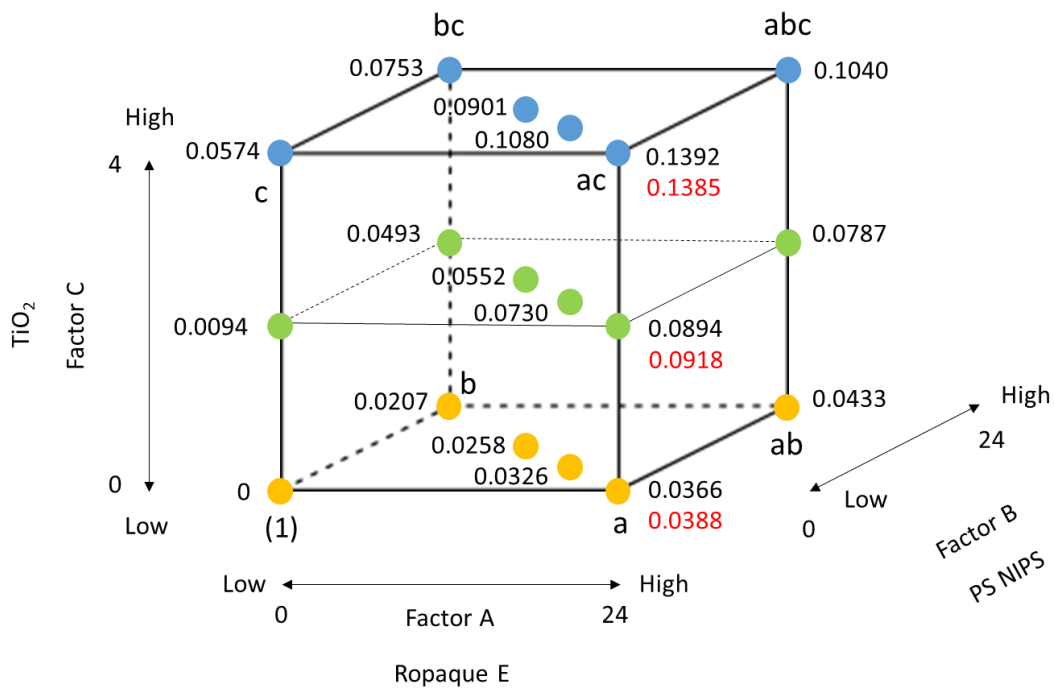


Figure 85: The geometrical representation of the full parameter space, including the replicates highlighted in red.

The factorial design analysis provided the conclusion that the multi-voided polystyrene particles, when introduced into industrial paint formulations, act as an opacifying agent with a scattering power S of $\approx 57 - 60\%$ that of the Ropaque extender and of $\approx 6 - 8\%$ that of titanium dioxide, the main white pigment used in the paint industry.

The surface profiles generated by the regression model (Equation 95) highlight the synergistic effect between titanium dioxide and Ropaque, displayed as a tilt in the response surface with increasing levels of TiO_2 (Figure 86). No synergistic effect is observed between the polystyrene multi-voided particles and the other two opacifying agents, titanium dioxide and Ropaque. A small antagonistic effect is present instead, whereby the scattering power S of a paint film containing polystyrene multi-voided particles is slightly less than the sum of the individual contributions of the single factors. A possible speculation on why this antagonistic effect is observed may be due to the concept of optical crowding,⁹⁰ already mentioned in the structural colour chapter: in order to design an efficient broad-band optical scatter, an optimum compromise between the number of scattering centres and their relative distance is necessary. If there are too many scattering centres per unit volume, this optical crowding would produce a reduction in scattering efficiency.³² In producing paint films with polystyrene multi-voided particles, it was observed that the distribution of the particles within the films was not perfectly homogeneous: the paint formulations supplied by AkzoNobel® were not optimised to accommodate the polystyrene multi-voided particles, which exhibited a tendency to form small aggregates. These aggregates would constitute optical crowding, and could be the physical cause of the antagonistic effects on the scattering detected by the factorial design analysis. Future work on the paint systems should be focused on improving the dispersion of the polystyrene multi-voided particles, by screening a number of surfactants in order to identify the most effective dispersing agent.

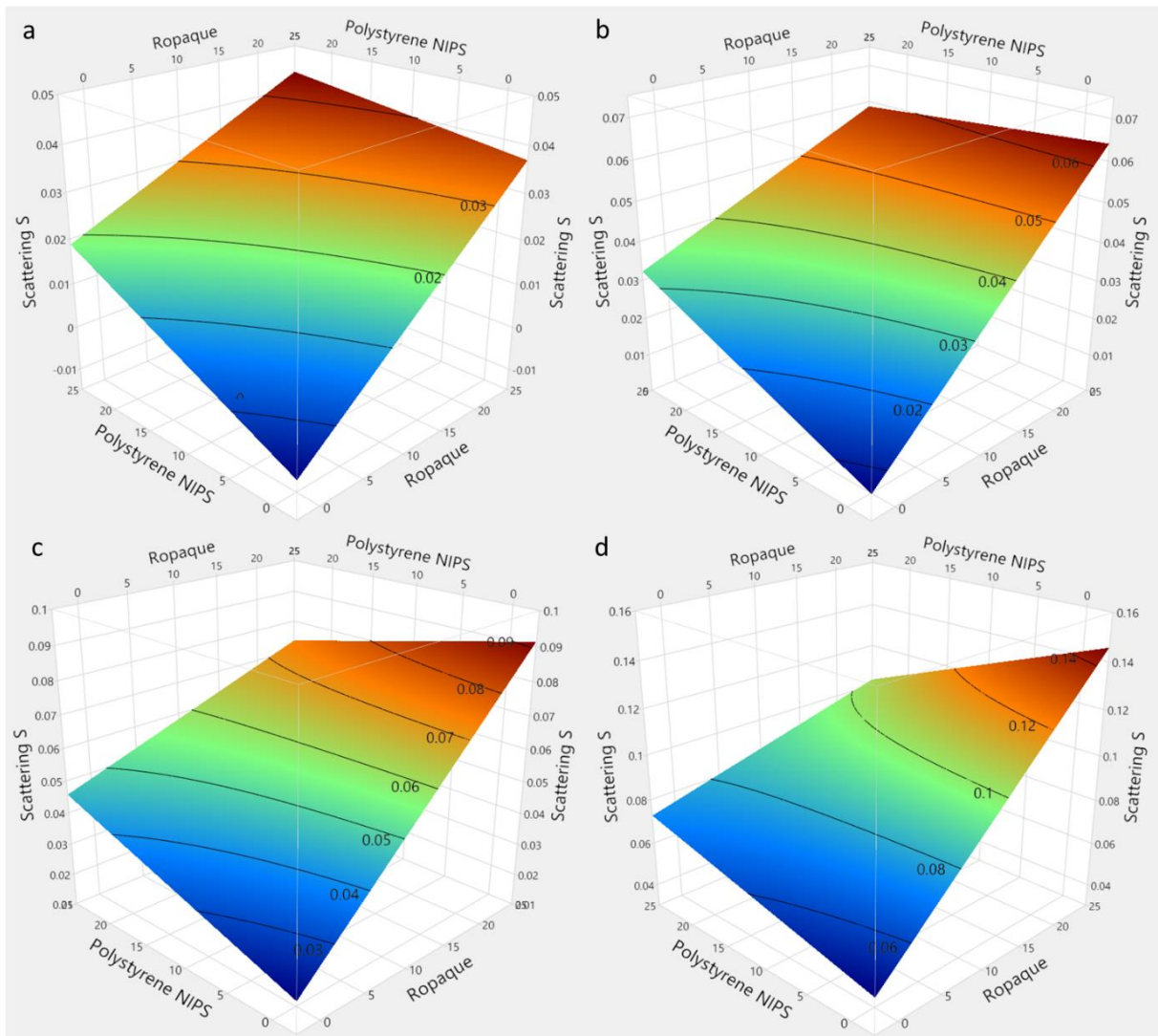


Figure 86: The surface profiles generated by the regression model (Equation 95) using the JPM⁸⁸ statistical software. Polystyrene is represented on the x-axis, Ropaque on the y-axis and the scattering S on the z-axis. The diagram (a) corresponds to the response surface for titanium dioxide PVC level of 0%, (b) to TiO_2 at 1%, (c) to TiO_2 at 2% and (d) to TiO_2 at 4%. The synergistic effect between titanium dioxide and Ropaque can be observed as a tilt in the response surface with increasing levels of TiO_2 .

The results obtained by the introduction of the polystyrene multi-voided particles into the AkzoNobel[®] paint formulations suggest that the particles produced with the NIPS method could not constitute a substantial replacement for titanium dioxide. It is apparent that the scattering power of titanium dioxide significantly overshadows that of any other opacifying agent. A meaningful comparison can only be done between extenders, where the scattering performance of the polystyrene multi-voided particles is not too distant from their closest industrial relative, Ropaque. This means that if future research on the multi-voided particles would be able to bridge the scattering gap with Ropaque, and if the manufacturing costs associated with the production of the

multi-voided particles at industrial scale should prove financially viable, it could not be excluded that the multi-voided particles could ultimately become an asset for the paint industry.

CHAPTER 8: CONCLUSIONS AND FUTURE WORK.

The objective of this work was the identification of a simple and cost effective system for the production of bio-mimetic multi-voided polymeric particles, to be introduced in paint formulation as a partial replacement for the industrial white pigment titanium dioxide.

TiO₂ is the most efficient broad-band light scattering material due to the high refractive index and its chromatic dispersity. However, the high production costs and the high carbon footprint associated with this compound constitute a motivation for investigating alternative materials. Polymeric particles were identified as a competitive alternative considering both their physical properties and comparatively low production costs.

Nature does not rely on titanium dioxide to produce striking examples of white. Achieving white in a material would simply require a significantly disordered structure that multiplies the scatter of light. The easiest way of doing this is by relying on very thick systems where the light is progressively scattered as it travels deep into the structure and interacts with a large number of interfaces.⁶

However, nature is particularly ingenious in designing structures that are capable of maximising the amount of scattering in very little material, producing a remarkable white in very thin tissues. Some of the most relevant structures displaying exceptional white are the scales of the *Cyphochilus* and *Lepidiota stigma* beetles.³⁴ The scales are only 7 to 15 µm in thickness and their internal structure is constituted by randomised, isotropic networks of rod-like filaments of chitin and air-filled voids.³⁴

Another relevant example of white was identified in the foam-like structures present in the 10 µm thick layers covering the barbs of the *Garrulus glandarius*.³⁸ *Garrulus glandarius*' feathers are characterised by a periodic colour-shift from blue to white along the barbs, due to a change in size of the air-filled voids within a keratin matrix. The white regions correspond to foam-like structures with a broader void size range and a higher degree of disorder.³⁸ The intricate networks of the beetle scales and the foam-like structures of the bird feathers were therefore identified as the target structures for the synthetic work.

An effective way of producing porous structures in polymer materials is based on the possibility of inducing phase separation in an initially homogeneous polymer solution.³⁹ The process can be initiated by the introduction of a non-solvent into the system.^{42 43} Phase separation can occur by a mechanism of nucleation and growth,⁴² producing closed pores within a polymer matrix, resembling the foam-like structures of birds, or by spinodal decomposition,⁴² producing interconnected polymer-pore domains, similar to the networks found in the beetle scales.

Polystyrene was the polymer selected for the synthetic work, due to a good compromise between costs, refractive index (similar to chitin and keratin), a large selection of good solvents, its hydrophobic nature and extensive information about its properties available from the scientific literature. The first attempt at fabricating polystyrene multi-voided particles by non-solvent induced phase separation involved a simple ternary system with tetrahydrofuran as the solvent and deionised water as the non-solvent. The fabrication process required the preparation of a polymer solution of polystyrene in tetrahydrofuran, delivered drop-wise via a syringe and a pump to a bath of non-solvent deionised water. The process was successful in producing particles with closed pores resembling the birds' foam-like structures. However, the particle size and shape was difficult to control. The particles were significantly larger than the desired 10 - 50 μm target range and their shape was far from the spherical shape needed for an efficient packing within a paint film.

The particles fabrication process was upgraded by employing an Ink Jet apparatus, capable of reducing and standardising the size of the polystyrene solution droplets delivered to the non-solvent. The Ink-Jet provided a way to control particles shape and size, which were now within the desired specifications, but presented a fatal flaw in the fact that the production was limited to a very small amount of material and the process was not industrially scalable.

In order to overcome these limitations, a modification of the fabrication process was necessary, whereby the ability to control shape and size of the polymer solution droplets (and therefore of the resulting particles) would not rely on the mechanical capabilities of the equipment employed, but rather on the intrinsic properties of the chemical system. An emulsion system was considered, where the polystyrene in toluene solution was finely dispersed into a continuous phase of deionised water. The emulsion was stabilised by the non-ionic surfactant span 80. The spherical shape of the droplets was achieved by the action of the surface tension and the droplets size could be controlled by the level of shear applied to the emulsion mixing. The emulsion was delivered to an ethanol non-solvent bath to induce phase separation in the spherical droplets of polymer solution and to precipitate the polystyrene in the form of spherical particles with a porous internal structure.

The emulsion system allowed the production of particles with the desired specifications and, most importantly, was a scalable process. The full characterisation of the emulsion system highlighted a reciprocal correlation between pore size and polystyrene concentration in the polymer solution, which enabled the correct selection of the initial conditions for the system in order to produce particles with morphological features comparable with the biological target structures.

The scale up of the emulsion process was performed in the AkzoNobel® laboratories. It required the replacement of the solvent and the non-solvent with less harmful equivalents due to the strict health and safety regulations in the company. It also required the assembling of a delivery system that could cope with the large volume of solvents needed to produce a significant amount of product (50 – 60 g) to be incorporated in the paint formulations. The formulations, containing three scattering agents, titanium dioxide, Ropaque and the newly fabricated polystyrene multi-voided particles, were mixed using the large speed-mixer machines in the AkzoNobel® laboratories, capable of producing very high shear in order to uniformly disperse all the solid materials. The paints were spread on Melinex transparent polyester substrates using a film applicator, in order to achieve films of a desired thickness. However, the dispersion of the polystyrene particles was not entirely successful, since small agglomerates were still detectable in the films. The reflectance of the paint films over black and white substrates was measured using a spectrophotometer. The density of the films was calculated. The reflectance and density data allowed the calculation of the scattering coefficient S of the paints. A factorial design analysis of the scattering results was performed in order to compare the scattering power of the polystyrene multi-voided particles with those of titanium dioxide and Ropaque, and to highlight any synergistic effect between these materials.

The analysis concluded that polystyrene multi-voided particles have a scattering power of $\approx 57 - 60\%$ that of the Ropaque extender and of $\approx 6 - 8\%$ that of titanium dioxide. It also showed a synergistic effect between titanium dioxide and Ropaque, and antagonistic effects due to the introduction of the polystyrene particles in the formulations. A possible speculation on why antagonistic effects are observed may be due to optical crowding: if there are too many scattering centres per unit volume in a material, this would result in a reduction of its scattering efficiency. In producing paint films with polystyrene multi-voided particles, it was observed that the distribution of the particles within the films was not perfectly homogeneous. The paint formulations supplied by AkzoNobel® were not optimised to accommodate the polystyrene multi-voided particles, which exhibited a tendency to form small aggregates. The aggregates would constitute optical crowding, and could be the physical cause of the antagonistic effects calculated.

From the results related to the optical performance of the polystyrene multi-voided particles into the AkzoNobel® paint formulations, it is apparent that the scattering power of titanium dioxide significantly overshadows that of any other opacifying agent. A meaningful comparison can only be done between extenders, where the scattering performance of the polystyrene multi-voided particles is not too distant from their closest industrial relative, Ropaque.

This means that if future research on the multi-voided particles would be able to bridge the scattering gap with Ropaque, and if the manufacturing costs associated with the production of the

multi-voided particles at industrial scale should prove financially viable, it could not be excluded that the multi-voided particles could ultimately become an asset for the paint industry.

Future work on the production of polystyrene multi-voided particles by non-solvent induced phase separation should address what is probably the greatest flaw of the fabrication process: the considerable amount of solvent required to produce a comparatively small amount of particles.

The fabrication of only 60 g of particles in the AkzoNobel® facilities required the use of \approx 1.1 kg of xylene, 3.0 kg of deionised water and the remarkable amount of 42 kg of isopropanol. Once the particles were isolated from the solvents by filtration, the remaining xylene, water, isopropanol mixture was disposed of as a waste. An industrial process with this level of waste to product ratio is far from being efficient.

One route towards the limitation of solvent waste may consist in designing a solvent recycling system integrated in the industrial process. Once the polystyrene particles are removed and isolated by filtration, the system should be able to achieve the separation of the individual solvents and make them available for the following production cycle. The separation of mixtures is an area of research extensively investigated^{91 92} and the separation of organic solvents from alcohol or water could be achieved by pressure-swing distillation⁹³ or pervaporation.⁹⁴ Whether this route could be technically and financially viable is a matter left to investigate for the AkzoNobel® industrial partner.

A second route for the reduction of solvent waste may consist in the entire removal of the non-solvent from the fabrication process, switching from a non-solvent induced phase separation (NIPS) to a thermally induced phase separation (TIPS) method.⁹⁵

Phase separation can be also induced by a temperature change. In polymer-solvent systems presenting an upper critical solution temperature (UCST), the polymer is soluble in all proportions above this temperature: the system is in the one-phase region.⁹⁶ A reduction in temperature below the UCST promotes the transit of the system into a two-phase region, inducing phase separation by nucleation and growth if the system transits into a metastable region, or by spinodal decomposition if the system progresses into the unstable region.⁹⁷ A TIPS process would remove the necessity of solvents separation by pressure-swing distillation or pervaporation after the polymer particles are isolated by filtration, since the only solvent present could be directly recollected and re-utilised.

TIPS routes have been explored parallel to NIPS in the research group that works on structural colour at the University of Sheffield. Low-density polyethylene in decalin is one of the most promising systems currently investigated. The formation of spherical particles of small size however still relies on the Ink-Jet equipment and it is not currently scalable.

The other issue to address is related to the optical crowding phenomenon observed in the paint films produced in the AkzoNobel® facilities, due to the formation of aggregates of polystyrene multi-voided particles. Optical crowding could be the physical cause of the antagonistic effects detected by the factorial design analysis in formulations containing polystyrene. The aggregates survive to the high shear applied during the paint formulations mixing and are difficult to remove by a mechanical action alone. The issue may be solved by implementing the paint formulations with a suitable dispersing agent, able to optimise the distribution of the polystyrene multi-voided particles within the paint, producing films of greater homogeneity. A systematic study consisting in the screening of a wide range of dispersing agents should be performed. Reflectance measurements of the paint films should follow, in order to investigate the effects of the dispersant agents on the scattering power of the paint films. Factorial design analysis should also be performed to verify whether the reversal of the optical crowding phenomenon leads to a change in behaviour of the interactions between polystyrene multi-voided particles, Ropaque and titanium dioxide. It should be expected for the observed antagonistic effects to revert into synergistic effects.

REFERENCES.

- (1) Born, M.; Wolf, E. *Principles of Optics: Electromagnetic Theory of Propagation, Interference and Diffraction of Light*; 1999. ISBN: 0080264824
- (2) Parker, A. R.; Martini, N. Structural Colour in Animals - Simple to Complex Optics. In *Optics and Laser Technology*; 2006; Vol. 38, pp 315–322.
- (3) Vukusic, P.; Kelly, R.; Hooper, I. A Biological Sub-Micron Thickness Optical Broadband Reflector Characterized Using Both Light and Microwaves. *J. R. Soc. Interface* **2009**, *6* (Suppl 2), S193–S201.
- (4) Vukusic, P.; Hallam, B.; Noyes, J. Brilliant Whiteness in Ultrathin Beetle Scales. *Science* **2007**, *315* (5810), 348.
- (5) Kinoshita, S. *Structural Colors in the Realm of Nature*; 2008. ISBN: 13 978-981-270-783-3. World Scientific Publishing Co. Pte. Ltd.
- (6) Burresti, M.; Cortese, L.; Pattelli, L.; Kolle, M.; Vukusic, P.; Wiersma, D. S.; Steiner, U.; Vignolini, S. Bright-White Beetle Scales Optimise Multiple Scattering of Light. *Sci. Rep.* **2014**, *4*, 1–7.
- (7) Lambourne; Strivens. *Paint and Surface Coatings: Theory and Practice*, Second edi.; Woodhead Publishing Ltd: Abington, England, 1999. ISBN: 9781855737006
- (8) Brock, T.; Groteklaes, M.; Mischke, P. *European Coatings Handbook*; Zorll, U., Ed.; Vincentz Verlag: Hannover, Germany, 2000. ISBN 3-87870-559
- (9) Khan, A. K.; Ray, B. C.; Dolui, S. K. Preparation of Core-Shell Emulsion Polymer and Optimization of Shell Composition with Respect to Opacity of Paint Film. *Prog. Org. Coatings* **2008**, *62* (1), 65–70.
- (10) Ruzsala, M. J. A.; Rowson, N. A.; Grover, L. M.; Choudhery, R. A. Low Carbon Footprint TiO₂ Substitutes in Paint: A Review. *Int. J. Chem. Eng. Appl.* **2015**, *6* (5), 331–340.
- (11) Laufer, G. Introduction to Optics and Lasers in Engineering. *Civ. Struct. Eng. Meas. with Interferom. Shear. Hologr.* **1996**, *24* (2–3), 90.
- (12) Hecht, E. Optics 4th Edition. *Optics 4th edition by Eugene Hecht Reading MA AddisonWesley Publishing Company 2001*. 2001, p 122. ISBN: 0321188780
- (13) Richards, A. Alien Vision Exploring the Electromagnetic Spectrum with Imaging Technology. *Press Monogr. ; 205.* **2011**, *1*. Chady T, Gratkowski S, Takagi T. Electromagneti.
- (14) Wyszecki, G.; Stiles, W. S. *Color Science. Concepts and Methods, Quantitative Data and Formulae*; 1967. ISBN: 978-0-471-39918-6
- (15) Arikawa, K. Spectral Organization of the Eye of a Butterfly, Papilio. *Journal of Comparative Physiology A: Neuroethology, Sensory, Neural, and Behavioral Physiology*. 2003, pp 791–800.

- (16) Shawkey, M. D.; Estes, A. M.; Siefferman, L. M.; Hill, G. E. Nanostructure Predicts Intraspecific Variation in Ultraviolet-Blue Plumage Colours. *Proc. R. Soc. London Ser. B-Biological Sci.* **2003**, *270* (1523), 1455–1460.
- (17) Parker, A. R. 515 Million Years of Structural Colour. *J. Opt. A Pure Appl. Opt.* **2000**, *2* (6), R15–R28.
- (18) Kinoshita, S.; Yoshioka, S. Structural Colors in Nature: The Role of Regularity and Irregularity in the Structure. *Chemphyschem* **2005**, *6*, 1442–1459.
- (19) Webb, P. A. A Primer on Particle Sizing by Static Laser Light Scattering. Micromeritics Instrument Corp. 2000.
- (20) Srinivasarao, M. Nano-Optics in the Biological World: Beetles, Butterflies, Birds and Moths. *Chem. Rev.* **1999**, *99*, 1935–1961.
- (21) Simonsen, I. Optics of Surface Disordered Systems. *The European Physical Journal Special Topics*. 2010, pp 1–103.
- (22) Yablonovitch, E. Photonic Crystals: Semiconductors of Light. *Sci. Am.* **2001**, *285* (6), 46–55.
- (23) Vukusic, P.; Sambles, J. R. Photonic Structures in Biology. *Nature* **2003**, *424* (6950), 852–855.
- (24) Vukusic, P.; Sambles, J. R.; Lawrence, C. R.; Wootton, R. J. Limited-View Iridescence in the Butterfly *Ancyluris Meliboeus*. *Proc. R. Soc. B Biol. Sci.* **2002**, *269* (1486), 7–14.
- (25) Vukusic, P.; Sambles, J. R.; Lawrence, C. R.; Wootton, R. J. Quantified Interference and Diffraction in Single Morpho Butterfly Scales. *Proc. R. Soc. B Biol. Sci.* **1999**, *266* (1427), 1403–1411.
- (26) Kinoshita, S.; Yoshioka, S.; Kawagoe, K. Mechanisms of Structural Colour in the Morpho Butterfly: Cooperation of Regularity and Irregularity in an Iridescent Scale. *Proc. Biol. Sci.* **2002**, *269* (1499), 1417–1421.
- (27) Kinoshita, S.; Yoshioka, S. Structural Colors in Nature: The Role of Regularity and Irregularity in the Structure. *ChemPhysChem*. 2005, pp 1443–1459.
- (28) Yoshioka, S.; Kinoshita, S. Single-Scale Spectroscopy of Structurally Colored Butterflies: Measurements of Quantified Reflectance and Transmittance. *J. Opt. Soc. Am. A. Opt. Image Sci. Vis.* **2006**, *23* (1), 134–141.
- (29) Ghiradella, H. Light and Color on the Wing: Structural Colors in Butterflies and Moths. *Appl. Opt.* **1991**, *30* (24), 3492.
- (30) Yoshioka, S.; Kinoshita, S. Wavelength-Selective and Anisotropic Light-Diffusing Scale on the Wing of the Morpho Butterfly. *Proc. R. Soc. B Biol. Sci.* **2004**, *271* (1539), 581–587.
- (31) Stavenga, D. G.; Wilts, B. D.; Leertouwer, H. L.; Hariyama, T. Polarized Iridescence of the Multilayered Elytra of the Japanese Jewel Beetle, *Chrysochroa Fulgidissima*. *Philos. Trans. R.*

- Soc. Lond. B. Biol. Sci.* **2011**, 366, 709–723.
- (32) Luke, S. M.; Hallam, B. T.; Vukusic, P. Structural Optimization for Broadband Scattering in Several Ultra-Thin White Beetle Scales. *Appl. Opt.* **2010**, 49 (22), 4246–4254.
- (33) Vukusic, P.; Hallam, B.; Noyes, J. Brilliant Whiteness in Ultrathin Beetle Scales. *Science*. 2007, p 348.
- (34) Cortese, L.; Pattelli, L.; Utel, F.; Vignolini, S.; Burrelli, M.; Wiersma, D. Anisotropic Light Transport in White Beetle Scales. *Adv. Opt. Mater.* **2015**.
- (35) Zi, J.; Yu, X.; Li, Y.; Hu, X.; Xu, C.; Wang, X.; Liu, X.; Fu, R. Coloration Strategies in Peacock Feathers. *Proc. Natl. Acad. Sci.* **2003**, 100 (22), 12576–12578.
- (36) Starkey, Tim; Vukusic, P. Light Manipulation Principles in Biological Photonic Systems. *Nanophotonics* **2013**, 2 (4), 289–307.
- (37) Greenewalt, C. H.; Brandt, W.; Friel, D. D. Iridescent Colors of Hummingbird Feathers*. *J. Opt. Soc. Am.* **1960**, 50 (10), 1005.
- (38) Andrew J. Parnell; Adam L. Washington; Oleksandr O. Mykhaylyk; Christopher J. Hill; Antonino Bianco; Stephanie L. Burg; Andrew J. C. Dennison; Mary Snape; Ashley J. Cadby; Andrew Smith; et al. Spatially Modulated Structural Colour in Bird Feathers. *Sci. Rep.* **2015**, 5 (August), 18317.
- (39) Wang, D. M.; Lai, J. Y. Recent Advances in Preparation and Morphology Control of Polymeric Membranes Formed by Nonsolvent Induced Phase Separation. *Curr. Opin. Chem. Eng.* **2013**, 2, 229–237.
- (40) Hiemenz, P. C.; Lodge, T. P. *Polymer Chemistry*; CRC Press, 2007. ISBN 9781574447798
- (41) Flory, P. J. Spatial Configuration of Macromolecular Chains. *Science* **1975**, 188 (4195), 1268–1276.
- (42) Ehsan Rezabeigi, Paula M. Wood-Adams, R. A. L. D. Isothermal Ternary Phase Diagram of the Polylactic Acid-Dichloromethane-Hexane System. *Polymer (Guildf)*. **2014**, 55 (14), 3100–3106.
- (43) Yang, J.; Li, D. W.; Lin, Y. K.; Wang, X. L.; Tian, F.; Wang, Z. Formation of a Bicontinuous Structure Membrane of Polyvinylidene Fluoride in Diphenyl Ketone Diluent via Thermally Induced Phase Separation. *J. Appl. Polym. Sci.* **2008**, 110 (1), 341–347.
- (44) Wang, Lawrence K.; Chen, Jiaping Paul; Hung, Yung-Tse; Shammas, N. K. *Membrane and Desalination Technologies*; Springer, 2010.
- (45) Vandeweerdt, P.; Berghmans, H.; Tervoort, Y. Temperature-Concentration Behavior of Solutions of Polydisperse, Atactic Poly(methyl Methacrylate) and Its Influence on the Formation of Amorphous, Microporous Membranes. *Macromolecules* **1991**, 24 (12), 3547–3552.

- (46) Peng, N.; Widjojo, N.; Sukitpaneenit, P.; Teoh, M. M.; Lipscomb, G. G.; Chung, T. S.; Lai, J. Y. Evolution of Polymeric Hollow Fibers as Sustainable Technologies: Past, Present, and Future. *Prog. Polym. Sci.* **2012**, *37* (10), 1401–1424.
- (47) van de Witte, P.; Dijkstra, P. J. J.; van den Berg, J. W. a. W. a; Feijen, J. Phase Separation Processes in Polymer Solutions in Relation to Membrane Formation. *J. Memb. Sci.* **1996**, *117* (1–2), 1–31.
- (48) Laity, P. R.; Glover, P. M.; Hay, J. N. Composition and Phase Changes Observed by Magnetic Resonance Imaging during Non-Solvent Induced Coagulation of Cellulose. *Polymer (Guildf)*. **2002**, *43* (22), 5827–5837.
- (49) Kim, J.; Yaszemski, M. J.; Lu, L. Three-Dimensional Porous Biodegradable Polymeric Scaffolds Fabricated with Biodegradable Hydrogel Porogens. *Tissue Eng. Part C. Methods* **2009**, *15* (4), 583–594.
- (50) Rezabeigi, E.; Wood-Adams, P. M.; Drew, R. A. L. Production of Porous Polylactic Acid Monoliths via Nonsolvent Induced Phase Separation. *Polym. (United Kingdom)* **2014**, *55* (26), 6743–6753.
- (51) Xin, Y.; Fujimoto, T.; Uyama, H. Facile Fabrication of Polycarbonate Monolith by Non-Solvent Induced Phase Separation Method. *Polym. (United Kingdom)* **2012**, *53*, 2847–2853.
- (52) Chang, H. H.; Chen, S. C.; Lin, D. J.; Cheng, L. P. Preparation of Bi-Continuous Nylon-66 Porous Membranes by Coagulation of Incipient Dopes in Soft Non-Solvent Baths. *Desalination* **2013**, *313*, 77–86.
- (53) Hong, Yi; Gao, Changyou; Shi, Yanchao; Shen, J. Preparation of Porous Polylactide Microspheres by Emulsion-Solvent Evaporation Based on Solution Induced Phase Separation. *Polym. Adv. Technol.* **2005**, No. 16, 622–627.
- (54) Karimi, Mohammad; Kish, M. H. Poly(methyl Methacrylate) Membrane: Dynamic Measurement of Concentrations During Water-Induced Phase Separation. *Macromol. Symp.* **2009**, *279*, 210–220.
- (55) Wang, Z.; Bai, R. Preparing Microgranules from Waste Polystyrene through a Novel Temperature- and Nonsolvent-Induced Phase Separation Method for Potential Adsorbent. *Ind. Eng. Chem. Res.* **2005**, No. 44, 825–831.
- (56) Balke, S. T.; Hamielec, A. E.; Leclair, B. P.; Pearce, S. L. GEL PERMEATION CHROMATOGRAPHY: Calibration Curve from Polydisperse Standards. *I EC Prod. Res. Dev.* **1969**, *8* (1), 54–57.
- (57) Striegel, A. M.; Yau, W. W.; Kirkland, J. J.; Bly, D. D. *Modern Size-Exclusion Liquid Chromatography: Practice of Gel Permeation and Gel Filtration Chromatography: Second Edition*; 2009.

- (58) Barnes, H. a. *Rheology of Industrial Polysaccharides — Theory and Applications*; 1995; Vol. 59. ISBN: 978-1-4615-2185-3
- (59) Barnes; Hutton; Walters. *An Introduction to Rheology*; 1989; Vol. 3. ISBN: 9780080933696
- (60) Hevin P. Menard. Dynamic Mechanical Analysis A Practical Introduction. *Tissue Eng.* **2008**, No. second edition.
- (61) Ichiro Noda, Yuji Higo, Noboru Ueno, and T. F. Semidilute Region for Linear Polymers in Good Solvents. *Macromolecules* **1984**, *17*, 1055–1059.
- (62) Fetters, L. J.; Hadjichristidis, N.; Lindner, J. S.; Mays, J. W. Molecular Weight Dependence of Hydrodynamic and Thermodynamic Properties for Well-Defined Linear Polymers in Solution. *J. Phys. Chem. Ref. Data* **1994**, *23* (4), 619–640.
- (63) Brandrup, J.; Immergut, E.; Grulke, E. A. Polymer Handbook. *John Wiley Sons, Inc* **1990**, *12* (3), 265. ISBN 0-471-16628-6
- (64) Van Krevelen, D. W.; Te Nijenhuis, K. *Properties of Polymers*; 2009. ISBN: 9780080915104
- (65) Allen, P. E. M.; Hardy, R.; Majer, J. R.; Molyneux, P. Applications and Limitations of Turbidimetric Titration as a Method of Characterizing Solutions of Polymers and Mixtures of Polymers. *Makromol. Chemie* **1960**, *39*, 52–66.
- (66) Chu, B. *Laser Light Scattering: Basic Principles and Practice*; 2012. ISBN: 9780323161886
- (67) Goodman, J. W. Some Fundamental Properties of Speckle*. *J. Opt. Soc. Am.* **1976**, *66* (11), 1145.
- (68) Abràmoff, M. D.; Magalhães, P. J.; Ram, S. J. Image Processing with imageJ. *Biophotonics International*. 2004, pp 36–41.
- (69) Schneider, C. a; Rasband, W. S.; Eliceiri, K. W. NIH Image to ImageJ: 25 Years of Image Analysis. *Nat. Methods* **2012**, *9* (7), 671–675.
- (70) Schnablegger, H.; Singh, Y. The SAXS Guide: Getting Acquainted with the Principles. *Ant. Paar* **2013**, 124.
- (71) Lindner, P.; Zemb, T. *Neutron, X-Rays and Light. Scattering Methods Applied to Soft Condensed Matter*; 2002; Vol. 5.
- (72) Hu, N.; Borkar, N.; Kohls, D.; Schaefer, D. W. Characterization of Porous Materials Using Combined Small-Angle X-Ray and Neutron Scattering Techniques. *J. Memb. Sci.* **2011**, *379*, 138–145.
- (73) Beaucage. Approximations Leading to a Unified Exponential/Power-Law Approach to Small-Angle Scattering. *J. Appl. Crystallogr.* **1995**, *28*, 717–728.
- (74) Ilavsky, J.; Jemian, P. R. Irena: Tool Suite for Modeling and Analysis of Small-Angle Scattering. *J. Appl. Crystallogr.* **2009**, *42* (2), 347–353.

- (75) Hsuan-Chung, W.; Huey-Jiuan, L.; Weng-Sing, H. A Numerical Study of the Effect of Operating Parameters on Drop Formation in a Squeeze Mode Inkjet Device. *Model. Simul. Mater. Sci. Eng.* **2004**, *13* (1).
- (76) Khalate, A. A.; Bombois, X.; Scorletti, G.; Babuška, R.; Koekebakker, S.; De Zeeuw, W. A Waveform Design Method for a Piezo Inkjet Printhead Based on Robust Feedforward Control. *J. Microelectromechanical Syst.* **2012**, *21* (6), 1365–1374.
- (77) Cheng-Han, W.; Weng-Sing, H. The Effect of the Echo-Time of a Bipolar Pulse Waveform on Molten Metallic Droplet Formation by Squeeze Mode Piezoelectric Inkjet Printing. *Microelectron. Reliab.* **2015**, *55*, 630–636.
- (78) Kniewske, W. M. K. and R. The Shear Viscosity Dependence on Concentration, Molecular Weight, and Shear Rate of Polystyrene Solutions. *Rheol. Acta* **1984**, *23* (1), 75–83.
- (79) Burchard, W.; Ross-Murphy, S. B. *Physical Networks: Polymers and Gels*; Elsevier Science, 1990. ISBN 1–85166–413–0
- (80) DOW Chemical Company. ROPAQUE Opaque Polymer Products. Assessment, Product Safety. 2012.
- (81) Torrent, J.; Barrón, V. Diffuse Reflectance Spectroscopy. *Methods Soil Anal. Part* **2008**, No. 5, 367–385.
- (82) Diebold, M. P. *Application of Light Scattering to Coatings: A User's Guide*; Springer, 2014. ISBN: 978-3-319-12015-7
- (83) Džimbeg-malčić, V.; Barbarić-mikočević, Ž.; Itrić, K. Kubelka-Munk Theory in Describing Optical Properties of Paper (1). *Tech. Gaz.* **2011**, *18* (1), 117–124.
- (84) Kuehni, R. G. *Color Vision and Technology*; Research Triangle Park, NC : American Association of Textile Chemists and Colorists, 2008.
- (85) Kuehl, R. *Design of Experiments: Statistical Principles of Research Design and Analysis*; Duxbury Press, 1999. ISBN: 0534368344
- (86) Myers, R. H.; Montgomery, D. C.; Anderson-Cook, C. Response Surface Methodology: Process and Product Optimization Using Designed Experiments . *Wiley Ser. Probab. Stat.* **2009**, No. June 2015, 704.
- (87) Montgomery, D. C. *Design and Analysis of Experiments*; 2012; Vol. 2. ISBN: 978-1-118-14692-7
- (88) Jones, B.; Sall, J. JMP Statistical Discovery Software. *Wiley Interdiscip. Rev. Comput. Stat.* **2011**, *3* (3), 188–194.
- (89) Vaughn, N.; Polnaszek, C. Design-Expert® Software. Stat-Ease, Inc: Minneapolis 2007.
- (90) Large, M. *Optical Biomimetics: Materials and Applications*; Woodhead Publishing Ltd, 2012.

- (91) Zhao, L.; Lyu, X.; Wang, W.; Shan, J.; Qiu, T. Comparison of Heterogeneous Azeotropic Distillation and Extractive Distillation Methods for Ternary Azeotrope Ethanol/toluene/water Separation. *Comput. Chem. Eng.* **2017**, *100*, 27–37.
- (92) Li, G.; Bai, P. New Operation Strategy for Separation of Ethanol-Water by Extractive Distillation. *Ind. Eng. Chem. Res.* **2012**, *51* (6), 2723–2729.
- (93) Zhu, Z.; Wang, L.; Ma, Y.; Wang, W.; Wang, Y. Separating an Azeotropic Mixture of Toluene and Ethanol via Heat Integration Pressure Swing Distillation. *Comput. Chem. Eng.* **2015**, *76*, 137–149.
- (94) Choudhari, S. K.; Kittur, A. A.; Kulkarni, S. S.; Kariduraganavar, M. Y. Development of Novel Blocked Diisocyanate Crosslinked Chitosan Membranes for Pervaporation Separation of Water-Isopropanol Mixtures. *J. Memb. Sci.* **2007**, *302* (1–2), 197–206.
- (95) Nishi, T.; Wang, T.; Kwei, T. Thermally Induced Phase Separation Behavior of Compatible Polymer Mixtures. *Macromolecules* **1974**, *8* (2), 227–234.
- (96) Nam, Y. S.; Park, T. G. Porous Biodegradable Polymeric Scaffolds Prepared by Thermally Induced Phase Separation. *J. Biomed. Mater. Res.* **1999**, *47* (1), 8–17.
- (97) Song, S. W.; Torkelson, J. M. Coarsening Effects on the Formation of Microporous Membranes Produced via Thermally Induced Phase Separation of Polystyrene-Cyclohexanol Solutions. *J. Memb. Sci.* **1995**, *98* (3), 209–222.